

UC San Diego

UC San Diego Electronic Theses and Dissertations

Title

Urban Microclimate, a Study of Energy Balance and Fluid Dynamics /

Permalink

<https://escholarship.org/uc/item/57r0h8q9>

Author

Yaghoobian, Neda

Publication Date

2013

Peer reviewed|Thesis/dissertation

UNIVERSITY OF CALIFORNIA, SAN DIEGO

Urban Microclimate, a Study of Energy Balance and Fluid Dynamics

A dissertation submitted in partial satisfaction of the requirements for the degree

Doctor of Philosophy

in

Engineering Sciences (Mechanical Engineering)

by

Neda Yaghoobian

Committee in charge:

Professor Jan Kleissl, Chair
Professor Joel Norris
Professor Sutanu Sarkar
Professor Kraig Winters
Professor Qiang Zhu

2013

Copyright

Neda Yaghoobian, 2013

All rights reserved.

The Dissertation of Neda Yaghoobian is approved, and it is acceptable in quality and form for publication on microfilm and electronically:

Chair

University of California, San Diego

2013

Dedication

To my parents and my husband

Table of Contents

Signature Page	iii
Dedication.....	iv
Table of Contents	v
List of Figures.....	ix
List of Tables	xiii
Acknowledgements	xv
Vita	xvii
Abstract of the dissertation	xviii
Introduction	1
Motivation.....	1
Research objectives.....	3
References.....	6
Chapter 1	7
An Indoor-Outdoor Building Energy Simulator to Study Urban Modification Effects on Building Energy Use – Model Description and Validation.....	7
1.1 Introduction.....	8
1.2 Model description	12
1.2.1 Outdoor energy balance model	12
1.2.2 Indoor energy balance model	17
1.2.3 Dynamic coupling of indoor and outdoor energy balance models	19
1.3 Validation.....	20
1.3.1 Analytical validation for a step change in outdoor air temperature	21
1.3.2 Inter-program validation	23
1.3.3 Discussion	29

1.4 TUF-IOBES application: effects of ground surface materials on building energy use	30
1.4.1 Simulation setup.....	30
1.4.2 Results and Discussion.....	34
1.5 Conclusion	38
Acknowledgements.....	40
Appendix.....	41
References.....	42
Chapter 2	47
Effect of reflective pavements on building energy use	47
2.1 Introduction.....	48
2.2 Simulation setup	51
2.2.1 Temperature of Urban Facets Indoor-Outdoor Building Energy Simulator (TUF-IOBES).....	51
2.2.2 Physical Building Setup and Thermal Properties.....	52
2.2.3 HVAC System.....	54
2.2.4 Scenarios for ground surface albedo, canopy aspect ratio, and window fraction	55
2.3 Results and discussion	58
2.3.1 Annual and daily thermal loads.....	58
2.3.2 Peak thermal loads	74
2.3.3 Discussion of Modeling Assumptions	76
2.4 Conclusion	78
Acknowledgments	80
Appendix.....	81

References.....	83
Chapter 3	86
Modeling the Thermal Effects of Artificial Turf on the Urban Environment	86
3.1 Introduction.....	88
3.2 Methods	89
3.2.1 Modeling radiation, convection, and conduction with TUF3D	89
3.2.2 Modification to TUF3D	92
3.2.3 Geometry, Initial, and Boundary Conditions	94
3.2.4 Material Properties	96
3.2.5 Effects of ground surface properties on the urban canopy	100
3.2.6 Sensitivity study and limitations	101
3.3 Results.....	102
3.3.1 Diurnal cycle of urban temperatures	102
3.3.2 Diurnal cycle of urban heat fluxes	104
3.3.3 Radiative exchange between building and ground.....	107
3.3.4 Convective heat exchange between building and ground	111
3.3.5 Sensitivity study	115
3.4 Discussion and Conclusions	117
3.4.1 Direct Temperature and heat flux effects of AT on nearby buildings	117
3.4.2 Implications of AT on energy use	118
Acknowledgements.....	124
References.....	125
Chapter 4	127
An Improved Three-Dimensional Simulation of the Diurnally Varying Street Canyon Flow	127

4.1 Introduction.....	129
4.2 Model description and simulation setup	131
4.2.1 Model Coupling	132
4.2.2 Simulation setup of TUF-IOBES	133
4.2.3 Simulation setup in PALM.....	134
4.3 Validation.....	138
4.4 Results and discussion	142
4.4.1 Mean flow and temperature field	143
4.4.2 Turbulent kinetic energy and turbulent fluxes	147
4.4.3 Non-uniform thermal forcing of the canyon surfaces throughout the day (effects of sunlit-shaded surfaces and different material thermal properties).....	158
4.4.4 Effects of ground surface albedo and wind speed.....	162
4.5 Conclusions.....	167
Acknowledgments	170
References.....	171
Chapter 5	175
Summary and conclusions	175
References.....	180

List of Figures

FIG. 1.1 Temporal variation of the inside surface temperature ($T_i(t)$) of a 0.28 m brick cavity wall after a step change in outdoor air temperature of ΔT_0 at time zero.....	23
FIG. 1.2 a) Annual heating, b) annual cooling, c) peak heating, and d) peak cooling loads (q_{sys}) comparisons between TUF-IOBES and other building energy balance models provided in BESTEST.....	25
FIG. 1.3 Comparison of hourly variation of thermal loads (q_{sys}) on January 4 th for BESTEST case 600 in Denver, CO. Positive thermal loads are heating loads and negative loads are cooling loads.....	26
FIG. 1.4 Heating (a) and cooling (b) load comparison between TUF-IOBES, BLAST, CBS-MASS, TARP, and BEM (a only) for an office space on a winter (a) and summer (b) design day in Montreal.....	28
FIG. 1.5 Surface temperatures in the TUF-IOBES simulation domain with canopy aspect ratio of 0.38 at 1200 LST of January 1st in San Diego, CA.	31
FIG. 1.6 Comparison of a) ground surface, b) canopy air, c) outside building wall and d) inside building surface temperatures, e) transmitted shortwave radiation into the building, and f) hourly thermal loads	35
FIG. 2.1 Surface temperatures in the TUF-IOBES simulation domain for canopy aspect ratio of 0.37, ground surface albedo of 0.3, and pre-1980 buildings at 0600 LST of July 15 th in Phoenix, AZ.....	54
FIG. 2.2 Annual heating and annual cooling loads for post (a and c) and pre (b and d) 1980 buildings in Phoenix, AZ.....	60
FIG. 2.3 Comparison of monthly averaged a) ground surface, b) canopy air, c) outdoor wall surface, d) indoor building surface temperatures, e) total transmitted shortwave radiation into the building from all windows and f) thermal loads for pre-1980 buildings.....	63
FIG. 2.4 Comparison of monthly averaged a) ground surface, b) canopy air, c) outdoor wall surface, d) indoor building surface temperatures, e) total transmitted shortwave radiation into the building from all windows and f) thermal loads for post-1980 buildings.....	65

FIG. 2.5 Comparison of the transmitted shortwave radiation through windows and total thermal load of a) post and b) pre-1980 buildings in W m^{-2} of floor area for canopies with $H/W = 1$ and ground surface albedo of 0.5.....	70
FIG. 2.6 Comparison of monthly averaged total transmitted shortwave radiation into the building from all windows (a, c) and thermal loads (b, d) in post-1980 buildings with double-pane reflective windows	72
FIG. 2.7 Comparison of monthly averaged a) total transmitted shortwave radiation into the building from all windows and b) thermal loads for post-1980 buildings in canopies with $H/W = 1$ and ground surface albedo of 0.5 for July in Phoenix, AZ.....	74
FIG. 2.8 Peak heating and peak cooling loads over a year for post (a and c) and pre (b and d) 1980 buildings in Phoenix, AZ.....	75
FIG. 3.1 TUF3D model simulation domain with buildings and ground showing surface temperature at 0700 LST.	90
FIG. 3.2 Schematic of the energy balance components between building walls and ground surface in the urban canopy.	91
FIG. 3.3a Subsurface layer depths and thermal properties for AT and grass surfaces.....	98
FIG. 3.3b Subsurface layer depths and thermal properties for asphalt and concrete surfaces. k , C and θ are defined as in Fig. 3a.....	98
FIG. 3.4 Modelled urban facets, canopy air, and building internal air temperatures for a community covered with a grass surface on a clear summer day in coastal southern California.	103
FIG. 3.5 Comparison of a) ground surface, b) canopy air, and c) building wall-average temperatures for AT, grass, asphalt, and concrete surfaces.....	105
FIG. 3.6 Modelled energy balance components for the grass and AT surfaces. Q_h , Q_e , and Q_g are sensible, latent, and ground heat fluxes, respectively. R_{net} is the net radiation.	106
FIG. 3.7 Energy balance components averaged over the four walls for grass (solid line) and AT (dashed line).....	108

FIG. 3.8 a) Longwave radiation, b) shortwave radiation, and c) total radiation from ground to building wall for different ground materials in W per m ² of ground surface area.....	109
FIG. 3.9 Comparison of sensible heat flux from a) ground and b) building walls to canopy air for AT, grass, asphalt, and concrete.....	112
FIG. 3.10 Comparison of Q_{g-wall} at the innermost wall layer for AT, grass, asphalt, and concrete.....	119
FIG. 4.1 Comparison of vertical profiles of ensemble and time averaged (over the last hour of 6 hour simulations) streamwise velocity normalized by initial bulk velocity at the center of a spanwise canyon	136
FIG. 4.2 Simulated mean wind field in PALM with $Fr =$ a) 0.73 and c) 1.17, and mean velocity vectors and streamlines of Kovar-Panskus et al. [32] for cases with $Fr =$ b) 0.73 and d) 1.17.	141
FIG. 4.3 Surface temperature in the TUF-IOBES simulation domain at a) 1015 b) 1315 c) 1615 d) 1915 LST of the August 17 th simulation with ground surface albedo of 0.1 in Phoenix, AZ (the base case simulation).	142
FIG. 4.4 Ensemble and time averaged velocity vectors and temperature field in vertical (left panel) and horizontal (right panel) cross sections in the middle of the spanwise canyon of the base case simulation.	147
FIG. 4.5 Vertical profiles of a) TKE and relative contributions from b) streamwise horizontal, c) spanwise horizontal, and d) vertical velocity variances from the center of the <i>spanwise</i> canyon.....	149
FIG. 4.6 Ensemble and time averaged mean hydrodynamic pressure field at 1600-1630 LST in a, b) y-z and c, d) x-z-cross sections in the center of the spanwise canyon of the base case and neutral simulations.	151
FIG. 4.7 Vertical profiles of a) TKE, and relative contributions from b) streamwise horizontal, c) spanwise horizontal, and d) vertical velocity variances from the center of the <i>streamwise</i> canyon	154
FIG. 4.8 Ensemble and time averaged mean hydrodynamic pressure field at 1600-1630 LST in a, b) x-z and c, d) y-z-cross sections in the center of the streamwise canyon of the base case and neutral simulations.	155

- FIG. 4.9 Vertical profiles of turbulent horizontal momentum and heat fluxes from the center of the spanwise (left column) and streamwise (right column) canyons of the base case simulation. See the text for the averaging details.....157
- FIG. 4.10 Surface temperature in the TUF-IOBES simulation domain at 1715 LST of the base case simulation. The center 4×5 patches of each facet are windows. The direction of the flow in the PALM simulations is from west to east.....159
- FIG. 4.11 Ensemble and half-hour time-averaged temperature (a, b), pressure (c, d) and velocity magnitude (e, f) difference of the base case simulation from the time period between 1700 and 1730 LST160
- FIG. 4.12 Ensemble, time and canopy-averaged TKE for a) spanwise b) streamwise canyons. Each marker represents a time-averaged value over 1800s. The ‘No wind_alb 0.1’ case was run based on the August 17th thermal forcing.....164
- FIG. 4.13 Ensemble and time-averaged a) temperature and b) velocity magnitude difference of the base case simulation minus the August 17th simulation with ground albedo of 0.5 averaged over 1300 to 1330 LST165
- FIG. 4.14 Ensemble and time-averaged a) temperature and b) velocity magnitude difference of the base case simulation minus the corresponding no wind simulation averaged over 1300 to 1330 LST166

List of Tables

TABLE 1.1 Building element thermal properties and thickness by layer.....	22
TABLE 1.2 Building and ground material thickness and thermal and radiative properties by layer. Material properties are chosen based on Incropera and DeWitt [61] and examples in the ASHRAE toolkit.....	33
TABLE 1.3 Angular and diffuse Solar Heat Gain Coefficient (SHGC), absorptance and transmittance of window glass. Glass properties are chosen based on examples in the ASHRAE toolkit	34
TABLE 1.A1 Building element thermal properties and thickness by layer for cooling and heating load validations against an intermediate floor office in Zmeureanu et al. [54].....	41
TABLE 2.1 Building and ground material thickness, and thermal and radiative properties by layer for pre and post-1980 buildings.	57
TABLE 2.2 Angular and diffuse Solar Heat Gain Coefficient (SHGC), absorptance and transmittance of window glass.	58
TABLE 2.3 Annual heating and annual cooling loads for all cases with ground surface albedo of 0.5.....	59
TABLE 2.A1 Double-pane reflective window thickness and thermal properties by layer.....	81
TABLE 2.A2 Angular and diffuse Solar Heat Gain Coefficient (SHGC), absorptance and transmittance of double-pane reflective window. Properties of the window are simulated by WINDOW v7 software [30].....	82
TABLE 3.1 Thermal and radiative properties of different ground materials.....	96
TABLE 3.2 Thermal and radiative properties of building walls and roof.....	99
TABLE 3.3 Maximum radiative flux densities between ground and wall and their timing in the day. All maxima in shortwave radiation occur at 1200 LST.....	111
TABLE 3.4 Magnitude and timing of maximum sensible heat fluxes from ground, wall and roof to canopy air.....	113

TABLE 3.5 Cumulative sensible heat fluxes over a day from the urban canopy and roof top to the atmospheric boundary layer (ABL) and the resulting air temperature differences ΔT averaged over a stagnant dry ABL of thickness 2 km.....	114
TABLE 3.6 Sensitivity of T_{can} and T_{wall} for grass and AT to wind speed, ground properties, λ_p , λ_f , above canopy air temperature, Bowen Ratio and latitude.....	116
TABLE 3.7 Building heat gain through different physical processes and surfaces according to ASHRAE [27] for grass and AT.....	121
TABLE 4.1 Stratification, ground surface albedo, and wind speed in the August 17 th and June 9 th PALM simulations.....	138

Acknowledgements

First, I would like to express my deepest appreciation and gratitude to my advisor, Professor Jan Kleissl, for the patient guidance and mentorship he provided me when I first came to the U.S. and started my PhD program, through to completion of this degree. I consider myself extremely fortunate to have known and worked with him over the years.

I was also truly fortunate to have had the opportunity to meet and work with Professor Kyaw Tha Paw U, whose intellectual heft is matched only by his genuinely good nature and down-to-earth humility. He treated me like one of his students, including me in many academic events and other occasions, and I deeply appreciate his kindnesses and support.

I would also like to express my sincere gratitude to my PhD committee members, Professor Sutanu Sarkar, Professor Kraig Winters, Professor Joel Norris, and Professor Qiang Zhu. Their comments and suggestions both within and outside the scope of my research were invaluable.

Lastly, I would like to thank my family for their love and encouragement: my parents who raised me with a love of science and supported me in my pursuits, and most of all my loving, patient husband, Kourosh, whose faithful support during the stages of this PhD is so appreciated.

The text and data in chapter 1, in full, is a reprint of the material as it appears in “An indoor–outdoor building energy simulator to study urban modification effects

on building energy use – Model description and validation”, Yaghoobian, Neda; Kleissl, Jan, *Energy and Buildings*, 54, 407–417 (2012). The dissertation author is the primary investigator and author of this article.

The text and data in chapter 2, in full, is a reprint of the material as it appears in “Effect of reflective pavements on building energy use”, Yaghoobian, Neda; Kleissl, Jan, *Urban Climate*, 2, 25-42 (2012). The dissertation author is the primary investigator and author of this article.

The text and data in chapter 3, in full, is a reprint of the material as it appears in “Modeling the thermal effects of artificial turf on the urban environment”, Yaghoobian, Neda; Kleissl, Jan; Krayenhoff, E. Scott, *Journal of Applied Meteorology and Climatology*, 49, 332–345 (2010) © American Meteorological Society (Used with permission). The dissertation author is the primary investigator and author of this article.

Chapter 4, in part is currently being prepared for submission for publication of the material. Yaghoobian, Neda; Kleissl, Jan; Paw U, Kyaw Tha. The dissertation author was the primary investigator and author of this material.

Vita

- 2013 Doctor of Philosophy in Engineering Sciences (Mechanical Engineering), University of California, San Diego, California, USA
- 2008-2013 Research Assistant, Dep. Of Mechanical Engineering, University of California, San Diego, California, USA
- 2006-2008 Researcher, Dep. Of Mechanical Engineering, University of California, San Diego, California, USA
- 2005-2006 Hydraulic Structural Engineer, ITCEN (Industrial and Technical Consulting Engineers), Tehran, Iran
- 2005 Master of Science in Civil Engineering (Hydraulics), Amirkabir University of Technology (Tehran Polytechnic), Tehran, Iran
- 2003 Bachelor of Science in Hydraulics and Agricultural irrigation Engineering, University of Mazandaran, Sari, Iran

PUBLICATIONS

Yaghoobian, Neda; Kleissl, Jan; Paw U, Kyaw Tha, “An Improved Three-Dimensional Simulation of the Diurnally Varying Street Canyon Flow”, 2013 (to be submitted)

Yaghoobian, Neda; Kleissl, Jan, “Effect of reflective pavements on building energy use”, *Urban Climate*, 2, 25-42, 2012

Yaghoobian, Neda; Kleissl, Jan, “An indoor–outdoor building energy simulator to study urban modification effects on building energy use – model description and validation”, *Energy and Buildings*, 54, 407–417, 2012

Yaghoobian, Neda; Kleissl, Jan; Krayenhoff, E. Scott, “Modeling the thermal effects of artificial turf on the urban environment”, *Journal of Applied Meteorology and Climatology*, 49, 332–345, 2010

ABSTRACT OF THE DISSERTATION

Urban Microclimate, a Study of Energy Balance and Fluid Dynamics

by

Neda Yaghoobian

Doctor of Philosophy in Engineering Sciences (Mechanical Engineering)

University of California, San Diego, 2013

Professor Jan Kleissl, Chair

Improvements in building energy use, air quality in urban canyons and in general urban microclimates requires understanding of the complex interaction between urban morphology, materials, and climate as well as their interaction with the flow dynamics in urban canyons. The review of the literature indicates that despite a long history of valuable urban microclimate studies, more comprehensive approaches

of investigating energy, heat and flow in urban areas are needed. In this research an indoor–outdoor dynamically coupled urban model, the Temperature of Urban Facets Indoor–Outdoor Building Energy Simulator (TUF-IOBES), has been developed and carefully validated. It is a building-to-canopy model that simulates indoor and outdoor building surface temperatures and heat fluxes in an urban area to estimate cooling/heating loads and energy use in buildings. The effects of a large number of parameters such as different ground surface albedo, building condition, window size and type, seasonal climate, and canopy aspect ratio on building thermal loads were investigated. The results presented in this dissertation highlight the fact that the interaction of urban materials (e.g. reflective pavements) with surrounding buildings must be considered in the energy analysis of urban areas. Although reflective pavements have been proposed as a mitigation measure for urban heat island since they reduce urban air temperatures, the increased solar reflectivity which transports solar radiation into (through fenestrations) and onto adjacent buildings increases building energy use.

To investigate a more comprehensive and realistic simulation of the diurnally varying street canyon flow and associated heat transport, TUF-IOBES three-dimensional surface heat flux distribution were used as thermal boundary conditions in large-eddy simulation (LES). Compared to previous analyses which used uniformly distributed thermal forcing on urban surfaces, the present analysis shows that non-uniform thermal forcing can result in complex local air flow patterns. Strong horizontal pressure gradients were detected in streamwise and spanwise canyons throughout the daytime which motivate larger turbulent velocity fluctuations in the

horizontal directions rather than in the vertical direction. This dissertation demonstrates that only local simulations for specific neighborhoods and urban climates can elucidate specific effects of urban mitigation measures; with often surprising outcomes.

Introduction

Motivation

Increasing energy efficiency is a primary objective for achieving energy independence and environmental sustainability. Many cities around the world face rising urban temperatures due to the global warming and increasing urban heat island (UHI) effect leading to an increase in energy use for building cooling. UHIs also impact meteorology, air quality, and public health. The US Climate Change Science Program determined that climate change will exacerbate the intensity of the UHI and recommended that ‘spatial extent’ and ‘diurnal changes’ of the UHI be evaluated at fine spatial scales. Quantification of diurnal UHI causes and effects at fine spatial scales can inform green engineering strategies (i.e. reflective roof coatings, solar panels) to improve the existing building stock and planning for energy efficient communities as well as improving the air quality in urban street canyons.

In 2005, buildings consumed 40% of total US primary energy and 72% of electricity. In addition, building heating, ventilation, and air conditioning (HVAC) consumed 15.3 quadrillion BTU, or about 37% of total building energy use (DOE, 2005) in the US. Thus, achieving sustainability requires a strong investment in integrated measurement, modeling, and control of urban heat exchange. Building indoor energy use as well as outdoor absorption and storage of solar energy is partially responsible for – and affected by - the UHI effect, which causes enhanced surface and air temperatures in urban environments compared to rural areas [1]. The UHI also

results from replacing natural landscapes with impervious surfaces such as concrete and asphalt and related changes in evapotranspiration (ET), albedo, and sky view factor [2, 3].

Since pavements make up about 40% of urban areas [4], UHI researchers now propose that cool pavements and urban evaporative cooling through vegetation should be the next step in reducing urban air temperatures. However, complex interaction between radiation, convection and conduction within the urban canyon precludes general conclusions about the direction and magnitude of the effect of these measures. Reflective pavements may actually increase building energy use through reflection of solar radiation onto building walls and into buildings through windows. Likewise evaporative cooling leads to a loss of precious water from the watershed and associated waste of embodied energy.

The effect of UHI mitigation measures depends on climate, meteorology, and geometry and materials of the urban fabric at a particular location. An accurate physical model of this situation would require simulating an entire urban region with a mesoscale weather model on building resolving scales (including building energy models) over a typical meteorological year (TMY). This is currently computationally impossible. In addition due to the complex nature of turbulence in urban roughness layers, lack of accurate information of thermal forcing from urban surfaces and also experimental and numerical limitations for holistically studying the thermal forcing effects on the flow field and heat transport, we have to be satisfied with an abstract understanding of what happens in urban canyons under real conditions. Reviewing the literature shows that despite a long history of valuable and necessary urban

microclimate studies, comprehensive study of heat and flow in urban areas are still in preliminary stages. Therefore, improvements are required in the modeling of urban meteorology that employs physical process-based descriptions at fine spatial scales and in three dimensions.

Research objectives

This research will address the following topics in the study of urban microclimates:

- Three dimensional, annual modeling of heat transfer and energy use in and above canopy to understand impacts of urban heat island mitigation measures
- Diurnal variations of the flow field and heat transport in urban street canyons due to the thermal forcing from urban surfaces

To address these topics we have developed a detailed building energy simulator which dynamically simulates indoor and outdoor building surface temperatures and heat fluxes in a three-dimensional urban area to estimate cooling/heating loads and energy use in buildings. This model is called The Temperature of Urban Facets Indoor–Outdoor Building Energy Simulator (TUF-IOBES), and its validation and applications are described in detail in Chapter 1.

In Chapters 2 and 3, where we respectively present the effects of reflective pavements and artificial turf on the urban environment and building energy use, we address questions regarding the UHI mitigation measures: How much air temperature

reduction could be achieved by increasing the albedo of urban surfaces (e.g. through reflective coating)? What is the impact of bright high albedo ground surface pavements (versus dark low albedo materials) on annual building cooling/heating loads? For high albedo pavements between buildings, what is the balance between increased building energy use due to reflection of heat into (through windows) and onto adjacent buildings versus the reduction in energy use due to reduced outside air temperature? How do the seasonal climate, shape and arrangement of buildings (i.e. urban canyon aspect ratio) as well as building age (reflected in insulation condition), window type and size, and ground surface materials affect these results? Can these results be used to inform urban planning?

In Chapter 4, effects of diurnal variations of thermal forcing from urban surfaces on flow field and heat transport in urban canyons are investigated. In this part, earlier surface heat flux simulation results from TUF-IOBES are applied as thermal boundary conditions into a large-eddy simulation (LES) model to provide a more comprehensive and realistic simulation of the diurnally varying street canyon wind flow and the associated heat transport. In this Chapter we address these questions: How do diurnal non-uniform heating in three-dimensional street canyons resulting from the effects of different urban materials (e.g. windows versus walls) and the moving shadows affect the flow in street canyons? How do these flow characteristics differ from flow in simulations that are neutrally stratified or contain uniformly heated surfaces? How do changes in ground surface albedo and wind speed modify the diurnal pattern of the flow and heat in urban canyons?

Finally, Chapter 5 summarizes the main conclusions of the present research and offers suggestions for future directions in urban microclimate studies.

References

- [1] T. R. Oke, *Boundary Layer Climates*, Routledge, ISBN 0-415-04319-0, 1987.
- [2] R. Gluch, D.A. Quattrochi, J.C. Luvall, A multi-scale approach to urban thermal analysis, *Remote Sensing of Environment* 104 (2006) 123–132.
- [3] P. J. Crutzen, The growing urban heat and pollution “island” effect—impact on chemistry and climate. *Atmospheric Environment*, 38 (2004) 3539–3540.
- [4] L. S. Rose, Akbari H, Taha H, *Characterizing the fabric of the urban environment: a case study of Greater Houston, Texas*. Lawrence Berkeley National Laboratory Report LBNL-51448, Berkeley, CA, 2003.

Chapter 1

An Indoor-Outdoor Building Energy Simulator to Study Urban Modification Effects on Building Energy Use – Model Description and Validation

Full reprint from *Energy and Buildings*, 54, 407–417, 2012

While there have been significant advances in energy modeling of individual buildings and urban canopies, more sophisticated and at the same time more efficient models are needed to understand the thermal interaction between buildings and their surroundings. In particular to evaluate policy alternatives it is of interest how building makeup, canyon geometry, weather conditions, and their combination modify heat transfer in the urban area. The Temperature of Urban Facets Indoor-Outdoor Building Energy Simulator (TUF-IOBES) is a building-to-canopy model that simulates indoor and outdoor building surface temperatures and heat fluxes in an urban area to estimate cooling/heating loads and energy use in buildings. The indoor and outdoor energy balance processes are dynamically coupled taking into account real weather conditions, indoor heat sources, building and urban material properties, composition of the building envelope (e.g. windows, insulation), and HVAC equipment. TUF-IOBES is also capable of simulating effects of the waste heat from air-conditioning systems on urban canopy air temperature. TUF-IOBES transient heat conduction is validated against an analytical solution and multi-model intercomparisons for annual and daily cooling and heating loads are conducted. An application of TUF-IOBES to study the impact of different pavements (concrete and asphalt) on building energy use is also presented.

1.1 Introduction

Urbanization or replacing natural land cover with buildings and impervious surfaces has resulted from rapid population and economic growth. Built-up surfaces

have different radiative and thermal properties and as a result a different surface energy balance than adjacent rural areas. In addition, the geometry of buildings and canopies changes flow patterns (e.g. [1, 2]) and traps radiation lowering effective albedos [3-6]. All of these effects are responsible for a different climate in urban areas with relatively higher surface and air temperatures (with a few exceptions, [7]) which is called the (surface or air temperature) urban heat island (UHI, [8]). Anthropogenic waste heat (e.g. from transportation, building air-conditioning) enhances UHI effects (e.g. [9-11]; for a review on anthropogenic heat flux modeling see Grimmond et al. [12, 13]; Sailor [14]).

Since land use change in urban areas modifies climate and weather [15, 16], physical processes in built areas and their causes and effects must be quantified effectively. Thermal and radiative properties of urban materials, building conditions (new versus old buildings), size, type, and location of windows, canyon geometry, anthropogenic heat fluxes, and most importantly the combination of these factors in different weather conditions affect urban heat transfer and building energy use. Several studies have been performed and different models have been developed to analyze these scenarios and improve mitigation measures in metropolitan areas (e.g. [17-21]). Most existing building energy models emerged from the engineering community such as, EnergyPlus [22], ASHRAE Toolkit [23], DOE-2 (U.S. National Renewable Energy Laboratory; NREL), the Building Loads Analysis and System Thermodynamics program (BLAST; U.S. Army Construction Engineering Research Laboratory), and Thermal Analysis Research Program (TARP; [24]). These models simulate the energy balance at the outside building wall/window surfaces, wall heat

conduction, the energy balance at inside faces and the indoor air heat balance. However, these models do not model the outdoor canopy air including heating, ventilating and air-conditioning (HVAC) heat emissions, the ground surface energy balance, and radiative effects of surrounding buildings. On the other hand, urban energy balance models in the meteorological community usually exclude dynamic modeling of the indoor building energy balance and anthropogenic heat fluxes released from HVAC systems. These components are usually included as prescribed values or offline models (see Grimmond et al. [12, 13, 25] for a review).

There have been some advances in modeling the *interaction* between urban climates and building energy use. For example Kikegawa et al. [9] coupled a one dimensional urban canopy meteorological model with a simple sub-model for building energy analysis. Salamanca et al. [26] developed and implemented a Building Energy Model (BEM) in an urban canopy parameterization for mesoscale models. BEM was coupled with a multi-layer urban canopy model and implemented in WRF/urban [27] with a statistical multi-scale modeling ability ranging from continental, to city, and building scales. On the building scale, Bueno et al. [28] proposed an iterative scheme for coupling EnergyPlus and the Town Energy Balance (TEB) 2-dimensional urban canopy model. Iteratively, TEB outdoor surface temperatures serve as boundary conditions for EnergyPlus and window temperature and HVAC waste heat from EnergyPlus are passed back to TEB. Iterations continue until the canyon temperature converges. Through EnergyPlus Bueno et al. [28] were able to simulate complex HVAC systems considering latent heat exchange between indoor and outdoor, building demand response strategies, and daylighting. However, this iterative process

and the TEB discrete numerical method for solving heat conduction [6] likely cause the model to be computationally too expensive for the long time periods required in building energy modeling (one year). Bouyer et al. [29] developed a CFD (Fluent [30]) – thermoradiative (from the Solene model) coupled simulation tool to estimate the microclimate influence on building energy consumption. Bouyer et al. [29] also admit that the computational cost of annual simulations is prohibitive.

The review of the literature highlights the need for computationally efficient models which employ physical process-based descriptions at fine spatial scales and capture microclimate and building energy effects of urban modifications and heat island mitigation measures. The Temperature of Urban Facets Indoor-Outdoor Building Energy Simulator (TUF-IOBES) model introduced in this paper is a building-to-canopy model that simulates indoor and outdoor building surface temperatures and associated heat fluxes in a high resolution, 3-dimensional urban domain to estimate urban microclimate, cooling/heating loads, and energy use in buildings. The indoor and outdoor energy balance processes are coupled online and dynamically take into account real weather conditions, urban microclimate, indoor heat sources, infiltration, building and urban material properties and composition of the building envelope (e.g. windows, insulation), and HVAC equipment. TUF-IOBES also simulates the effect of waste heat emissions from HVAC systems on urban canopy air temperature and in consequence on urban and building heat transfer.

The description of the outdoor and indoor energy balance models and their integration is presented in section 1.2. In section 1.3 TUF-IOBES simulations of transient heat conduction are validated against an analytical solution of the interior

wall surface temperature response to a step change in outside air temperature. Also TUF-IOBES simulations of yearly and daily cooling and heating loads are validated against other building energy simulators. In section 1.4 an example of a TUF-IOBES application on simulating effects of urban material modifications on building energy use is presented. Conclusions are presented in Section 1.5. A detailed application of TUF-IOBES to study urban heat island mitigation measures is presented in Yaghoobian and Kleissl [57].

1.2 Model description

1.2.1 Outdoor energy balance model

Our urban energy modeling research builds upon a study with the Temperature of Urban Facets in 3-D (TUF3D, [31]) model in Yaghoobian et al. [32]. The TUF-IOBES outdoor energy balance model that determines outside surface and canopy air temperatures is still based on TUF3D. The geometry, view factor, and sunlit-shaded algorithms for simulating radiation distribution over a 3-dimensional (3D) domain are directly adopted from TUF3D. Generally, the geometry of TUF3D is composed of arrays of buildings with the ability of rotating the domain. Surfaces are sub-divided into patches of identical size. The surface energy balance consisting of net longwave LW_{net} and net shortwave SW_{net} radiation (accounting for multiple reflections of direct solar radiation and shading), conduction q_{cond} , and convection q_{conv} is solved and enforced for each patch surface (Eq. 1.1).

$$SW_{net} + LW_{net} = q_{cond} + q_{conv} , \quad (1.1)$$

Direct and diffuse horizontal solar radiation is based on the TUF-IOBES forcing data file (explained later). Downwelling longwave radiation from the sky is based on Brown's sky model [33] as implemented in the ASHRAE Toolkit [23], where LW_{down} is a function of air and dew point temperatures, cloud cover and cloud height.

a. Fenestration model

Fenestrations (windows and skylights) are key components in building thermal design since they affect energy use through radiative transmission, conductive heat transfer (often lumped together as solar heat gain), infiltration air leakage, and daylighting which may affect the amount of artificial lighting. The size and position of windows, composition and thickness of glass panes, and shading devices strongly impact the cooling and heating loads in buildings.

The simple geometry of buildings with opaque walls in TUF3D was modified to accommodate windows, which are also resolved by one or several patches. The net shortwave radiation incident on each window patch (SW_{net}) is simulated based on the method used in ASHRAE Toolkit

$$SW_{net} = (abs_{dir} \times SW_{dir}) + (abs_{diff} \times SW_{diff}) - [(SHGC_{dir} - \tau_{dir}) \times SW_{dir} + (SHGC_{diff} - \tau_{diff}) \times SW_{diff}] + (SHGC_{diff} - \tau_{diff}) \times SW_s, \quad (1.2)$$

where abs , τ , and $SHGC$ are absorptance, transmittance, and solar heat gain coefficient of the window, respectively. SW_s is the total shortwave radiation from internal sources. Subscripts dir and $diff$ stand for direct and diffuse components of

solar radiation. Direct absorptance, transmittance, and SHGC of the glazing depend on the incidence angle of solar radiation. TUF-IOBES is capable of simulating up to triple pane windows. The transmitted shortwave radiation is passed to the indoor heat balance (Eq. 1.4 later).

b. Transient heat conduction model

There are several methods for simulating transient heat conduction in building envelopes [34] such as Lumped parameter methods [35], frequency response methods [36], numerical models like finite difference method (FDM) and finite element method (FEM) [37-39], and Z-transform methods [40, 41]. Fully discrete numerical models (especially FDM) are the most popular schemes in building and urban energy analysis. However, FDM have several disadvantages such as computational cost (especially for thin layers such as windows), storage requirements, and numerical stability. In order to evaluate building-canopy energy interactions over time scales greater than a few days a more efficient heat conduction scheme is needed.

In TUF-IOBES we have implemented a Z-transform method utilizing Conduction Transfer Functions (CTFs), which is an analytical based scheme for calculating conduction in solid media [40-42]. CTFs are applied for example in EnergyPlus and the ASHRAE Toolkit. CTFs are calculated based on the State Space Method which assumes a linear change in temperature between two time steps. CTF reduce computational cost since the resulting conduction equation is linearly relating surface heat flux only to the temperatures and fluxes at the inside and outside faces of

the medium (unlike in FDM and FEM, element temperatures within the medium are not required). CTF coefficients only need to be determined once for each medium (wall, roof, window, and ground patches). In TUF-IOBES over a domain of 5 by 5 buildings, CTF reduced *overall* computational time by a factor of 15 compared to the FDM. This difference would be even greater for larger and more complex domains.

Due to round-off and truncation errors, the CTF method has stability problems in thermally massive construction [41, 22] including thermally thick soil layers. To find soil surface temperature using CTF the soil layer has to be thermally thin. As a result, a constant “deep soil” temperature at the bottom boundary of the simulation domain can no longer be assumed. In TUF-IOBES to obtain the deep soil temperature over any time period P , following Hillel [43] we solve the diffusion equation for a soil with constant thermal properties, a sinusoidal temperature boundary condition at the surface and a constant temperature boundary condition at infinite depth

$$T_{soil}(z, t) = T_a + A_0 e^{-z/D} \sin \left[\frac{2\pi(t-t_0)}{P} - \frac{z}{D} - \frac{\pi}{2} \right]. \quad (1.3)$$

In this equation $T_{soil}(z, t)$ is the boundary condition for deep soil temperature at time t and depth z (m), T_a is the average surface temperature ($^{\circ}\text{C}$) over P , A_0 is the amplitude of the surface temperature ($^{\circ}\text{C}$) over P . $D = \sqrt{\alpha P / \pi}$ is the thermal damping depth (m) of temperature fluctuations over P , and α is the thermal diffusivity (m^2s^{-1}). t_0 is the time lag from an arbitrary starting time to the occurrence of the minimum temperature in period P . To avoid stability problems, the maximum allowed z is initialized as $3D$ for $P = 86400$ s where the soil temperature amplitude is 5% of the diurnal surface temperature A_0 . Instead of computing T_a and A_0 from soil

temperatures (usually not available), hourly *air* temperature is used [44]. Since soil is composed of heterogeneous horizontal layers, the effective thermal conductivity (k) is calculated as the harmonic average of thermal conductivities of the soil layers [45]. The effective volumetric heat capacity (c) is derived from the weighted sum of the thermal capacities of each separate layer [46]. k and c weighted by volume fraction of each layer are used to define an effective and constant thermal diffusivity $\alpha = k/(\rho_{soil}c)$, where ρ_{soil} is the soil density. CTF is then used to compute the soil surface temperature using the boundary condition obtained through Eq. 1.3.

c. Convection model

In a simple representation of buoyancy-driven and wind-driven air flow over a surface, the turbulent sensible heat flux (Q_h) in building energy balance models is typically expressed by the heat transfer coefficient (h) multiplied by the driving force expressed by the temperature (T) difference between the surface and air ($Q_h = h [T_{surface} - T_{Air}]$). There are several methods for calculating the heat transfer coefficient (e.g. [47-51, 24]). Models differ as to the degree of complexity of modeling free and forced convections on horizontal or vertical surfaces considering thermal stratification of the adjacent flow.

In TUF-IOBES, based on TUF3D, stability-corrected Monin–Obukhov similarly theory can be used for modeling heat transfer from horizontal surfaces. The transfer from vertical surfaces is based on a flat plate forced convection relationship considering patch surface roughness and effective wind speed [31]. Alternatively, the

DOE-2 model [52] can be applied which is a combination of the MoWiTT [50] and BLAST [51] models. In the DOE-2 method, the sum of the forced and natural convection components differs for windward and leeward surfaces and is a function of surface roughness.

d. Forcing data: Annual weather data file

Building energy analyses should be forced with a full year of representative weather data such as the TMY3 (Typical Meteorological Year 3) files provided by the National Solar Radiation Data Base. TUF-IOBES inputs hourly global horizontal, direct normal, and diffuse horizontal irradiances, cloud cover and height, dry bulb and dew point temperatures, pressure, wind speed, and wind direction at reference height from the TMY3 file. TMY3 information is linearly interpolated within the hour. TMY3 wind speed, direction, and air temperature are applied at the reference height in the surface layer; wind speed and temperature profiles in the roughness sub-layer (logarithmic law) and inside the canopy (exponential profile for wind and constant canopy air temperature) are based on Krayenhoff and Voogt [31].

1.2.2 Indoor energy balance model

Unlike the gridded outdoor energy model, the indoor model computes bulk heat exchange and temperature between surfaces. The indoor energy balance model is based on subroutines in the ASHRAE Toolkit. The inside surface heat balance shows that the heat transfer due to convection, longwave and shortwave radiation is balanced by conduction:

$$q_{LWX} + q_{SW} + q_{LWS} + q_{cond} + q_{sol} + q_{conv} = 0, \quad (1.4)$$

where q_{LWX} is the net longwave radiant exchange flux between zone surfaces modeled using Walton's mean radiant temperature with balance method [53], q_{SW} is the net shortwave radiation flux to the surface from interior light which is assumed to be distributed over the surfaces in the zone (walls, floor, and ceiling) through a user defined fraction, q_{LWS} is the longwave radiation flux from equipment, people, and lights in a zone modeled using the method of radiative/convective split of heat, q_{cond} is conduction flux through the wall simulated using CTF method, q_{sol} is the transmitted solar radiation flux absorbed on indoor surfaces, and q_{conv} is the convective heat flux to zone air based on air and surface temperature difference. Eq. 1.4 yields the indoor surface temperatures. Since the unknown surface temperature in the net longwave radiant exchange flux between surfaces (q_{LWX}) is fourth order (Stefan-Boltzmann law), Eq. 1.4 is a nonlinear equation which is solved by Newton's method (unlike the ASHRAE Toolkit which linearizes this equation).

The air in the thermal zone is considered to be well-mixed. The air heat balance consists of convection heat transfer from the zone surfaces (q_{conv}) which is based on the indoor air and surface temperature difference, convective part of internal loads (q_{CE}), the sensible load due to infiltration and ventilation (q_{IV}), and the heat transfer to/from the HVAC system (q_{sys}):

$$q_{conv} + q_{CE} + q_{IV} + q_{sys} = 0. \quad (1.5)$$

The air heat balance equation yields the room air temperature and the heating or sensible cooling load (q_{sys}) at each timestep. TUF-IOBES simulates a single or

dual-setpoint (deadband) system with no upper limit on air flow (unlimited capacity) such that the cooling and heating setpoints are immediately satisfied.

1.2.3 Dynamic coupling of indoor and outdoor energy balance models

First a real weather data file (TMY3) forces the outdoor energy balance to obtain canopy air and urban surface temperatures. Then through the indoor energy balance (Eqs. 1.4 and 1.5) surface temperatures, air temperature, and cooling/heating load inside the building are obtained. Finally the waste heat from the air-conditioning (AC) system increases the canopy air temperature.

Anthropogenic heat from AC systems is the combination of latent (Q_e) heat from equipment and people, sensible (Q_c) heat generated inside the building, and the work required for operating the thermodynamic cycle [9]. The total waste heat of the AC system (Q_A [W]) is

$$Q_A = (Q_c + Q_e) \left(\frac{1+COP}{COP} \right), \quad (1.6)$$

where COP is the coefficient of performance of the AC system. Assuming that the AC systems are mounted on the walls (versus on rooftops) of the buildings and instant mixing into the canopy, the waste heat increases the canopy air temperature. Using air density (ρ_{air}), specific heat capacity ($C_{p_{air}}$), and volume of the air inside the canopy (V_{can}), the temperature increase (ΔT_{AC}) from these anthropogenic heat fluxes becomes

$$\Delta T_{AC} = \frac{Q_A dt}{\rho_{air} C_{p_{air}} V_{can}}, \quad (1.7)$$

where dt is the simulation timestep. Since the air temperature above the canopy layer is imposed as the boundary condition, it is not affected by anthropogenic heat release and the canopy air temperature.

In TUF-IOBES the indoor and outdoor energy balance processes are dynamically coupled. At each timestep the outdoor energy balance model uses the simulated inside building surface temperatures at the previous timestep from the indoor energy model. On the other hand, the indoor energy balance model uses the outside building wall temperature simulated at the current timestep as its boundary condition. Also, the transmitted solar radiation in the interior surface heat balance q_{sol} is based on the radiation in the outdoor energy balance.

1.3 Validation

The complexity of building energy simulation programs and simplifications in describing the physical processes imply that careful validation is essential. Ideally, the performance of a building energy simulator should be validated against measured data from a real building. However, such data are not available as the urban indoor and outdoor environment is too complex to be instrumented sufficiently. So as stated by Zmeureanu et al. [54], sufficient testing should be conducted to assure that the probability of failure is sufficiently low to be acceptable. In this section a transient heat conduction simulation in TUF-IOBES is validated against an analytical solution of interior wall surface temperature response to a step change in outside air

temperature. In addition yearly and daily cooling and heating load simulations in TUF-IOBES are validated against other whole building energy simulators.

1.3.1 Analytical validation for a step change in outdoor air temperature

The variation of inside surface temperature (T_i) of a cavity wall due to a step change in outdoor air temperature (OAT) in TUF-IOBES is compared against the analytical solution. The building is a rectangular zone ($L \times W \times H = 6.0 \text{ m} \times 6.0 \text{ m} \times 3.6 \text{ m}$) with four exterior walls and no windows. Walls, outdoor air, and room air temperatures are assumed to be in steady state at 20°C initially. At $t = 0$, the OAT drops to 0°C ($\Delta T_0 = 20^\circ\text{C}$) while the room air temperature is kept constant at 20°C . The mean radiant temperature (used for calculating the radiant exchange between interior surfaces) is equal to the room air temperature and there is no air infiltration, internal mass and solar radiation. Walls, ceiling, and floor are composed of a 0.28 m brick cavity wall. The total U-value of the building walls is $1.42 \text{ W m}^{-2} \text{ K}^{-1}$ (Table 1.1). More information can be found in Zmeureanu et al. [54] and Pratt [55].

TABLE 1.1 Building element thermal properties and thickness by layer. Given the thermal resistances of outside and inside air, the heat transfer coefficients on outdoor and indoor surfaces are $34.0 \text{ W m}^{-2} \text{ K}^{-1}$ and $8.0 \text{ W m}^{-2} \text{ K}^{-1}$, respectively. Thermal resistances of outdoor and indoor air are defined as the reciprocal of the heat transfer coefficient on outdoor and indoor surfaces. Air cavity thickness was calculated based on the thermal resistance given in Zmeureanu et al. [54].

Building layer	Thickness (m)	Thermal conductivity ($\text{W m}^{-1} \text{ K}^{-1}$)	Thermal resistance ($\text{m}^2 \text{ K W}^{-1}$)
Outdoor air	Infinite		0.0294
Brick	0.14	0.73	0.192
Air cavity	0.004	0.025	0.167
Brick	0.14	0.73	0.192
Indoor air			0.125

Although in TUF-IOBES heat transfer coefficients can be calculated dynamically, to match the conditions in the analytical solution, heat transfer coefficients are fixed to the values provided by the reference.

TUF-IOBES simulation results (Fig. 1.1) start at the same initial condition ($T_i(t) = T_i(0) = 20 \text{ }^\circ\text{C}$) and reach the same steady state value ($T_i(t) = 16.4 \text{ }^\circ\text{C}$) at 45 h as the analytical solution. The analytical steady state solution is only a function of the room air temperature (T_{room}) and the ratio of the outdoor air-to-indoor wall surface (R_{ai}) and outdoor air-to-indoor air (R_{aa}) thermal resistances of the cavity wall ($T_i(45 \text{ h}) = T_{room} R_{ai}/R_{aa}$). R_{ai} and R_{aa} are the sum of the thermal resistances in Table 1.1. During the transient part, there is good agreement with a slight lag in TUF-IOBES. The difference is less than 2.3% (in terms of $T_i(0)$ minus $T_i(t)$) significantly improving over the 5% difference for CBS-MASS model [54].

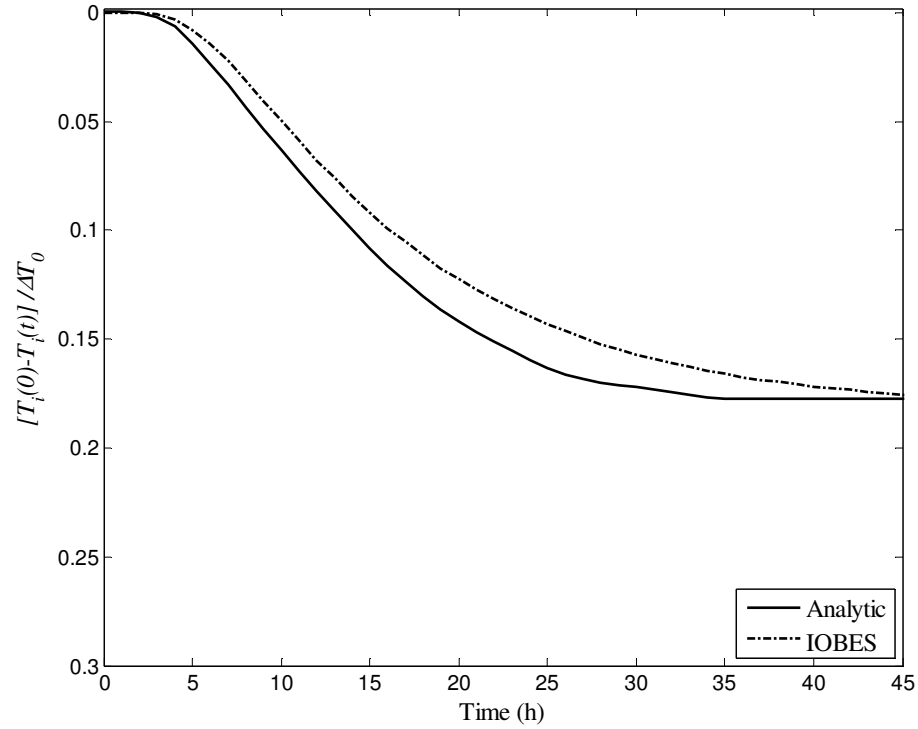


FIG. 1.1 Temporal variation of the inside surface temperature ($T_i(t)$) of a 0.28 m brick cavity wall after a step change in outdoor air temperature of ΔT_0 at time zero. The y-axis scale is the relative change of the hourly interior surface temperature with respect to the drop in OAT at initial time based on Zmeureanu et al. [54]

1.3.2 Inter-program validation

a. Annual cooling/heating load

The performance of TUF-IOBES in estimating annual cooling and heating loads was compared to other building energy simulation programs using the International Energy Agency Building Energy Simulation Test (BESTEST) and Diagnostic Method [56]. BESTEST is a standard test for “systematically testing whole-building energy simulation models and diagnosing the sources of predictive disagreement” [56]. The base case of a Low Mass Building (Case 600) is used for annual load validation.

Case 600 consists of a rectangular single zone building (8 m north and south exposures \times 6 m east and west exposures \times 2.7 m high) with lightweight construction, no interior partitions, and 12 m² of double glazing windows on the south exposure. The mechanical system is 100% efficient with no duct losses and no capacity limitation, no latent heat extraction, and a dual setpoint thermostat with deadband between 20 °C and 27 °C. The weather data file is in the typical meteorological year (TMY) format for Denver, Colorado (39.8° north latitude, 104.9° west longitude, 1609 m altitude) with an annual minimum of -24.4 °C and a maximum of 35.0 °C. The ground surface temperature is 10 °C. Detailed information on building construction characteristics and all input data including weather can be found in Judkoff and Neymark [56].

A comparison of annual and peak heating and cooling loads of TUF-IOBES and other building energy models from BESTEST is presented in Fig. 1.2. Since neither reference model results necessarily represent the ‘truth’ [56], the objective is to observe if the predicted thermal loads in TUF-IOBES fall within or close to the range of results from other programs. TUF-IOBES annual (5.36 MWh) and peak heating load (3.49 kWh) are in the range of loads (4.29 – 5.7 MWh for annual and 3.43 – 4.35 kWh for peak heating load) of the other programs. The annual cooling load from TUF-IOBES (5.52 MWh) is 10% below the lowest prediction (range 6.13 – 8.44 MWh). Likewise the peak cooling load (4.99 kWh) is under-predicted by TUF-IOBES compared to the other programs (5.96 – 7.18 kWh). Given that no sub-annual data are available for the other programs (with the exception of one day reported in the next section), it is difficult to assess the reason for the lower cooling load in TUF-IOBES.

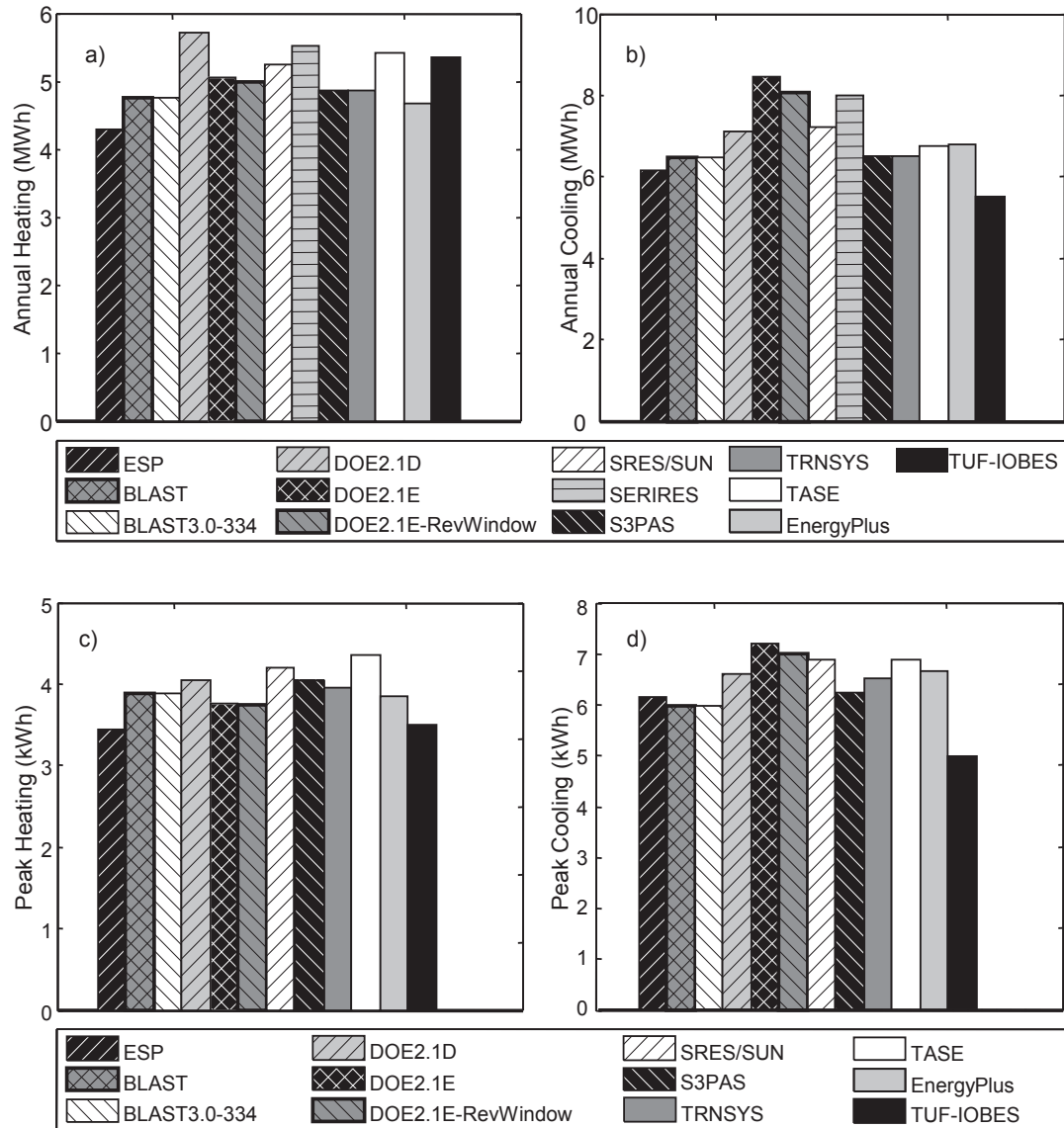


FIG. 1.2 a) Annual heating, b) annual cooling, c) peak heating, and d) peak cooling loads (q_{sys}) comparisons between TUF-IOBES and other building energy balance models provided in BESTEST

b. BESTEST Daily cooling/heating load

TUF-IOBES hourly variation of cooling and heating loads over one day (January 4th - proposed in BESTEST for the TMY of Denver, CO) is compared to the other models for BESTEST case 600 (see section a). Fig. 1.3 shows that TUF-IOBES

cooling and heating loads are in good agreement with other models. The cooling load is underpredicted consistent with the observations for the entire year in Fig. 1.2.

Radiation is an important component of the indoor energy balance. The TUF-IOBES sunlit-shaded and view factor models which were adopted from TUF3D were validated separately by comparing downwelling shortwave radiation incident on south and west walls on March 5th and July 27th for case 600. Good agreement between TUF-IOBES and BESTEST was observed (not shown).

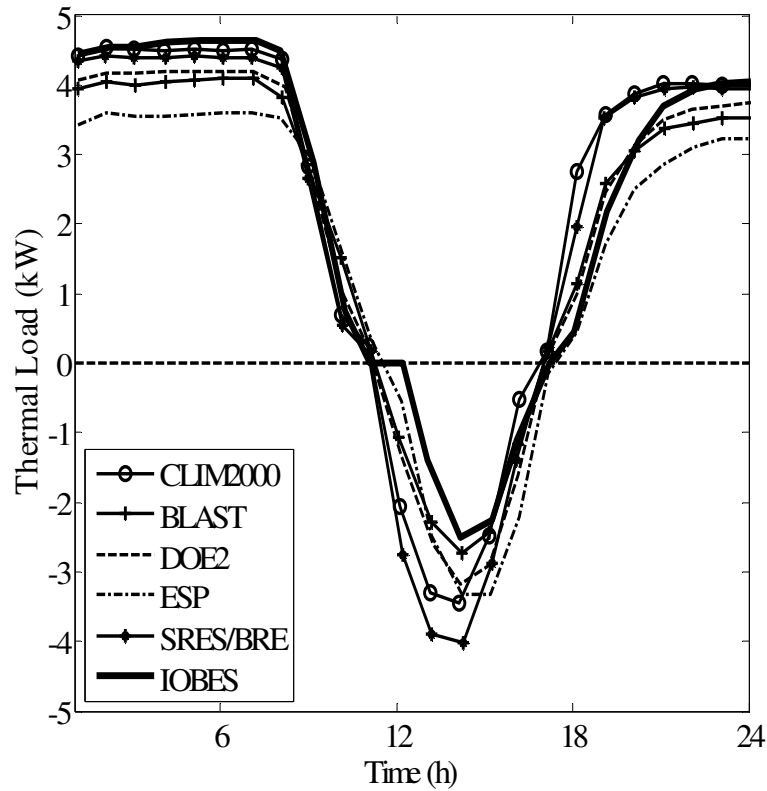


FIG. 1.3 Comparison of hourly variation of thermal loads (q_{sys}) on January 4th for BESTEST case 600 in Denver, CO. Positive thermal loads are heating loads and negative loads are cooling loads

c. Design day heating / cooling loads for an office building in Montreal

A second test is performed to compare TUF-IOBES daily variation of thermal load in an office space to other building energy models. We simulated the conditions provided in Zmeureanu et al. [54] which consist of an intermediate-floor office with dimension $L \times W \times H = 30 \text{ m} \times 30 \text{ m} \times 3.6 \text{ m}$, with four exterior walls and windows. The air temperature of the under and overlying floor is equal to the air temperature of the analyzed space making vertical heat transfer in floor and ceiling slabs negligible. In TUF-IOBES the setup is approximated by a single story office building with thermally thick roof and floor constructions such that the effects of the roof surface temperature (affected by OAT and solar radiation) on the ceiling temperature and effects of the deep soil temperature on the floor temperature are negligible. Since thermal and radiative properties of the materials are not provided in Zmeureanu et al. [54], typical properties for the windows and building construction materials are assumed (see Table 1.A1 in the appendix for details). The glazing-to-wall-ratio is 0.5 and windows are double glazing with $U = 2.8 \text{ W m}^{-2} \text{ K}^{-1}$.

Winter (December 21) and summer (July 22) design days in Montreal are forced using OAT, global horizontal and direct normal radiation provided in Zmeureanu et al. [54]. Since no information about ground surface temperature is available and most building energy models do not simulate it, ground surface temperature is set equal to OAT. Air infiltration is 1 air change per hour (ach). Internal heat gains from people and lights are 10 W m^{-2} and 20 W m^{-2} respectively. Continuous operation of the HVAC system keeps the room air temperature equal to $20 \text{ }^{\circ}\text{C}$ during

building occupancy from 9:00 to 17:00. Fig. 1.4 shows the comparison of the space thermal loads between TUF-IOBES, BLAST, CBS-MASS, TARP, and BEM [26].

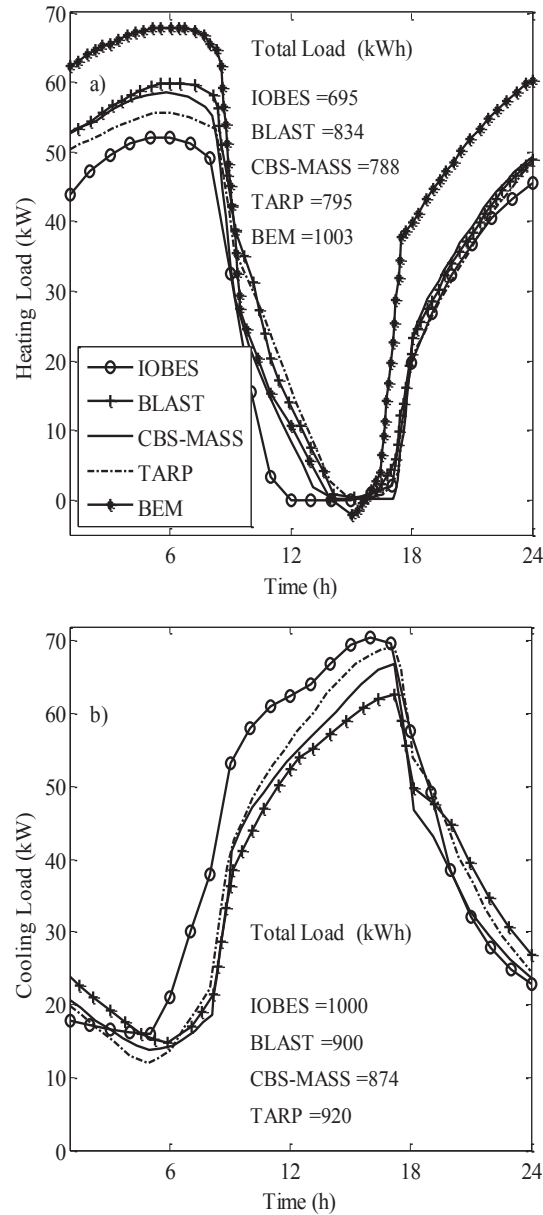


FIG. 1.4 Heating (a) and cooling (b) load comparison between TUF-IOBES, BLAST, CBS-MASS, TARP, and BEM (a only) for an office space on a winter (a) and summer (b) design day in Montreal. The total load from BEM was digitized from Fig. 5b in Salamanca et al. [26]

The comparisons show that the TUF-IOBES cooling and heating load is in close agreement with CBS-MASS, BLAST, TARP and BEM. TUF-IOBES relatively too warm underestimating the total daily heating load and overestimating the total daily cooling load on the design days. Despite an 8.7% difference in daily cooling load and a 12.5% difference in daily heating load between TUF-IOBES and TARP, the TUF-IOBES peak load is closer to TARP with a peak heating load difference of 3.69 kW (6.6%) and a peak cooling load difference of 1.52 kW (2.2%). On the other hand the difference in TARP and BLAST peak heating load is 4.96 kW (7.9%) and the difference in their peak cooling load is 5.84 kW (9.3%).

The differences between TUF-IOBES and other programs could stem from uncertainty in the material thermal and radiative properties which were not specified in the original reference. Also it is not clear that shortwave and longwave interaction between the building and surroundings are taken into account by Zmeureanu et al. [54].

1.3.3 Discussion

Overall the validation results indicate that TUF-IOBES performs well. TUF-IOBES accurately simulates an analytical case that demonstrates the performance of the conduction and interior heat balance components. Analytical testing of all components of the TUF-IOBES simulation is not possible due to the complexity of urban heat transfer. Instead, for heating loads TUF-IOBES is comparable to other standard building energy models. For cooling loads the inconsistent results between

the model intercomparison for BESTEST (TUF-IOBES smaller than other building energy models) and Zmeureanu et al. [54] (TUF-IOBES larger than other building energy models) indicate that TUF-IOBES does not have a fundamental bias; rather unknown parameter settings could explain the variable results. For example for BESTEST, window diffuse optical properties were unknown and set to 0.6 for diffuse transmittance, and 0.086 and 0.06 for diffuse absorptance of outer and inner panes, respectively. Diffuse optical properties have a greater effect on (summer) cooling loads than (winter) heating loads, since beam irradiance is the dominant radiative source term during the winter. So if the diffuse absorptance and/or transmittance were specified too small this could explain the reduction in cooling load.

1.4 TUF-IOBES application: effects of ground surface materials on building energy use

While this paper focuses on the description of TUF-IOBES, we briefly demonstrate an application of TUF-IOBES to study the effect of ground surface materials on building energy use. A detailed application of the model is presented in Yaghoobian and Kleissl [57].

1.4.1 Simulation setup

The effect of urban materials on building energy use and air quality in urban areas has received much attention (e.g. [58-60, 19]). Air temperature over urban surfaces with low albedo is higher than the air temperature over reflective materials,

which indirectly (through convective fluxes) affects urban building energy use. While this relationship holds for reflective roofs [20], reflective pavements have more complex effects due to their radiative interaction with surrounding building walls. The main objective of this initial study is to holistically evaluate local thermal and radiative effects of asphalt (representative of highly absorptive materials) and concrete (representative of more reflective materials) ground surfaces on building thermal loads. For this simulation a 5×5 identical building array is resolved by 99×99 identical patches of 3.05 m length (Fig. 1.5). Buildings have a square footprint of 21.33 m (7 patches) on each side and a height of 18.28 m (6 patches; 4 floors). The buildings in the domain are separated by 16 patches in both x and y directions (canyon aspect ratio of 0.38). The outputs are computed over the central building in the domain while the surrounding buildings provide appropriate radiative boundary conditions.

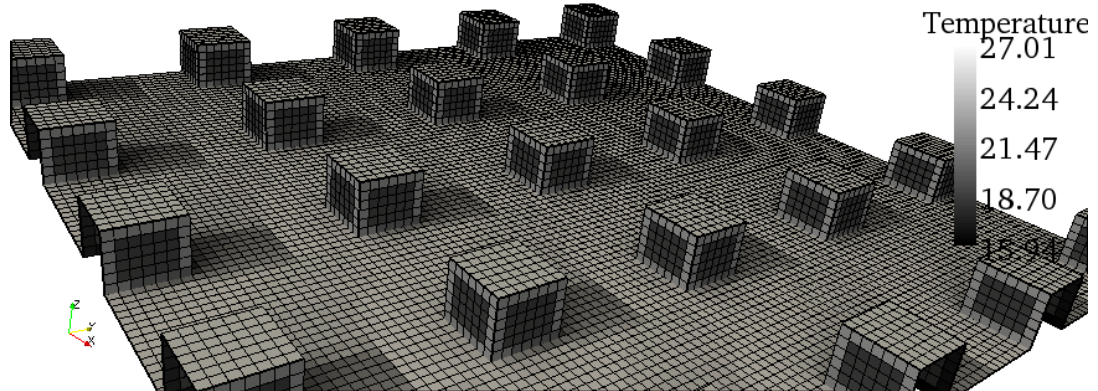


FIG. 1.5 Surface temperatures in the TUF-IOBES simulation domain with canopy aspect ratio of 0.38 at 1200 LST of January 1st in San Diego, CA. The length of each patch is 3.05 m. The center 4×5 patches of each façade are windows.

Building and system characteristics and the amounts of internal loads are chosen similar to the characteristics of prototypical post-1980 office buildings provided in Akbari et al. [20]. Each wall of the building has a double glazing window with dimensions 12.19 m (4 patches) height \times 15.24 m (5 patches) width resulting in a window fraction of 0.47. Every day from 0600 to 1900 LST each floor is occupied by 25 persons. Internal load from lighting is 15.07 W m^{-2} and from equipments is 16.14 W m^{-2} of floor area. The HCAV system operates continuously. Coefficient of performance (COP) of the HVAC system is 2.9 with cooling setpoint of 25.55°C and heating setpoint of 21.11°C . Infiltration is neglected. TMY3 weather data file for Miramar station (KNKX at 32.87° north latitude, 117.13° west longitude and 140 m altitude) in San Diego, California is used as forcing data at reference height. Properties of the building envelope and ground surface and sub-surface materials are presented in Tables 1.2 and 1.3. Deep soil temperature is the same in both asphalt and concrete cases and it is simulated based on TMY air temperature (Eq. 1.3).

TABLE 1.2 Building and ground material thickness and thermal and radiative properties by layer. Material properties are chosen based on Incropera and DeWitt [61] and examples in the ASHRAE toolkit.

Material layer	Thickness (m)	Conduct. (W/m/K)	Density (kg/m ³)	Spec. heat (kJ/kg/K)	Solar Abs. [-]	IR Emis. [-]
Walls						
Brick (outside)	0.10	1.3	2083	0.835	0.8	0.9
Insulation (R-13)	0.09	0.038	32	0.835	-	-
Drywall (inside)	0.013	0.17	800	1.09	0.65	0.9
Roof						
Asphalt	0.01	0.75	2110	0.92	0.4	0.9
Plywood	0.02	0.12	545	1.215	0.4	0.9
Plenum (air cavity)	0.1	0.026	1.205	1.005	-	-
Insulation (R-30)	0.2	0.038	32	0.835	-	-
Drywall (inside)	0.013	0.17	800	1.09	0.65	0.9
Floor						
Plywood (inside)	0.019	0.12	545	1.215	0.8	0.9
Concrete	0.07	1.51	2400	0.88	-	-
Crushed Rock	0.2	0.95	2000	1.05	-	-
Double-pane window						
Glass	0.009	0.74	2500	0.84	Table 1.3	0.9
Air	0.013	0.026	1.205	1.005	-	-
Glass	0.009	0.74	2500	0.84	Table 1.3	0.9
Ground surface						
Asphalt	0.07	0.75	2110	0.92	0.82	0.95
Concrete	0.07	1.51	2400	0.88	0.65	0.9
Ground sub-surface						
Crushed rock	0.2	0.95	2000	1.05	-	-

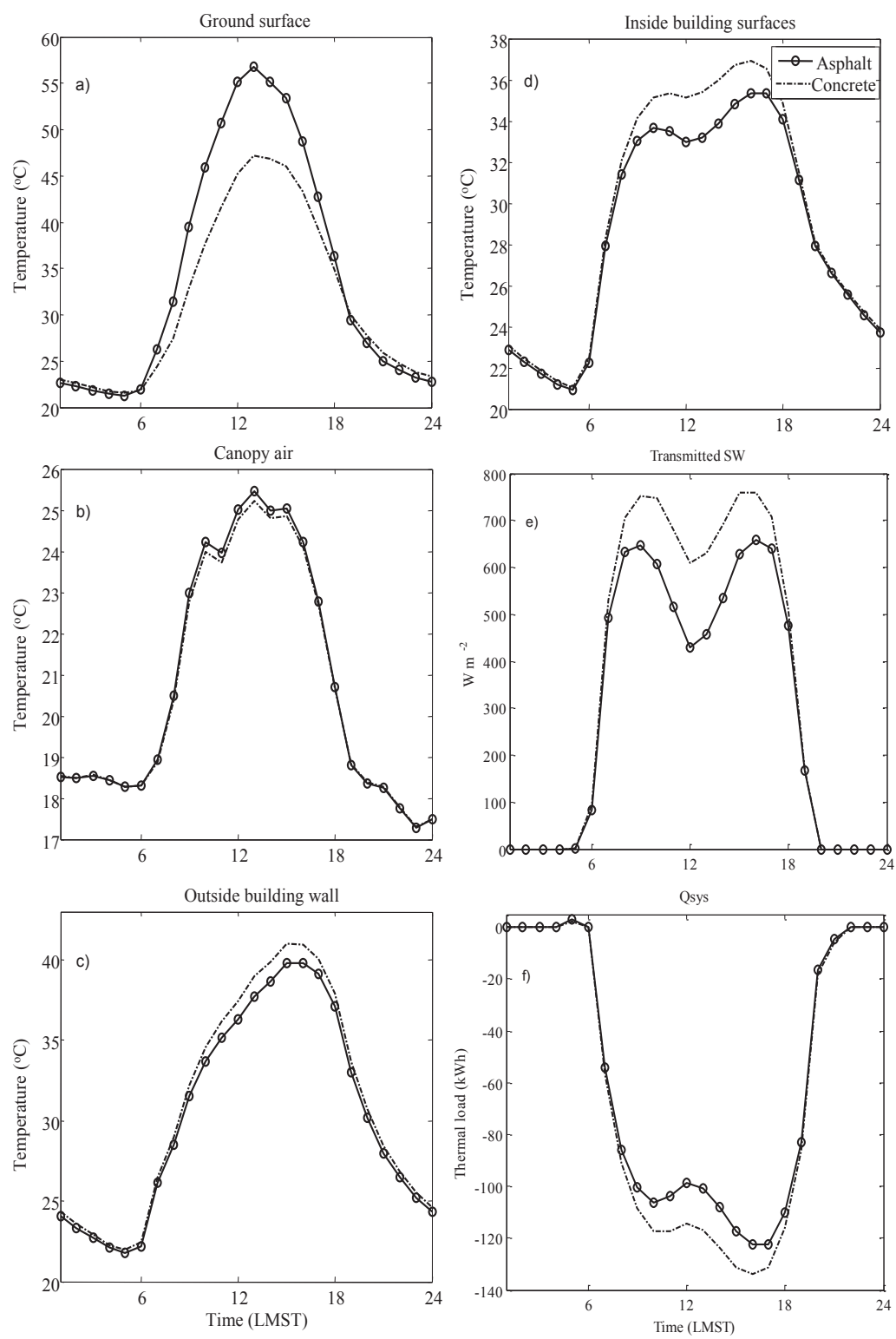
TABLE 1.3 Angular and diffuse Solar Heat Gain Coefficient (SHGC), absorptance and transmittance of window glass. Glass properties are chosen based on examples in the ASHRAE toolkit.

Incident Angle (Degree)	SHGC	Absorptance (1st pane)	Absorptance (2nd pane)	Transmittance
0	0.777	0.08	0.064	0.727
10	0.776	0.081	0.065	0.726
20	0.774	0.082	0.066	0.723
30	0.769	0.085	0.068	0.716
40	0.756	0.089	0.07	0.702
50	0.725	0.094	0.071	0.669
60	0.656	0.101	0.071	0.599
70	0.509	0.11	0.065	0.455
80	0.261	0.117	0.049	0.215
90	0	0	0	0
Diffuse	0.676	0.093	0.067	0.623

1.4.2 Results and Discussion

Fig. 1.6 shows a comparison of temperatures of ground surface, canopy air, outside building wall, inside building surfaces with the transmitted shortwave radiation into the building and hourly thermal loads for July 10th (a clear day with average wind speed of 3 m s⁻¹) between the simulations using asphalt and concrete ground surfaces. Roof surface temperature is not shown since in TUF-IOBES it is independent of the ground surface material.

FIG. 1.6 Comparison of a) ground surface, b) canopy air, c) outside building wall and d) inside building surface temperatures, e) transmitted shortwave radiation into the building, and f) hourly thermal loads for asphalt and concrete ground surface material for a summer day (July 10th) in San Diego, California. Outside building wall temperature is averaged over all four outside walls excluding windows. Inside building surface temperature is the average temperature of all surface temperatures inside the building excluding windows.



The difference in albedo and (less so) other material thermal properties causes a higher ground surface temperature on asphalt than concrete with the maximum difference of 9.9 °C. Since TUF-IOBES assumes perfect advection from inside the canopy to the atmospheric surface layer, the air temperature above the asphalt is only up to 0.25 °C higher than that over concrete surface. Ground surface materials affect building surfaces directly (through radiation) and indirectly (through convection). Fig. 1.6c shows that despite the higher ground surface temperature and canopy air temperature over asphalt, building walls are cooler (with maximum difference of 1.24 °C) than over concrete. With the simpler TUF3D model, Yaghoobian et al. [32] similarly demonstrated that the thermal exchange between ground surfaces and walls is dominated by the effects of net shortwave radiation. Consequently, the larger building wall temperature over concrete is directly related to the higher albedo of concrete (0.35) than asphalt (0.18). Higher reflection from concrete also results in a 19.8% increase in total transmitted shortwave radiation into the building (Fig. 1.6e). Together, the larger transmitted shortwave radiation and larger heat conduction through the building envelope result in larger inside building wall (Fig. 1.6d) and indoor air temperatures. The contribution of transmitted shortwave radiation through windows on indoor temperatures is larger than the effects of conductive heat transfer through the building envelope (Fig. 1.6c, 2.6e). Consequently, the daily AC energy use to keep the indoor air temperature at the cooling setpoint increases 10.2% for the concrete ground surface (Fig. 1.6f).

During the winter the same processes cause a reduction in heating load over concrete. The total yearly cooling energy use for concrete is 7.5% (31 MWh) larger

and total yearly heating energy use is 4.1% (0.9 MWh) smaller than over an asphalt surface. While the relative increases are similar the absolute magnitude of cooling energy use increase trumps the heating load savings resulting in an overall increase in building energy use near more reflective ground materials. These results differ from previous research. Other researchers focused on the increase in *air* temperature over dark surfaces compared to reflective surfaces ignoring the effect of reflected solar radiation on nearby buildings. This approach is justified for cool roofs, but inappropriate for cool pavement studies. Ground surface materials affect buildings both directly and indirectly and TUF-IOBES results show that in above scenario direct radiative effects are locally dominant.

1.5 Conclusion

An indoor-outdoor dynamically coupled urban model has been presented. The Temperature of Urban Facets Indoor-Outdoor Building Energy Simulator (TUF-IOBES) provides scientific and engineering results with policy relevance, for example by studying the holistic impact of heat island mitigation measures. TUF-IOBES was validated against analytical heat transfer results and against previously validated and well-known building energy models. Results of these carefully conducted tests indicate that TUF-IOBES can accurately simulate the thermal behavior of a building. Simulations of annual thermal loads on about two days of a single processor are possible in this two-way coupled model. The effect of a large number of parameters such as building conditions (e.g. infiltration rate, construction materials, window size

and type), canopy aspect ratio, and weather type (very hot and cold cities) on building thermal loads can be investigated [57].

TUF-IOBES is one of the first three-dimensional fully-coupled indoor-outdoor building energy simulators. Given the complexity of solar irradiance fields in the urban canopy the surface temperature fields and energy use can be simulated more faithfully. TUF-IOBES provides unprecedented insight into urban canopy and building energy heat transfer processes. It can improve our understanding of how urban geometry and material modifications and the interaction between buildings and their surroundings and dynamic combination of all of these effects in three dimensions modify urban energy use. Additional capabilities need to be developed such as more flexible model geometry to accommodate any possible building and canyon shape, more sophisticated HVAC system models, more sophisticated models for simulating vegetated surfaces (other than using Bowen ratio in Yaghoobian et al. [32]) and the water balance in urban areas. The TUF-IOBES outdoor convection model is simplistic albeit no more so than in other building energy models. Also, the feedback of changes in the urban canopy and anthropogenic heat release onto the atmospheric surface layer cannot be simulated, since the boundary conditions are imposed in the surface layer. In this case, models that can simulate the full boundary layer and mesoscale effects are more applicable (e.g. WRF-Urban [27]; Krayenhoff and Voogt [62]).

Acknowledgements

We thank (i) Scott Krayenhoff (University of British Columbia) for providing the TUF3D model, (ii) Chunsong Kwon (University of California, San Diego) for his contribution in importing TMY file into TUF-IOBES, (iii) Ron Judkoff and Joel Neymark in National Renewable Energy Laboratory for providing BESTEST weather data. (iv) Funding from a National Science Foundation CAREER award.

The text and data in chapter 1, in full, is a reprint of the material as it appears in “An indoor–outdoor building energy simulator to study urban modification effects on building energy use – Model description and validation”, Yaghoobian, Neda; Kleissl, Jan, *Energy and Buildings*, 54, 407–417 (2012). The dissertation author is the primary investigator and author of this article.

Appendix

TABLE 1.A1 Building element thermal properties and thickness by layer for cooling and heating load validations against an intermediate floor office in Zmeureanu et al. [54]. For simplicity floor construction is chosen to be the same as roof.

Building layer	Thickness (m)	Conduct. (W/m/K)	Density (kg/m ³)	Spec. heat (kJ/kg/K)	Solar Abs. [-]	IR Emis. [-]
Walls						
Concrete (outside)	0.1	1.51	2400	0.88	0.7	0.9
Air cavity	0.025	0.026	1.205	1.005	-	-
Insulation	0.1	0.039	32	0.835	-	-
Gypsum board (inside)	0.02	0.14	760	0.8	0.3	0.9
Roof & Floor						
Plywood	0.038	0.12	545	1.215	0.8	0.9
Plenum (air cavity)	0.1	0.026	1.205	1.005	-	-
Insulation (R-30)	0.2	0.038 32	0.835	-	-	
Drywall	0.013	0.17	800	1.09	0.65	0.9
Double-pane window						
Glass	0.009	0.74	2500	0.84	0.8	0.9
Air	0.008	0.026	1.205	1.005	-	-
Glass	0.009	0.74	2500	0.84	0.8	0.9

References

- [1] R.E. Britter, S.R. Hanna, Flow and dispersion in urban areas, *Annual Review of Fluid Mechanics* 35 (2003) 469–496.
- [2] M.O. Letzel, M. Krane, S. Raasch, High resolution urban large-eddy simulation studies from street canyon to neighbourhood scale, *Atmospheric Environment* 42 (2008) 8770–8784.
- [3] G.T. Johnson, T.R. Oke, T.J. Lyons, D.G. Steyn, I.D. Watson, J.A. Voogt, Simulation of Surface Urban Heat Islands under ‘Ideal’ Conditions at Night. Part I: Theory and Tests Against Field Data, *Boundary Layer Meteorology* 56 (1991) 275–294.
- [4] G.M. Mills, Simulation of the Energy Budget of an Urban Canyon-I. Model Structure and Sensitivity Test, *Atmospheric Environment* 27(1993) 157–170.
- [5] J. Arnfield, J.M. Herbert, G.T. Johnson, A Numerical Simulation investigation of Urban Canyon Energy Budget Variations, in *Proceedings of 2nd AMS Urban environment Symposium* (1998).
- [6] V. Masson, A physically based scheme for the urban energy budget in atmospheric models, *Boundary Layer Meteorology* 94 (2000) 357–397.
- [7] C.S.B. Grimmond, T.R. Oke, H.A. Cleugh, The role of ‘rural’ in comparisons of observed suburban–rural flux differences. Exchange processes at the land surface for a range of space and time scales, *International Association of Hydrological Sciences Publication* 212 (1993) 165–74.
- [8] T.R. Oke, The surface energy budget on urban areas. *Modeling the Urban Boundary Layer*, American Meteorological Society, 1987, pp. 1–52
- [9] Y. Kikegawa, Y. Genchi, H. Yoshikado, H. Kondo, Development of a numerical simulation system toward comprehensive assessments of urban warming countermeasures including their impact upon the urban buildings’ energy-demands, *Applied Energy* 76 (2003) 449–466.
- [10] Y. Kikegawa, Y. Genchi, H. Kondo, K. Hanaki, Impacts of city-block-scale countermeasures against urban heat island phenomena upon a building’s energy-consumption for air conditioning, *Applied Energy* 83 (2006) 649–668.
- [11] A. Krpo, F. Salamanca, A. Martilli, A. Clappier, On the impact of anthropogenic heat fluxes on the urban boundary layer: a two-dimensional numerical study, *Boundary Layer Meteorology* 136 (2010) 105–127.

- [12] C.S.B. Grimmond, M. Best, J. Barlow, A.J. Arnfield, J.J. Baik, S. Belcher, M. Bruse, I. Calmet, F. Chen, P. Clark, A. Dandou, E. Erell, K. Fortuniak, R. Hamdi, M. Kanda, T. Kawai, H. Kondo, S. Krayenhoff, S.H. Lee, S.B. Limor, A. Martilli, V. Masson, S. Miao, G. Mills, R. Moriwaki, K. Oleson, A. Porson, U. Sievers, M. Tombrou, J. Voogt, T. Williamson, Urban surface energy balance models: model characteristics and methodology for a comparison study. *Meteorological and Air Quality Models for Urban Areas*, A.Baklanov et al., Eds., Springer-Verlag, 2009, 97-124.
- [13] C.S.B. Grimmond, M. Blackett, M.J. Best, J. Barlow, J.J. Baik, S.E. Belcher, S.I. Bohnenstengel, I. Calmet, F. Chen, A. Dandou, K. Fortuniak, M.L. Gouvea, R. Hamdi, M. Hendry, T. Kawai, Y. Kawamoto, H. Kondo, E.S. Krayenhoff, S.H. Lee, T. Loridan, A. Martilli, V. Masson, S. Miao, K. Oleson, G. Pigeon, A. Porson, Y.H. Ryu, F. Salamanca, L. Shashua-Bar, G.J. Steeneveld, M. Tombrou, J. Voogt, D. Young, N. Zhang, The International Urban Energy Balance Models Comparison Project: First results from Phase 1, *Journal of Applied Meteorology and Climatology* 49 (2010) 1268–1292.
- [14] D.J. Sailor, A review of methods for estimating anthropogenic heat and moisture emissions in the urban environment, *International Journal of Climatology* 31 (2011) 189–199.
- [15] M.J. Best, Progress towards better weather forecasts for city dwellers: from short range to climate change, *Theoretical and applied climatology* 84 (2006) 47-55.
- [16] M.P. McCarthy, M.J. Best, R.A. Betts, Climate change in cities due to global warming and urban effects, *Geophysical Research Letters*, 37, L09705 (2010) 1-5.
- [17] H. Taha, D. Sailor, H. Akbari, High-albedo materials for reducing building cooling energy use, Rep. LBL-3172L Lawrence Berkeley Laboratory, Berkeley, CA, 1992.
- [18] H. Taha, Urban climates and heat islands: Albedo, evapotranspiration, and anthropogenic heat, *Energy and Buildings* 25 (1997) 99-103.
- [19] H. Akbari, M. Pomerantz, H. Taha, Cool surfaces and shade trees to reduce energy use and improve air quality in urban areas, *Solar Energy* 70 (2001) 295–310.
- [20] H. Akbari, S. Konopacki, Calculating energy-saving potentials of heat-island reduction strategies, *Energy Policy* 33 (2005) 721–756.
- [21] H. Shen, H.W. Tan, T. Athanasios, The effect of reflective coatings on building surface temperatures, indoor environment and energy consumption—An experimental study, *Energy and Buildings* 43 (2011) 573-580.

- [22] U.S. DOE. EnergyPlus - Engineering reference. <http://apps1.eere.energy.gov/buildings/energyplus/pdfs/engineeringreference.pdf> last accessed on April 26, 2011.
- [23] C.O. Pedersen, R.J. Liesen, R.K. Strand, D.E. Fisher, L. Dong, P.G. Ellis, A toolkit for building load calculations; Exterior heat balance (CD-ROM), American Society of Heating, Refrigerating and Air Conditioning Engineers (ASHRAE), Building Systems Laboratory, 2001.
- [24] G.N. Walton, Thermal Analysis Research Program Reference Manual. NBSSIR 83- 2655. National Bureau of Standards, Washington, DC, 1983.
- [25] C.S.B. Grimmond, M. Blackett, M.J. Best, J.J. Baik, S.E. Belcher, J. Beringer, S.I. Bohnenstengel, I. Calmet, F. Chen, A. Coutts, A. Dandou, K. Fortuniak, M.L. Gouvea, R. Hamdi, M. Hendry, M. Kanda, T. Kawai, Y. Kawamoto, H. Kondo, E.S. Krayenhoff, S.H. Lee, T. Loridan, A. Martilli, V. Masson, S. Miao, K. Oleson, R. Ooka, G. Pigeon, A. Porson, Y.H. Ryu, F. Salamanca, G.J. Steeneveld, M. Tombrou, J.A. Voogt, D. Young, N. Zhang, Initial results from Phase 2 of the international urban energy balance model comparison, *International Journal of Climatology* 31 (2011) 244–272.
- [26] F. Salamanca, A. Krpo, A. Martilli, A. Clappier, A new building energy model coupled with an urban canopy parameterization for urban climate simulations—part I. formulation, verification, and sensitivity analysis of the model, *Theoretical and applied climatology* 99 (2010) 331-344.
- [27] F. Chen, H. Kusaka, R. Bornstein, J. Ching, C.S.B. Grimmond, S. Grossman-Clarke, T. Loridan, K.W. Manning, A. Martilli, S. Miao, D. Sailor, F.P. Salamanca, H. Taha, M. Tewari, X. Wang, A.A. Wyszogrodzki, C. Zhang, The integrated WRF/urban modeling system: development, evaluation, & applications to urban environmental problems, *International Journal of Climatology* 31 (2011) 273–288.
- [28] B. Bueno, L. Norford, G. Pigeon, R. Britter, Combining a Detailed Building Energy Model with a Physically-Based Urban Canopy Model, *Boundary Layer Meteorology* 140 (2011) 471–489.
- [29] J. Bouyer, C. Inard, M. Musy, Microclimatic coupling as a solution to improve building energy simulation in an urban context, *Energy and Buildings* 43 (2011) 1549-1559.
- [30] Fluent, Fluent 6.3 User Guide, Fluent Inc., Centerra Resource Park, 10 Cavendish Court, Lebanon, NH 03766, USA, 2006.
- [31] E.S. Krayenhoff, J.A. Voogt, A microscale threedimensional urban energy balance model for studying surface temperatures, *Boundary Layer Meteorology* 123 (2007) 433–46.

- [32] N. Yaghoobian, J. Kleissl, E.S. Krayenhoff, Modeling the thermal effects of artificial turf on the urban environment, *Journal of Applied Meteorology and Climatology* 49 (2010) 332–345.
- [33] D. Brown, An Improved Meteorology for Characterizing Atmospheric Boundary Layer Turbulence Dispersion, Ph.D. Thesis, Department of Mechanical and Industrial Engineering, University of Illinois, Urbana, IL, 1997.
- [34] F.C. McQuiston, D.J. Parker, J.D. Spitler, *Heating Ventilating and Air Conditioning*, John Wiley & Sons Inc., New York, 2000.
- [35] F. Haghighat, H. Liang, Determination of Transient Heat Conduction through Building Envelops-A review. *ASHRAE Transactions*, 98: No. 1, 1992, pp. 284-290.
- [36] M.G. Davies, Transmission and Storage Characteristics of Sinusoidally Excited Walls-A review, *Applied Energy* 15 (1983) 167-231.
- [37] P.T. Lewis, D.K. Alexander, HTB2: A Flexible Model for Dynamic Building Simulation, *Building and Environment* 25 (1990) 7-16.
- [38] J.A. Clarke, *Energy Simulation in Building Design*, Adam Hilger Ltd., Boston, 1985.
- [39] J.R. Waters, A.J. Wright, Criteria for the Distribution of Nodes in Multi-layer Walls in Finite Difference Thermal Modeling, *Building and Environment* 20 (1985) 151-162.
- [40] D.C. Hittle, *Response Factors and Conduction Transfer Functions*, Unpublished, 1992.
- [41] J.E. Seem, Modeling of Heat Transfer in Buildings, Ph.D. Thesis, University of Wisconsin, Madison, WI, 1987.
- [42] J. Seem, S. Klein, Transfer functions for efficient calculation of multidimensional transient heat transfer, *Journal of Heat Transfer* 111 (1989) 5–12.
- [43] D. Hillel, *Introduction to soil physics*. Academic Press, San Diego, CA, 1982.
- [44] J. Wu, D.L. Nofziger, Incorporating temperature effects on pesticide degradation into a management model, *Journal of Environmental Quality* 28 (1999) 92-100.
- [45] B.M. Caruta, *New Developments in Materials Science research*, Nova Science publisher, Inc., 2007.
- [46] D.A. Vries De, Thermal properties of soils. In Van Wijk, W. R. (ed.), *Physics of Plant Environment*, North-Holland Publishing Co., Amsterdam, 1963.

- [47] S.S. Zilitinkevich, Non-local turbulent transport: pollution dispersion aspects of coherent structure of convective flows. In: H. Power, N. Moussiopoulos, and C.A. Brebbia (eds.), *Air pollution III – Volume I. Air pollution theory and simulation*, Computational Mechanics Publications, Southampton, Boston, 1995, pp 53–60.
- [48] E. Guilloteau, Optimized computation of transfer coefficients in surface layer with different momentum and heat roughness length, *Boundary Layer Meteorology* 87 (1998) 147–160.
- [49] R.J. Cole, N.S. Sturrock, The Convective Heat Exchange at the External Surface of Buildings, *Building and Environment* 12 (1977) 207-214.
- [50] M. Yazdanian, J.H. Klems, Measurement of the Exterior Convective Film Coefficient for Windows in Low-Rise Buildings. *ASHRAE Transactions*, Vol. 100, Part 1, 1994.
- [51] G.N. Walton, Passive Solar Extension of the Building Loads Analysis and System Thermodynamics (BLAST) Program, Technical Report, United States Army Construction Engineering Research Laboratory, Champaign, IL, 1981.
- [52] Lawrence Berkeley Laboratory (LBL), DOE2.1E-053 source code, 1994.
- [53] G.N. Walton, Algorithm for Calculating Radiation View Factors Between Plane Convex Polygons With Obstructions, National Bureau of Standards, NBSIR 86-3463, (1987--- shortened report in *Fundamentals and Applications of Radiation Heat Transfer*, HTD-Vol. 72, American Society of Mechanical Engineers), 1987.
- [54] R. Zmeureanu, P. Fazio, F. Haghighat, Analytical and interprogram validation of a building thermal model, *Energy and Buildings* 10 (1987) 121–133.
- [55] A.W. Pratt, *Heat Transmission in Buildings*, John Wiley and Sons Ltd, 1981.
- [56] R. Judkoff, J. Neymark, *Building Energy Simulation Test (BESTEST) and Diagnostic Method*, National Renewable Energy Laboratory, Golden, Colorado, 1995.
- [57] N. Yaghoobian, J. Kleissl, *Effect of Reflective Pavements on Building Energy Use*, 2012, Submitted to *Urban Climate*.
- [58] A.H. Rosenfeld, H. Akbari, S. Bretz, B.L. Fishman, D.M. Kurn, D. Sailor, H. Taha, Mitigation of urban heat islands: materials, utility programs, updates, *Energy and Buildings* 22 (1995) 255–265.
- [59] S. Bretz, H. Akbari, A. Rosenfeld, Practical issues for using solar-reflective materials to mitigate urban heat islands, *Atmospheric Environment* 32 (1998) 95–101.

- [60] L. Doulos, M. Santamouris, I. Livada, Passive cooling of outdoor urban spaces, The role of materials, *Solar Energy* **77** (2004) 231–249.
- [61] F.P. Incropera, D.P. DeWitt, *Fundamentals of Heat and Mass Transfer* 5th Edition, John Wiley & Sons, 2001.
- [62] E.S. Krayenhoff, J.A. Voogt, Impacts of Urban Albedo Increase on Local Air Temperature at Daily–Annual Time Scales: Model Results and Synthesis of Previous Work, *Journal of Applied Meteorology and Climatology* 49 (2010) 1634–1648.

Chapter 2

Effect of reflective pavements on building energy use

Full reprint from *Urban Climate* 2 (2012) 25–42, 2012

Optimization of building energy use in an urban area requires understanding of the complex interaction between urban morphology, materials, and climate, which can have unanticipated effects on urban microclimates and building energy use. Reflective pavements reduce urban air temperatures and have been proposed as a mitigation measure for urban heat islands. However, the increased solar reflectivity also transports more solar radiation into (through windows) and onto adjacent buildings possibly increasing building energy use. The effect of albedo changes in the urban canopy floor surface on building thermal loads is investigated using the Temperature of Urban Facets Indoor-Outdoor Building Energy Simulator (TUF-IOBES). A case study for a four storey office building with 1820 m² floor area and 47% window to wall ratio in Phoenix, Arizona was conducted. Increasing pavement solar reflectivity from 0.1 to 0.5 increased annual cooling loads up to 11% (33.1 kWh m⁻²). The impacts on annual heating loads and canopy air temperatures were small. The confounding impacts of canopy aspect ratio, building insulation conditions reflective of building age, and window type and size were also quantified. Policymakers should carefully weigh the benefits and local energy use implications of reflective pavements for each site to ensure their optimal application.

2.1 Introduction

The microclimate generated by the urban surfaces on and around a building affects human comfort and building energy use. Material properties, anthropogenic heat, geometry, and urban landscape features alter surface temperatures and energy

fluxes between the ground and the atmosphere. For instance buildings close to parks or especially areas with abundant reflective roofs [1] are exposed to cooler air than buildings in areas with predominantly (low albedo) asphalt surfaces. Reflective building roofs reduce shortwave absorption during the day decreasing the surface temperature and urban air temperature which leads to reduced building energy use in most U.S. climates [2]. Bouyer et al. [3] numerically showed the importance of considering the local condition and microclimate in building energy analysis. Radiative, conductive and convective properties of construction materials and the urban form (e.g. [4]) can be engineered or selected to achieve different urban climate objectives. The effects of urban heat island mitigation measures such as increases in albedo and urban greeneries on building energy use and air quality have been investigated (e.g. [5-16]) previously. Urban planning, policy and code development, however, often occur with little consideration for the atmospheric environment impacts of development, and mitigation measures have heretofore been based on limited analysis of the potential suite of interacting impacts.

Consequently, urban design needs to consider these interactions and impacts of urban heat island mitigation strategies need to be analyzed carefully with appropriate modeling tools and computational resources. Just like global climate, urban climate is a complex system where changing one parameter or process will trigger positive and negative feedback effects that require holistic simulation of the physical and meteorological processes.

The success of ‘cool’ (reflective) roofs caused cool-roof building codes and incentive programs to sprout around the country (e.g. [17]). UHI researchers and

politicians now propose that reflective pavements should be the next step in reducing urban air temperatures (and associated air quality) and energy use. The Heat Island and Smog Reduction Act of 2011 (Bill H.R.51 [18]) requires “high solar reflectivity (cool) roofs, vegetated roofs, and paving materials with higher solar reflectivity”. Assembly Bill 296 in California [19] is specifically designed to advance cool pavement practices in the state and requires compilation of a Cool Pavement Handbook.

However, reflective pavements may actually increase building energy use through reflection of solar radiation onto building walls and into buildings through windows. For example, Yaghoobian et al. [20] showed that artificial turf (the “anti-reflective pavement” with an albedo of 0.08) while being warmer than grass actually reduced local urban energy use for a San Diego building compared to grass surfaces because it reduces reflection of sunlight onto adjacent building surfaces. Pearlmutter et al. [21] and Erell [22] found that streets with lighter-colored walls generated a slightly higher total pedestrian heat gain, which was attributed to increased pedestrian exposure to shortwave radiation reflected from the walls. These increases outweighed the longwave radiative reductions due to lower wall temperature. Sailor’s conference presentation covered a very similar topic to the present study [23].

In this paper we investigate the holistic physical interaction between buildings and the surrounding microclimate in the urban canyon. An advanced urban heat transfer / meteorological model is applied to investigate how the albedo of the canopy floor surface impacts building energy use for heating and cooling. Twenty three different cases considering different canopy floor surface albedo and different canopy

aspect ratios for two building types representing more and less energy-efficient buildings are simulated. Also the effects of window-to-wall ratio (WWR) and reflective mirrored windows are investigated. The Temperature of Urban Facets Indoor-Outdoor Building Energy Simulator (TUF-IOBES, [24]) is applied for these simulations. The setup of these simulations is described in Section 2.2. Simulation results are presented and discussed in Section 2.3 followed by the conclusions in Section 2.4.

2.2 Simulation setup

2.2.1 Temperature of Urban Facets Indoor-Outdoor Building Energy Simulator (TUF-IOBES)

TUF-IOBES was described and validated in detail in Yaghoobian and Kleissl [24]. It is a building-to-canopy model that solves energy balance equations to simulate indoor and outdoor building surface temperatures and heat fluxes in a three-dimensional urban area. The indoor and outdoor energy balance processes are dynamically coupled taking into account weather conditions, indoor heat sources, building and urban material properties, composition of the building envelope (e.g. windows, insulation), and HVAC equipment. TUF-IOBES is also capable of simulating effects of the waste heat from air-conditioning systems on urban canopy air temperature [24]. Canopy air temperature is simulated using an energy balance considering convective sensible heat fluxes from all surfaces in the canopy into the canopy air and the convective heat flux exchanged between canopy and above canopy.

The latter is based on the air temperature difference between these two layers. Since the air temperature above the canopy layer is imposed as a boundary condition, it is not affected by anthropogenic heat release and the canopy air temperature; in other words it is assumed that the heat flux from inside the canopy to the atmospheric surface layer is removed from the simulation domain. A version of TUF-IOBES is employed here with outdoor convection described by the DOE-2 model [25], the interior convection model is the ASHRAE default method, and the infiltration and ventilation model is the simple air change per hour model [26].

2.2.2 Physical Building Setup and Thermal Properties

The TMY3 weather data file for Phoenix Sky Harbor International Airport (33.45° north latitude, 111.983° west longitude and 337 m altitude) in Arizona, US, is used as forcing data at reference height. Phoenix presents an interesting case because it is a large urban development representative of the desert southwest, where reflective pavements are likely to be applied and have large effects. Also relative to other urban areas, Phoenix has a long history in urban climate research and a large body of academic work exists on the Phoenix UHI that has informed urban policy [27].

The domain geometry consists of 5×5 identical detached buildings and extends vertically from the deep soil to the reference height in the atmospheric surface layer (Fig. 2.1). Buildings have square footprints of 21.3 m on each side and heights of 18.3 m (4 storeys). Intermediate floors and internal mass are not considered. Each wall has a window centered on the wall with dimensions of 12.2 m height \times 15.2 m width

resulting in a window fraction of 0.47. The effects of curtains, blinds, or outside sunshades are not considered (see Section 2.3.3 for a detailed discussion of modeling assumptions).

Thermal properties follow prototypical post and pre-1980 office buildings suggested in Akbari et al. [2] which respectively satisfy and do not satisfy insulation requirements for nonresidential buildings in ASHRAE 90.1-2004 [28] (Table 2.1). Pre (post) -1980 buildings have R-11 (R-30) roof insulation and R-6 (R-13) wall insulation. Floor construction is based on best guesses and is made of a layer of plywood over a concrete slab followed by a layer of crushed rock and is chosen the same for both types of buildings. Reflective roof surfaces are used in both building types with a solar reflectance of 0.6, i.e. re-roofing is assumed to have occurred in pre-1980 buildings. Triple-pane clear 1 Low-E layer (clear single-pane) windows with overall Solar Heat Gain Coefficient (SHGC) of 0.22 (0.72) and overall U-factor of 1.25 (5.6) $\text{W m}^{-2} \text{K}^{-1}$ are chosen for post (pre)-1980 buildings. The triple pane windows were chosen to meet ASHRAE Standard 90.1-99 and are considered typical for new construction [29]. Properties of the building envelope and ground materials used in all simulations are presented in Table 2.1. Angular and diffuse SHGC, absorptance and transmittance of window glasses derived from the WINDOW v7.0.68.0 software [30] are shown in Table 2.2.

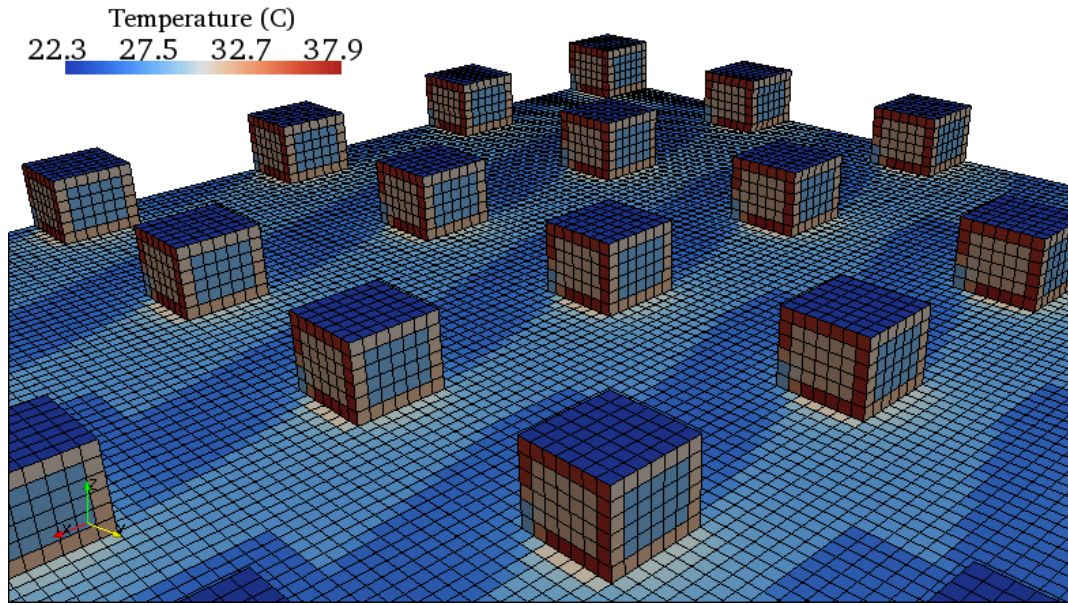


FIG. 2.1 Surface temperatures in the TUF-IOBES simulation domain for canopy aspect ratio of 0.37, ground surface albedo of 0.3, and pre-1980 buildings at 0600 LST of July 15th in Phoenix, AZ. The length of each patch is 3.05 m. The center 4×5 patches of each façade are windows.

2.2.3 HVAC System

In both types of buildings every day from 0600 to 1900 LST the occupancy is 75 persons per floor ($0.16 \text{ person m}^{-2}$) and internal loads from lighting and equipments are 15.1 W m^{-2} and 16.1 W m^{-2} of floor area. Continuous HVAC operation is assumed. The heat transfer to/from the HVAC system satisfies the air heat balance (the convective heat transfer from the zone surfaces, convective contribution of internal loads, and the sensible load due to infiltration and ventilation) to keep the room air temperature between 21.1°C and 25.6°C heating and cooling setpoints [31], respectively. The air conditioning equipment is chosen as ‘air conditioners, air cooled’ based on Akbari et al. [2]. Since in ASHRAE 90.1-2004 the required ‘minimum efficiency’ is 10.1 and 10.3 EER (~ 2.9 and 3.0 COP), the Coefficient of performance

(COP) of the cooling system in both types of buildings is chosen as 2.9 consistent with Akbari et al. [2] for post-1980 buildings. An efficiency of 1 is assumed for the (electric) heating supply. Using ANSI/ASHRAE Standard 62.1-2007 [32] (outdoor air rate in office spaces of $0.0023 \text{ m}^3 \text{ s}^{-1} \text{ person}^{-1}$ people and $3.04 \times 10^{-4} \text{ m}^3 \text{ s}^{-1} \text{ m}^{-2}$ area) the minimum required outdoor airflow in both types of buildings is 0.55 air changes per hour (ACH).

2.2.4 Scenarios for ground surface albedo, canopy aspect ratio, and window fraction

To study the interactive effects of different urban mitigation strategies on building energy use three different canopy aspect ratios (the building height (H) divided by the distance between buildings (W)) (0.37, 1.0, 1.5) in both x and y directions and three different canopy ground surface albedos (0.1, 0.3, 0.5) are used while the building wall albedo is kept constant at 0.3. Canopy aspect ratio directly and non-linearly modulates the effect of reflective pavements so the two parameters have to be investigated jointly. Increased shading for large aspect ratios makes reflective materials less effective. The ground surface albedo choices are motivated by data from the American Concrete Pavement Association [33] for weathered materials: asphalt 0.1 – 0.15; gray portland cement concrete 0.2 – 0.3; white portland cement concrete 0.4 – 0.6.

To study the effects of window to wall fraction which varies significantly in office buildings, a sensitivity test for the case with $H/W = 1$ and ground surface

albedo of 0.5 is conducted considering a smaller (0.24) and a larger (0.66) window to wall fraction. Also since many office buildings have reflective mirrored windows, for one case in a canopy with $H/W = 0.37$ and ground surface albedo of 0.5 the effects of double-pane reflective mirrored windows are compared with the triple-pane clear windows in post-1980 buildings. The overall SHGC of the reflective window is chosen to be close to that of typical reflective windows in Phoenix, AZ [29] (Table 2.A2).

TABLE 2.1 Building and ground material thickness, and thermal and radiative properties by layer for pre and post-1980 buildings. Properties of the single pane window are for a product named 'Clear-6 / .090 PVB / Clear-6' manufactured by 'Cardinal Glass Industries' [30]. Triple pane windows are made of a clear low-e glass named 'LoE² 240 on 6mm Clear' manufactured by 'Cardinal Glass Industries' and 2 layers of 'Generic Clear Glass' [30]. Properties of reflective windows are provided in Table 2.A1.

Material layer	Thickness (m)	Conduct. (W/m/K)	Density (kg/m ³)	Spec. heat (kJ/kg/K)	Solar Abs. [-]	IR Emis. [-]
Walls						
Brick (outside)	0.10	1.3 ^[34]	2083 ^[34]	0.835 ^[34]	0.7 ^[35]	0.9 ^[35]
Insulation (R-6) (Pre)	0.044	0.042 ^b	32 ^[34]	0.835 ^[34]	-	-
Insulation (R-13)(Post)	0.089	0.038 ^b	32 ^[34]	0.835 ^[34]	-	-
Drywall-Gypsum (inside)	0.013 ^[2]	0.17 ^[34]	800 ^[34]	1.05 ^[35]	0.65 ^a	0.95 ^a
Roof						
Plywood	0.019 ^[2]	0.12 ^[34]	545 ^[34]	1.215 ^[34]	0.4 ^[2]	0.9 ^[2]
Plenum (air cavity)	0.1	0.025 ^[36]	1.205 ^[36]	1.005 ^[36]	-	-
Insulation (R-11) (Pre)	0.089	0.045 ^b	32 ^[34]	0.835 ^[34]	-	-
Insulation (R-30)(Post)	0.2	0.038 ^b	32 ^[34]	0.835 ^[34]	-	-
Drywall-Gypsum (inside)	0.013 ^[2]	0.17 ^[34]	800 ^[34]	1.05 ^[35]	0.65 ^a	0.95 ^a
Floor						
Plywood (inside)	0.019	0.12 ^[34]	545 ^[34]	1.215 ^[34]	0.8 ^a	0.9 ^[2]
Concrete	0.07	1.51 ^[35]	2400 ^[35]	0.88 ^[35]	-	-
Crushed rock	0.2	0.95 ^[37]	1200 ^a	1.05 ^a	-	-
Window						
Triple-pane (Post)						
Glass (Clear Low-E)	0.0057 ^[30]	1.0 ^[30]	2480 ^[35]	0.67 ^[35]	Table 2.2	0.84 ^[30]
Air	0.012 ^[30]	0.024 ^[30]	1.292 ^[30]	1.006 ^[30]	-	-
Glass (Clear)	0.0057 ^[30]	1.0 ^[30]	2480 ^[35]	0.67 ^[35]	Table 2.2	0.84 ^[30]
Air	0.012 ^[30]	0.024 ^[30]	1.292 ^[30]	1.006 ^[30]	-	-
Glass (Clear)	0.0057 ^[30]	1.0 ^[30]	2480 ^[35]	0.67 ^[35]	Table 2.2	0.84 ^[30]
Single-pane (Pre)						
Glass (Clear)	0.0137 ^[30]	0.617 ^[30]	2480 ^[35]	0.67 ^[35]	Table 2.2	0.84 ^[30]
Ground						
Asphalt	0.07 ^[38]	0.75 ^[35]	2110 ^[35]	0.92 ^[35]	0.9-0.7-0.5	0.95 ^[35]
Crushed rock	0.2	0.95 ^[37]	1200 ^a	1.05 ^a	-	-

^a: Assumed

^b: Insulation conductivities are calculated based on their typical thickness.

TABLE 2.2 Angular and diffuse Solar Heat Gain Coefficient (SHGC), absorptance and transmittance of window glass. Properties of single (triple) pane windows which are used in pre (post) -1980 buildings are simulated by WINDOW v7.0.68.0 software [30].

Inc. Angle (degree)	SHGC (Single)	SHGC (Triple)	Abs. (single)	Abs. (Triple - 1st pane)	Abs. (Triple - 2nd pane)	Abs. (Triple - 3rd pane)	Trans. (Single)	Trans. (Triple)
0	0.722	0.222	0.316	0.526	0.022	0.016	0.617	0.157
10	0.716	0.223	0.301	0.531	0.023	0.016	0.616	0.158
20	0.713	0.221	0.305	0.535	0.023	0.016	0.612	0.155
30	0.708	0.217	0.311	0.536	0.023	0.016	0.605	0.152
40	0.698	0.212	0.318	0.532	0.023	0.016	0.593	0.146
50	0.679	0.201	0.326	0.528	0.024	0.016	0.571	0.135
60	0.639	0.177	0.329	0.523	0.024	0.015	0.530	0.112
70	0.550	0.132	0.319	0.494	0.022	0.012	0.444	0.074
80	0.352	0.069	0.269	0.366	0.017	0.006	0.263	0.027
90	0	0	0	0	0	0	0	0
Diffuse	0.646	0.187	0.311	0.511	0.023	0.015	0.542	0.125

2.3 Results and discussion

2.3.1 Annual and daily thermal loads

Fig. 2.2 shows annual thermal loads of post and pre-1980 buildings (representing energy efficient and less energy efficient buildings representative of the building stock) versus ground surface solar reflectance for three different canopy aspect ratios. Table 2.3 shows the annual heating and cooling loads for all scenarios with ground surface albedo of 0.5. As expected, for both types of buildings annual heating and annual cooling loads decrease with increasing canopy height-to-width

ratio (H/W). Also annual thermal loads increase with increasing WWR. On the other hand annual cooling noticeably increases in both types of buildings with increasing ground surface albedo, but annual heating shows little or no sensitivity to ground surface albedo. The next sections will analyze these results in more detail.

TABLE 2.3 Annual heating and annual cooling loads for all cases with ground surface albedo of 0.5

	Simulation Type (Ground albedo = 0.5)	Annual Heating Load (kWh m ⁻²)	Annual Cooling Load (kWh m ⁻²)
Pre-1980 Buildings	H/W = 0.37, WWR = 0.47	40.8	329.8
	1.0, 0.47	35.1	298.6
	1.5, 0.47	30.9	274.8
	1.0, 0.24	24	248.9
	1.0, 0.66	45.1	326
Post-1980 Buildings	H/W = 0.37, WWR = 0.47	17.7	229.7
	1.0, 0.47	16.7	217
	1.5, 0.47	15.9	207.9
	1.0, 0.24	14.6	190.3
	1.0, 0.66	18.7	237.4
	0.37, 0.47, Reflective Window	21.1	219.4

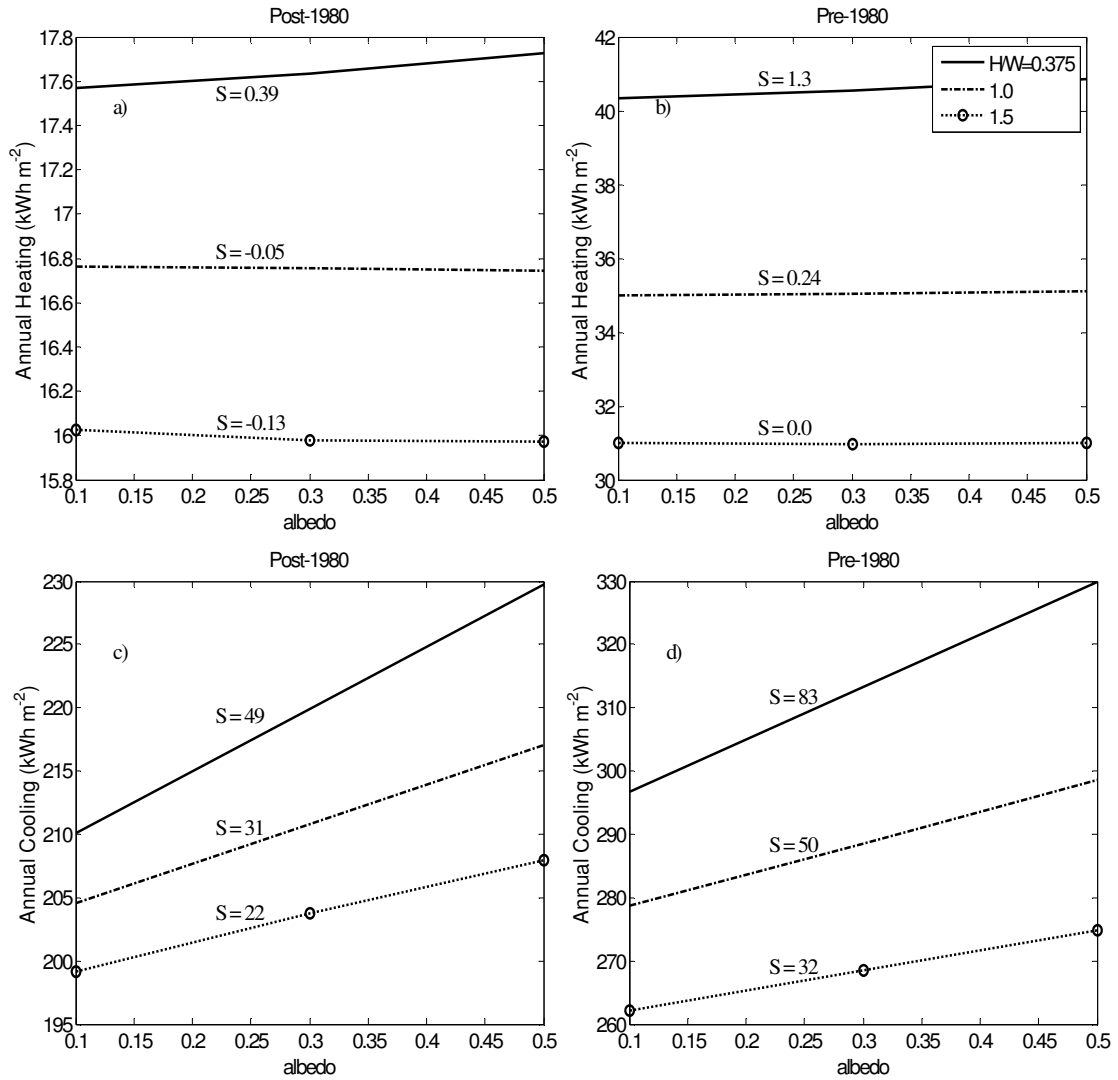


FIG. 2.2 Annual heating and annual cooling loads for post (a and c) and pre (b and d) 1980 buildings in Phoenix, AZ. S is the slope of annual thermal load with respect to ground surface albedo in units of kWh m^{-2} per albedo change from 0 to 1.

a. Canopy floor surface albedo

Fig. 2.2 indicates that for both pre and post-1980 buildings and for all three canopy aspect ratios annual thermal loads change linearly with ground surface albedo, albeit the sensitivity (i.e. the slope in Fig. 2.2) is different. Due to larger conduction (because of poor insulation) and larger transmitted shortwave radiation (due to single-

pane windows) the thermal demand in pre-1980 buildings is more sensitive to canopy floor albedo.

To better understand how the annual (and peak) simulation results relate to the thermal processes, Figs. 2.3 and 2.4 present monthly average diurnal cycle results for the average July day including temperatures of ground surface, canopy air, outside building wall including windows, inside building surfaces with the total transmitted shortwave radiation into the building from all windows and thermal loads. The average wind speed in July is 3.6 m s^{-1} and average daily high and low air temperatures are 41.4°C and 29.9°C , respectively. Since the heating / cooling load change with albedo was linear, only the 0.1 and 0.5 ground surface albedo simulations are shown.

As expected, during the day the temperature of the darker ground surface is significantly higher than the temperature of the brighter surface (differences up to 15.8°C at 14 LST for canopies with $H/W = 0.37$; Figs. 2.3a and 2.4a). This temperature difference affects air temperature in the canopy but this effect is relatively small (0.4°C at 14 LST for canopies with $H/W = 0.37$; Figs. 2.3b and 2.4b). The effects of ground surface albedo on canopy air temperature are larger in canopies with smaller aspect ratios.

Larger ground albedo results in larger shortwave reflection onto the wall and window surfaces and larger transmitted shortwave radiation into the buildings (Figs. 2.3e and 2.4e) causing higher indoor surface temperatures (Figs. 2.3d and 2.4d) and decrease in heating load (winter; not shown) and increase in cooling load (summer;

Figs. 2.3f and 2.4f). Similar processes (at different magnitudes) can be observed for a typical winter day (not shown).

FIG. 2.3 Comparison of monthly averaged a) ground surface, b) canopy air, c) outdoor wall surface, d) indoor building surface temperatures, e) total transmitted shortwave radiation into the building from all windows and f) thermal loads for **pre-1980** buildings for July in Phoenix, AZ. Transmitted shortwave radiation and thermal loads are in Watt per square meter of floor area. Outside building wall temperature is averaged over all four outside walls including windows. Indoor building surface temperature is the average temperature of all surface temperatures inside the building.

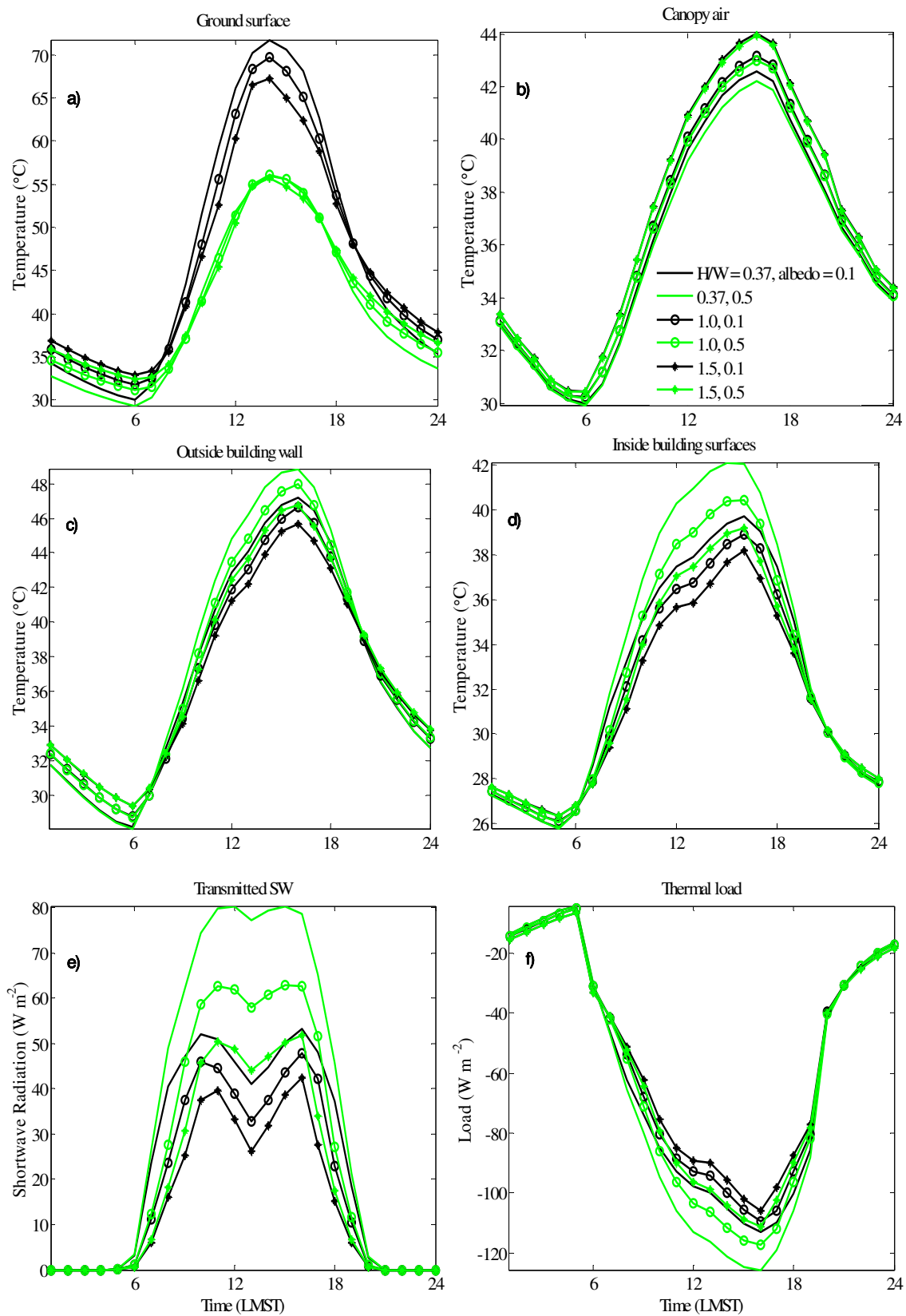
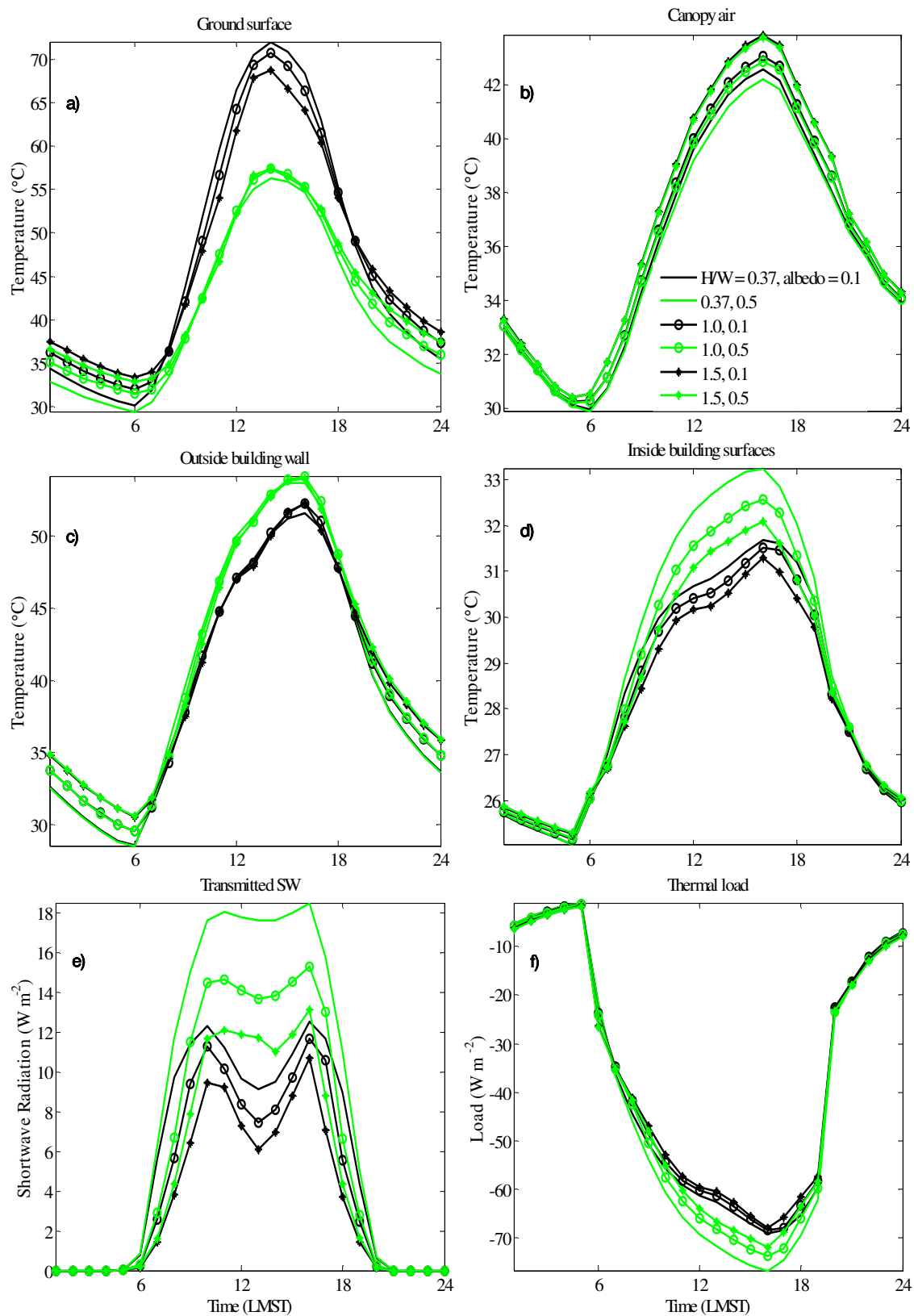


FIG. 2.4 Comparison of monthly averaged a) ground surface, b) canopy air, c) outdoor wall surface, d) indoor building surface temperatures, e) total transmitted shortwave radiation into the building from all windows and f) thermal loads for **post-1980** buildings for July in Phoenix, AZ. Transmitted shortwave radiation and thermal loads are in Watt per square meter of floor area. Outside building wall temperature is averaged over all four outside walls including windows. Indoor building surface temperature is the average temperature of all surface temperatures inside the building.



b. Canopy aspect ratio

The slope of annual thermal loads with respect to ground surface albedo (Fig. 2.2) and the diurnal cycles (Figs. 2.3, 2.4) indicate that (as expected) the albedo effect is stronger for smaller H/W . The thermal conditions and indoor-outdoor heat fluxes converge with increasing H/W since in deep and narrower canopies less shortwave radiation reaches the ground surface making the ground surface albedo less relevant. In addition, due to shadowing during the day the ground, outdoor and indoor building surface temperatures decrease with increasing canopy H/W (Fig. 2.3a, c, d; 2.4a, c, d). The reverse trend is observed at night when the reduction in longwave radiation losses at the outside surfaces leads to increased air and surface temperatures for larger H/W . The reduction of turbulent sensible heat transfer out of the canyon also contributes to increased air temperature in canopies with larger H/W [39, 40].

As a result of less transmitted shortwave radiation into the buildings in deep and narrower canopies less (mostly daytime) cooling is required with increasing H/W (Figs 2.3f, 2.4f) in both types of buildings.

c. Building condition and construction materials

In both pre and post-1980 buildings, heating mostly occurs at night and cooling mostly happens during the day due to solar and internal heat gains. Due to poor insulation (in walls and single pane windows), the indoor air and surface temperatures of pre-1980 building are strongly influenced by the outdoor temperatures. Comparing the annual thermal loads (Fig. 2.2 and Table 2.3) reveals that

pre-1980 buildings require more heating and cooling energy than post-1980 buildings. On the other hand, in post-1980 buildings due to stronger insulation the conductive heat exchange between indoor and outdoor is smaller. Consequently at night the inside environment does not benefit much from the higher outdoor temperature in larger H/W to reduce heating loads and as a result the maximum difference in annual heating loads for small and large H/W is small (less than 1.8 kWh m^{-2}) for post-1980 buildings (Fig. 2.2a).

Figs. 2.3c and 2.4c (average outdoor surface temperature of walls and windows) show that for a typical summer day the outside building surface temperature in a post-1980 building is generally higher than in a pre-1980 building. The lower outdoor building surface temperature in pre-1980 buildings can be explained by larger heat conduction into the building through walls and single-pane windows due to smaller thermal resistances compared to the well insulated walls and triple-pane windows in post-1980 buildings.

Indoor building surface temperature is a result of heat transferred into the building through the building envelope, transmitted shortwave radiation, radiation and convection from internal loads and indirect effects of infiltration and ventilation. With the same amount of internal loads and infiltration / ventilation in both types of buildings, the larger transmitted shortwave radiation through single pane windows and larger heat transfer through the building walls and roof in pre-1980 buildings cause indoor surfaces to experience higher temperatures.

d. Window type and size effects

Single versus triple-pane window

As shown in Figs. 2.3e and 4e, there is a large difference between transmitted shortwave radiation through single-pane windows in pre-1980 buildings and triple-pane windows in post-1980 buildings (a factor of 5). Triple and single-pane windows have very different thermal and radiative properties (Tables 2.1, 2.2). A triple-pane window with two gaps filled with air provides stronger insulation reducing the conductive heat transfer. In addition, triple-pane windows have larger absorptance and smaller SHGC and transmittance. As a result conductive heat gain and transmitted shortwave radiation into the building noticeably decrease compared to the buildings with single-pane windows reducing cooling demand. Fig. 2.5 displays the comparison of transmitted shortwave radiation (in W m^{-2} of floor area) through single and triple-pane windows and total thermal loads of pre and post-1980 buildings for canopies with $H/W = 1$ and ground surface albedo of 0.5 for a typical summer day. The ratio of the total amount of transmitted shortwave radiation through single-pane windows in pre-1980 buildings to the total cooling load can be up to 68% at 10 LST compared to 25% of triple-pane windows in post-1980 building at the same time. The daily integrated value of transmitted shortwave radiation and the cooling load for a typical summer day in pre-1980 building is 606 and 1406.1 Wh m^{-2} of floor area and in post-1980 buildings is 144.3 and 907.5 Wh m^{-2} of floor area, respectively. This indicates the importance of the window properties and the effects of outdoor conditions on the available shortwave radiation incident on a building on the building thermal loads.

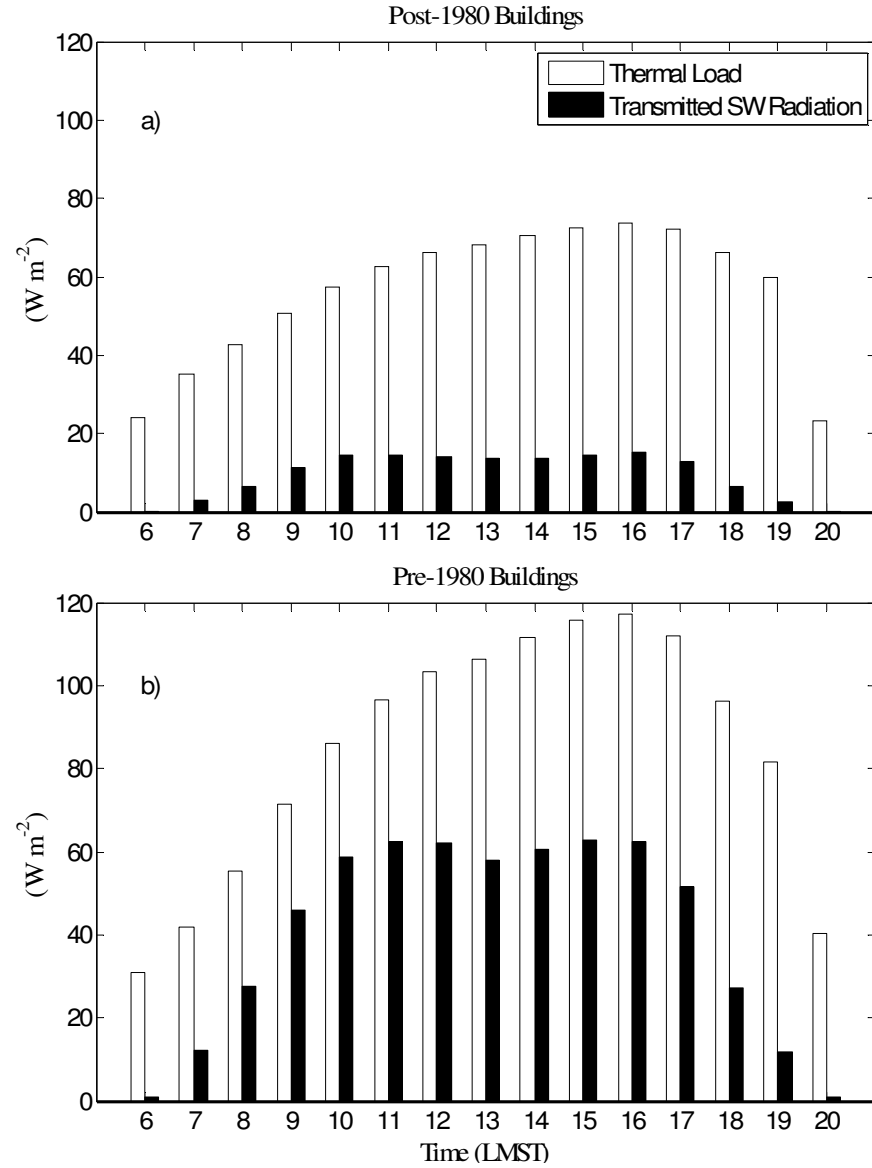


FIG. 2.5 Comparison of the transmitted shortwave radiation through windows and total thermal load of a) post and b) pre-1980 buildings in W m^{-2} of floor area for canopies with $H/W = 1$ and ground surface albedo of 0.5 for a typical summer day (monthly averaged diurnal cycle over July) in Phoenix, AZ.

Reflective mirrored windows

Fig. 2.6 compares the effects of typical reflective windows on transmitted shortwave radiation into the building and thermal load for average summer and winter

days in Phoenix, AZ. As expected a clear window transmits more shortwave radiation into the building than a reflective window (Fig. 2.6a and c). The difference in thermal loads results from the differences in the overall window conductivity and transmittance (that are lumped in the SHGC). While the transmittance and SHGC of the double-pane reflective windows is even smaller than the triple-pane windows in post-1980 buildings (Tables 2.2 and 2.A2), the conductivity of double pane windows is larger. Consequently, during the summer (Fig. 2.6b) even though there is less transmitted shortwave radiation into the building through reflective double-pane windows there is a small difference between cooling loads; during 13-17 LST the cooling load in the building with the reflective window is even larger than the building with triple-pane clear window. The reason is that heat conduction (large temperature difference between indoors and outdoors) then dominates over light transmission. On the other hand when indoor-outdoor temperature gradients are reversed (winter), besides less transmitted shortwave radiation into the building, buildings with double-pane reflective windows also benefit from outdoor cool air in winter and so daytime cooling load in these buildings is less than for triple-pane clear windows (total of 0.05 kWh m⁻² in a typical winter day). During winter nights, however, the difference in heating loads in Fig. 2.6d is only related to the difference in window conductivity. The annual cooling load in buildings with double-pane reflective windows is 4.5% (10.3 kWh m⁻²) less than in buildings with triple-pane clear windows but the annual heating load is 19.2% (3.4 kWh m⁻²) larger (Table 2.3). Another reason for the relatively small relative differences in cooling load is that there is a negative feedback in that the energy reflected from reflective windows increase the amount of available radiation

reaching the surrounding building walls and ground surfaces and affects the thermal load in adjacent buildings.

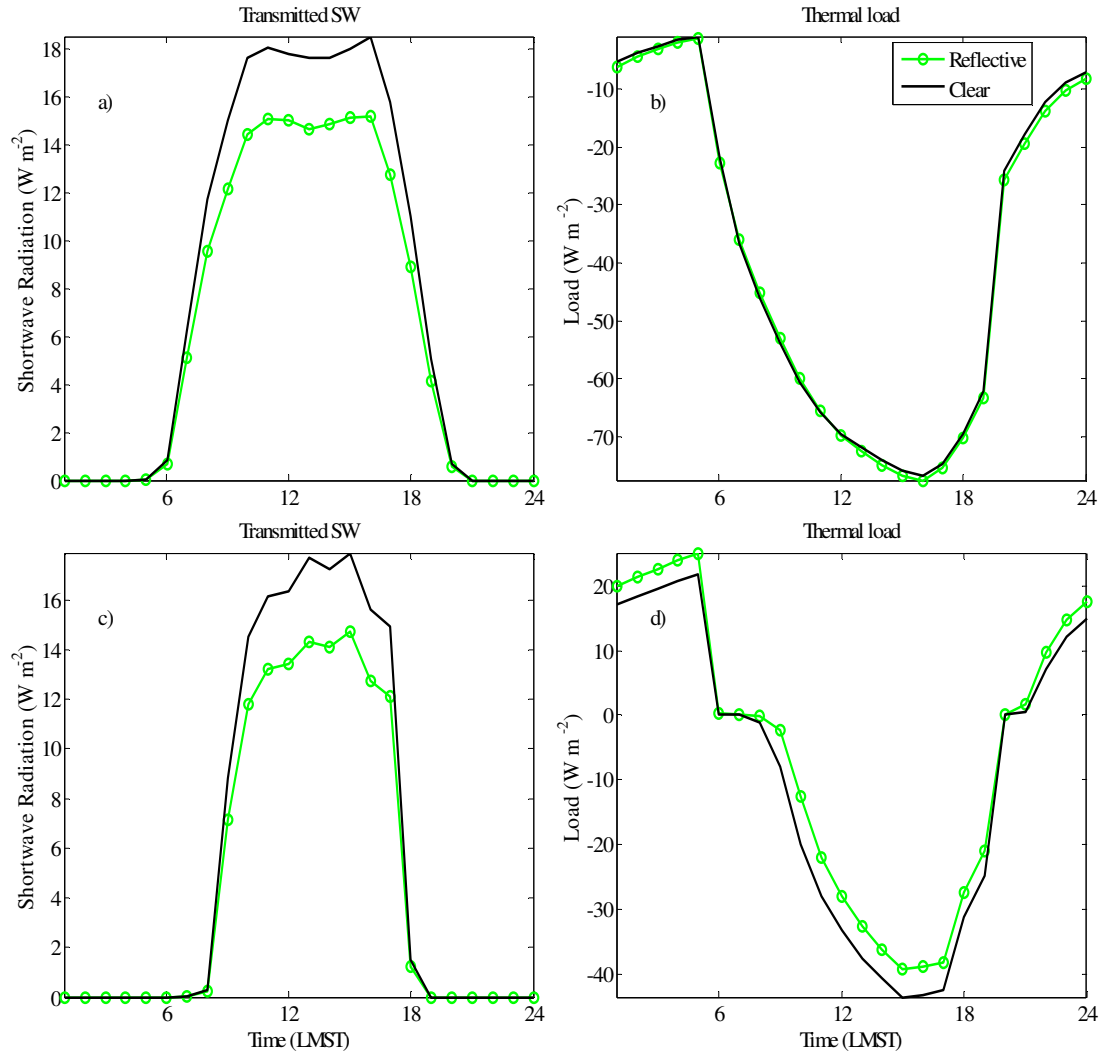


FIG. 2.6 Comparison of monthly averaged total transmitted shortwave radiation into the building from all windows (a, c) and thermal loads (b, d) in post-1980 buildings with double-pane reflective windows and triple-pane clear windows in July (a, b) and January (c, d) in a canopy with $H/W = 0.37$ and ground surface albedo of 0.5. Negative (positive) loads represent cooling (heating). Transmitted shortwave radiation and thermal loads are in Watt per square meter of floor area.

Window surface area

Besides window type, window size is the other important factor in controlling indoor temperatures and thermal demand in buildings. The main impact of larger windows in our study is that they transmit more shortwave radiation into the building resulting in larger surface and air temperatures. Larger windows also cause more conductive exchange between indoors and outdoors, due to their larger thermal conductivity compared to walls. Fig. 2.7 shows transmitted shortwave radiation through windows and thermal loads in buildings with three different WWRs for a typical summer day. Increasing WWR from 0.24 to 0.66 (for post-1980 buildings in canopies with $H/W = 1$ and ground surface albedo of 0.5) results in a 20% increase in total daily cooling demand for a typical summer day and 25% (28%) increase in total annual cooling (heating) demand. The same trends for WWR exist for pre-1980 buildings and for winter times. While increased shortwave transmission for large WWR acts to reduce heating loads in the winter, most heating happens at night and then the larger conductivity of windows versus walls leads to an overall increase in heating loads (not shown).

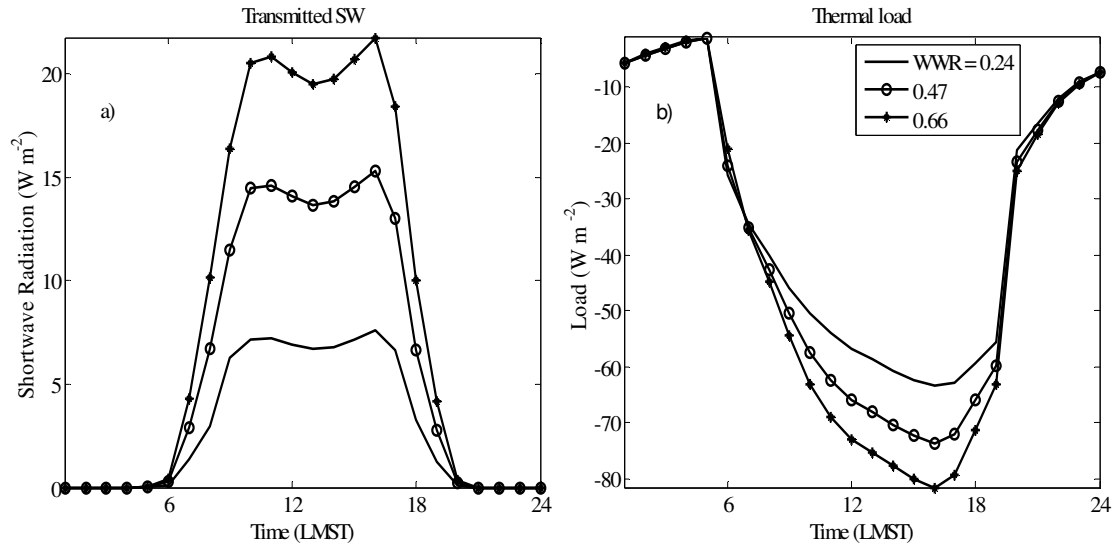


FIG. 2.7 Comparison of monthly averaged a) total transmitted shortwave radiation into the building from all windows and b) thermal loads for post-1980 buildings in canopies with $H/W = 1$ and ground surface albedo of 0.5 for July in Phoenix, AZ for three different window-to-wall ratios (WWR). Transmitted shortwave radiation and thermal loads are in Watt per square meter of floor area.

2.3.2 Peak thermal loads

Peak thermal loads are important because they determine sizing of the HVAC system. Peak loads also typically occur during clear days with large insolation amplifying the effects of reflective pavements. Fig. 2.8 shows the change in annual peak thermal loads of post and pre-1980 buildings with respect to change in ground surface albedo for three different canopy aspect ratios. The trend of peak thermal loads is similar to the trend of annual thermal loads and can be explained similarly. Generally, buildings in denser neighborhoods (larger H/W) require smaller HVAC systems. Not surprisingly, Fig. 2.8 also shows that peak heating loads in both types of buildings are independent of canopy floor albedo since they occur at night. With increasing ground surface albedo from 0.1 to 0.5 peak cooling demand increases by 5.3 – 10.6% ($6 - 13 \text{ W m}^{-2}$) in pre-1980 buildings and 7.1 – 10.9% ($5.2 - 8 \text{ W m}^{-2}$) in

post-1980 buildings. The relative changes are similar in magnitude to the annual cooling load changes with albedo. HVAC systems have to be larger in pre-1980 buildings since all peak cooling load components are larger than in post-1980 buildings.

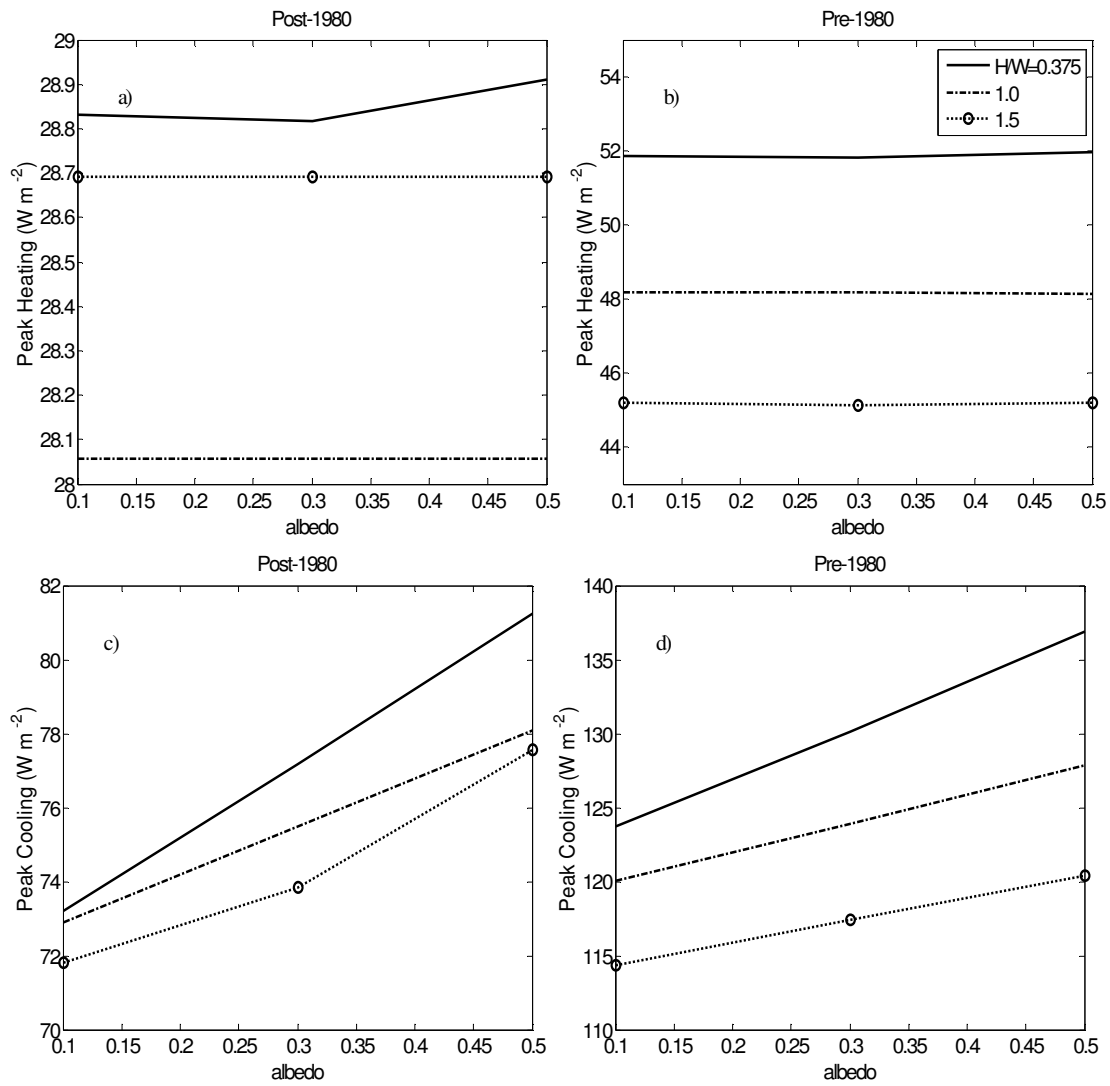


FIG. 2.8 Peak heating and peak cooling loads over a year for post (a and c) and pre (b and d) 1980 buildings in Phoenix, AZ.

2.3.3 Discussion of Modeling Assumptions

Effects on building energy use in the immediate vicinity of high albedo pavements through radiative and conductive increases in cooling load (Figs 2.3c-e, 2.4c-e) by far dominate indirect effects through reduction in canopy air temperature (Figs 2.3b, 2.4b). Canopy air temperature is more sensitive to the canopy aspect ratio than ground surface albedo. However, our simulations assume perfect advection, i.e. the heat flux from inside the canopy to the atmospheric surface layer is removed from the simulation domain. Consequently, feedback effects acting on air temperature are blunted compared to simulations with one dimensional atmospheric models including the boundary layer and recirculating flow [e.g. 41]. Accounting for the non-local effect of a larger reflective pavement program in an urban area would reduce (but not reverse) the increase in energy use with increasing albedo. Similarly, since there is no coupling between the canopy and atmospheric surface layer, in TUF-IOBES roof thermal behavior is independent of canopy aspect ratio and ground surface albedo.

While we also ignore the high pavement albedo effects on the earth's radiative balance and reduction in global warming, this feedback on building energy use is weak.

The quantity of simulated heating loads is unrealistic for commercial buildings since HVAC systems do not operate at nights. Furthermore, considering intermediate floors and associated thermal mass in these simulations would reduce the daytime and increase the nighttime cooling loads; however sensitivity studies (not shown) demonstrated minimal changes in annual and peak cooling loads. During peak days

the thermal mass is already warm due to heat storage on previous days limiting its thermal impacts on indoor air.

Since canopy aspect ratio and ground surface albedo affect natural lighting in buildings, they also affect building energy use for lighting [42]. For example, in denser neighborhoods or over darker ground surfaces more artificial lighting and consequently more energy should be required in buildings. Besides the parameters modeled in this study (shadowing of neighboring buildings for large H/W and multi-pane windows with different size and radiative properties, Tables 2.2 and 2.A2), transmitted solar radiation depends on shading devices (curtains, blinds or outside sunshades [43]) and window locations. Moreover, lighting in most office buildings is not controlled dynamically based on photo-cells and human operator action is unlikely. Also for visual comfort of pedestrians and vehicle operators a significant fraction of the albedo gain of very reflective pavements would be achieved in the near-infrared spectrum. Increase in near-infrared irradiation indoors would not cause any change in artificial lighting needs. Properly accounting for energy implications of indoor light conditions would require modeling spectral irradiance, glare and shading devices, and the human intervention. Since these interactions are complex to model and the impacts are likely small, we neglect the feedback effect of improved daylighting for more reflective ground surfaces.

2.4 Conclusion

The Temperature of Urban Facets Indoor-Outdoor Building Energy Simulator (TUF-IOBES) is applied to investigate the effects of reflective pavements on energy use in nonresidential office buildings in Phoenix, AZ. Sensitivity of the results to canopy aspect ratio, building age (as reflected in insulation), window surface area, and windows with different radiative properties are also investigated. The results of this study show that the annual thermal loads decrease with increasing canopy height-to-width ratio and increase with increasing window-to-wall ratio. On the other hand annual cooling increases with increasing ground surface albedo but annual heating shows no sensitivity to ground surface albedo. The effect of double-pane reflective windows compared to triple-pane clear windows on building energy use is to decrease the annual cooling load and increase the annual heating load.

As also highlighted by Bouyer et al. [3] and Strømman-Andersen and Sattrup [42], our results indicate the importance of the direct evaluation of the microclimate influence (e.g. effects of canopy floor reflectance and urban canopy height to width ratio) on building energy use. The diversity of urban landscapes and designs means that an idealized study such as ours cannot provide optimum solutions for size and type of the building elements or shape of urban canopies. Only local simulations for specific neighborhoods and urban climates can elucidate the exact effect of reflective pavement implementation. For example, energy use in older buildings in New York City, even those dating to the early 1900s, is less than in most new structures because of fewer windows and thicker walls used in the older structures [44].

Strømman-Andersen and Sattrup [42] investigated the effects of the solar radiation distribution and daylight on total energy use (heating, cooling, and artificial lighting) in canopies with different aspect ratios for the urban morphology of Copenhagen. In their study artificial lighting is the dominant contributor to energy use. Energy use for artificial lighting increases more than six times at $H/W = 3$ compared to an unobstructed building. Consistent with our results, Strømman-Andersen and Sattrup [42] show that cooling demand decreases with increasing canopy aspect ratio due to overshadowing.

This study shows that the interaction of urban materials like reflective pavements and mirrored windows with surrounding buildings must be considered in the context of an urban area. The increase in energy use for buildings near reflective pavements shown in this paper for a typical scenario indicates that reflective pavements should be considered with caution. On the other hand, application of cool pavement to roads without nearby air-conditioned buildings reduces global radiative forcing counteracting global warming [45] and reduces air temperatures and energy use in urban areas downwind. We recommend that policymakers carefully weigh the benefits and disadvantage of reflective pavements to ensure their optimal application.

Acknowledgments

We thank Dr. Charlie Curcija (Lawrence Berkeley National Laboratory) for suggesting WINDOW v7.0.68.0 software and typical glazing ratios in commercial buildings, funding from a National Science Foundation CAREER award, and anonymous reviewers helped in improving the manuscript.

The text and data in chapter 2, in full, is a reprint of the material as it appears in “Effect of reflective pavements on building energy use”, Yaghoobian, Neda; Kleissl, Jan, *Urban Climate*, 2, 25-42 (2012). The dissertation author is the primary investigator and author of this article.

Appendix

TABLE 2.A1 Double-pane reflective window thickness and thermal properties by layer. Properties of the reflective glass are for a product named ‘Solar Silver 20% on 3mm Clear’ manufactured by ‘Johnson laminating & Coating, Inc.’ [30]. Properties of the clear glass are for a product named ‘Clear-6 / .090 PVB / Clear-6’ manufactured by ‘Cardinal Glass Industries’ [30].

Double-pane reflective window	Thickness (m)	Conductivity (W m ⁻¹ K ⁻¹)	Density (kg m ⁻³)	Specific heat (kJ kg ⁻¹ K ⁻¹)	IR Emis. [-]
Glass (Reflective)	0.0032 ^[30]	0.969 ^[30]	2480 ^[35]	0.67 ^[35]	0.84 ^[30]
Air	0.012 ^[30]	0.024 ^[30]	1.292 ^[30]	1.006 ^[30]	-
Glass (Clear)	0.013 ^[30]	0.617 ^[30]	2480 ^[35]	0.67 ^[35]	0.84 ^[30]

TABLE 2.A2 Angular and diffuse Solar Heat Gain Coefficient (SHGC), absorptance and transmittance of double-pane reflective window. Properties of the window are simulated by WINDOW v7 software [30].

Incident Angle (degree)	SHGC	Absorptance (Reflective pane)	Absorptance (Clear pane)	Transmittance
0	0.197	0.315	0.044	0.123
10	0.198	0.318	0.045	0.123
20	0.196	0.321	0.045	0.121
30	0.194	0.322	0.045	0.118
40	0.190	0.320	0.045	0.114
50	0.182	0.317	0.045	0.108
60	0.167	0.314	0.043	0.094
70	0.136	0.297	0.037	0.070
80	0.080	0.222	0.025	0.033
90	0	0	0	0
Diffuse	0.172	0.307	0.042	0.101

References

- [1] C.W. Mackey, X. Lee, R.B. Smith, Remotely sensing the cooling effects of city scale efforts to reduce urban heat island, *Build Environ.* 49 (2012) 348-358.
- [2] H. Akbari, S. Konopacki, Calculating energy-saving potentials of heat-island reduction strategies, *Energ. Policy.* 33 (2005) 721-756.
- [3] J. Bouyer, C. Inard, M. Musy, Microclimatic coupling as a solution to improve building energy simulation in an urban context, *Energ. Buildings.* 43 (2011) 1549-1559.
- [4] E. Krüger, D. Pearlmutter, F. Rasia, Evaluating the impact of canyon geometry and orientation on cooling loads in a high-mass building in a hot dry environment. *J. Appl. Energ.* 87 (2010) 2068-2078.
- [5] R. Berg, W. Quinn, Use of light colored surface to reduce seasonal thaw penetration beneath embankments on permafrost. In: *Proceedings of the Second International Symposium on Cold Regions Engineering.* University of Alaska, 1978, pp. 86-99.
- [6] H. Taha, D.J. Sailor, H. Akbari, High-albedo materials for reducing building cooling energy use, Rep. LBL-3172L Lawrence Berkeley Laboratory, Berkeley, CA, 1992.
- [7] A.H. Rosenfeld, H. Akbari, S. Bretz, B.L. Fishman, D.M. Kurn, D.J. Sailor, H. Taha, Mitigation of urban heat islands: materials, utility programs, updates, *Energ Buildings.* 22 (1995) 255-265.
- [8] D.J. Sailor, Simulated urban climate response to modifications in surface albedo and vegetative cover, *J. Appl. Meteorol.* 34 (1995) 1694-1704.
- [9] D.S. Parker, S.F. Barkaszi, Roof solar reflectance and cooling energy use: field research results from Florida, *Energ. Buildings.* 25 (1997) 105-115.
- [10] H. Akbari, S. Bretz, D.M. Kurn, J. Hanford, Peak power and cooling energy savings of high-albedo roofs, *Energ. Buildings.* 25 (1997) 117-126.
- [11] S. Bretz, H. Akbari, A. Rosenfeld, Practical issues for using solar-reflective materials to mitigate urban heat islands, *Atmos. Environ.* 32 (1998) 95-101.
- [12] H. Akbari, L. Rainer, Measured Energy Savings from the Application of Reflective Roofs in 3 AT&T Regeneration Buildings. Lawrence Berkeley National Laboratory. Paper LBNL-47075, 2000.

- [13] H. Akbari, M. Pomerantz, H. Taha, Cool surfaces and shade trees to reduce energy use and improve air quality in urban areas, *Sol. Energy*. 70 (2001) 295–310.
- [14] L. Doulos, M. Santamouris, I. Livada, Passive cooling of outdoor urban spaces, The role of materials, *Sol. Energy*. 77 (2004) 231–249.
- [15] L. Shashua-Bar, D. Pearlmutter, E. Erell, The cooling efficiency of urban landscape strategies in a hot dry climate, *Landscape Urban Plan*. 92 (2009) 179-186.
- [16] A. Scherba, D.J. Sailor, T.N. Rosenstiel, C.C. Wamser, Modeling impact of roof reflectivity, integrated photovoltaic panels and green roof systems on sensible heat flux into the urban environment, *Build. Environ*. 46 (2011) 2542-2551.
- [17] Cardin, Energy-Efficient Cool Roof Jobs Act. <http://www.govtrack.us/congress/billtext.xpd?bill=s112-1575>. 2011. Accessed 13 Dec 2011.
- [18] Connolly, Heat Island and Smog Reduction Act of 2011. (Introduced in House - IH) <http://thomas.loc.gov/cgi-bin/thomas>. 2011. Accessed 13 Dec 2011.
- [19] Skinner, Cool pavements. http://www.leginfo.ca.gov/pub/11-12/bill/asm/ab_0251-0300/ab_296_cfa_20110623_170416_sen_comm.html. 2011. Accessed 16 Dec 2011.
- [20] N. Yaghoobian, J. Kleissl, E.S. Krayenhoff, Modeling the thermal effects of artificial turf on the urban environment, *J. Appl. Meteorol. Clim*. 49 (2010) 332–345.
- [21] D. Pearlmutter, P. Berliner, E. Shaviv, Physical modeling of pedestrian energy exchange within the urban canopy, *Build. Environ*. 41 (2006) 783-795.
- [22] E. Erell, Effect of high-albedo materials on pedestrian thermal comfort in urban canyons, International Conference on Urban Climate, Dublin, Ireland, August 2012.
- [23] D.J. Sailor, Building Energy Use Implications of Ground-Level Albedo Modification, International Conference on Urban Climate, Dublin, Ireland, August 2012.
- [24] N. Yaghoobian, J. Kleissl, An Indoor-Outdoor Building Energy Simulator to Study Urban Modification Effects on Building Energy Use - Model Description and Validation. *Energy Buildings* (2012), <http://dx.doi.org/10.1016/j.enbuild.2012.07.019>
- [25] Lawrence Berkeley Laboratory (LBL), DOE2.1E-053 source code, 1994.
- [26] C.O. Pedersen, R.J. Liesen, R.K. Strand, D.E. Fisher, L. Dong, P.G. Ellis, A toolkit for building load calculations; Exterior heat balance (CD-ROM), American

Society of Heating, Refrigerating and Air Conditioning Engineers (ASHRAE), Building Systems Laboratory, 2001.

[27] W. Chow, D. Brennan, A. Brazel, Urban Heat Island Research in Phoenix, Arizona: Theoretical Contributions and Policy Applications. *Bull. Amer. Meteor. Soc.*, 93 (2012), 517–530.

[28] American Society of Heating, Refrigerating and Air-Conditioning Engineers, Inc. ANSI/ASHRAE/IESNA Standard 90.1-2004, Energy Standard for Buildings Except Low-Rise Residential Buildings I-P Edition.

[29] K. Haglund, Window Selection Methodologies and Optimization in High-performance Commercial Buildings. BEST2 Conference, Portland, Oregon, April 2010.

[30] WINDOW v7.0.68.0, <http://windows.lbl.gov/software>

[31] G. Chamberlin, D. Schwenk, Standard HVAC Control Systems Commissioning and Quality Verification User Guide, US Army Construction Engineering Research Laboratories Champaign, IL, 1994.

[32] American Society of Heating, Refrigerating and Air-Conditioning Engineers, Inc. ANSI/ASHRAE Standard 62.1-2007, Ventilation for Acceptable Indoor Air Quality.

[33] American Concrete Pavement Association, Albedo: a measure of pavement surface reflectance. <http://www.pavement.com/Downloads/RT/RT3.05.pdf>. 2002. Accessed 15 Dec 2011.

[34] F. Incropera, D. Dewitt, Fundamental of heat and mass transfer. John Wiley & Sons, New York, 2002.

[35] T. R. Oke, Boundary Layer Climates. Methuen, London, 1987.

[36] The Engineering Toolbox (http://www.engineeringtoolbox.com/air-properties-d_156.html)

[37] L. P. Crevier, Y. Delage, METERo: a new model for road-condition forecasting in Canada. *J. Appl. Meteorol.*, 40 (2001), 2026–2037.

[38] C. Jansson, E. Almkvist, P. Jansson, Heat balance of an asphalt surface: observation and physically-based simulations. *Meteor. Appl.*, 13 (2006) 203–221.

[39] T.R. Oke, G.T. Johnson, D.G. Steyn, I.D. Watson, Simulation of surface urban heat islands under “ideal” conditions at night Part 2: diagnosis of causation, *Bound-Lay Meteorol.* 56 (1991) 339–358.

- [40] T.R. Oke, Street design and urban canopy layer climate, *Energ. Buildings*. 11 (1988) 103–113.
- [41] E. S. Krayenhoff, J.A. Voogt, Impacts of Urban Albedo Increase on Local Air Temperature at Daily–Annual Time Scales: Model Results and Synthesis of Previous Work, *J. Appl. Meteorol. Clim.* 49 (2010) 1634–1648.
- [42] J. Strømman-Andersen, P.A. Sattrup, The urban canyon and building energy use: Urban density versus daylight and passive solar gains, *Energ. Buildings*. 43 (2011) 2011–2020.
- [43] H. Akbari, Shade trees reduce building energy use and CO₂ emissions from power plants, *Environ. Pollut.* 116 (2002) S119–S126.
- [44] M. Navarro, Wide Differences Found in Buildings’ Power Use, *The New York Times*, August 2012. (<http://www.nytimes.com/2012/08/03/nyregion/wide-differences-found-in-large-buildings-power-use.html?scp=1&sq=building+energy+use&st=nyt>)
- [45] H. Akbari, S. Menon, A. Rosenfeld, Global cooling: increasing world-wide urban albedos to offset CO₂. *Climate Change*. 94 (2009) 275–286.

Chapter 3

Modeling the Thermal Effects of Artificial Turf on the Urban Environment

Full reprint from *Journal of Applied Meteorology and Climatology*, 49, 332–345, 2010

© American Meteorological Society (Used with permission)

The effects of artificial turf (AT) on the urban canopy layer energy balance, air and surface temperatures, and building cooling loads are compared to those of other common ground surface materials (asphalt, concrete and grass) through heat transfer modeling of radiation, convection, and conduction. We apply the TUF3D (Temperatures of Urban Facets in 3-D) model - modified to account for latent heat fluxes - to a clear summer day at a latitude of 33° over a typical coastal suburban area in Southern California. The low albedo of artificial turf relative to the other materials under investigation results in a reduction in shortwave radiation incident on nearby building walls and an approximately equal increase in longwave radiation. Consequently, building walls remain at the same relatively cool temperature as those that are adjacent to irrigated grass surfaces. Using a simple offline convection model, replacing grass ground cover with artificial turf was found to add $2.3 \text{ kWh m}^{-2}\text{day}^{-1}$ of heat to the atmosphere which could result in urban air temperature increases of up to 4° C.

While the increased urban air temperatures with AT can cause an increase in building peak cooling loads of 60% through conduction and infiltration compared to a building near grass, in this temperate climate the absolute values of these loads are small compared to the reduction in radiative heat flux through windows. Consequently, overall building cooling loads near AT are reduced by 17%. In addition, the irrigation water conservation with AT cause an embodied energy savings of $10 \text{ Wh m}^{-2}\text{day}^{-1}$. Locally, this study points to a win-win situation for AT use for urban landscaping as it results in water and energy conservation.

3.1 Introduction

The thermal environment of a city has a multi-faceted effect on the health of its dwellers and ecological and economic consequences at several scales. Thermal comfort, heat wave mortality, ozone formation, and building energy consumption and resulting CO₂ emissions are all impacted to varying degrees by the canopy layer thermal environment and its distinct character relative to rural areas, a difference that is often loosely referred to as the urban heat island (UHI). In many cities around the world the effect of urbanization on local climate, especially on canopy layer air and surface temperatures, is significant [1-4]. Furthermore, the modified surface energy balance in urban areas significantly modifies micro- and meso-scale flow fields [5].

The genesis of a city's thermal environment is frequently complex in nature and depends on numerous factors including latitude, ambient meteorology, urban canopy geometry and material thermal properties, the amount and distribution of vegetation and anthropogenic activity. All of the above factors except meteorology are significantly under our control, and in the present study we investigate the thermal effects of altering canopy floor materials. This is motivated by the limited availability of irrigation water to cool cities in arid climates.

Artificial turf (AT) has become increasingly popular as an irrigation-free and maintenance-free urban surface for athletic fields, parks, golf courses, and residential and commercial properties. While it is indisputable that AT conserves irrigation water, the thermal impact on the urban environment has not been quantified. Kruger and Pearlmutter [6] showed that the cooling effect of open water evaporation on urban air

temperature resulted in a 20-80% reduction in building energy use in an arid area. However, these results cannot be generalized to grass surfaces (which are the major source of water vapor in urban areas through evapotranspiration) since grass has a larger solar reflectance (albedo) than most open water sources. The surface temperature of grass is usually close to the air temperature due to evaporative cooling. Anecdotal evidence suggests that the lack of evaporation allows AT surface temperatures to exceed that of regular grass by as much as 20° C [7]. In this paper we apply a 3-D heat transfer model of the urban canopy to study the effects of AT on the energy balance of nearby buildings and the temperature of urban areas.

A description of the model is given in Section 3.2, followed by results of the simulation in Section 3.3. The sensitivity analysis in Section 3.3.5 will be followed by a discussion in section 3.4.

3.2 Methods

3.2.1 Modeling radiation, convection, and conduction with TUF3D

TUF3D (Temperatures of Urban Facets in 3-D) is a micro-scale three-dimensional (3-D) urban energy balance model designed to predict urban surface temperatures for a variety of surface geometries and properties, weather conditions, and solar angles [8]. The surface is composed of plane-parallel facets: roofs, walls, and “streets”. These facets are further sub-divided into identical square patches, each of which has its own energy balance and surface temperature, resulting in a 3-D raster model geometry (Fig. 3.1). TUF3D simulates the energy balance over such simple,

non-vegetated, dry 3-D urban geometries on time scales of hours to days, resulting in surface temperature distributions down to the sub-facet scale across walls, streets, and roofs. Its performance has been evaluated with several independent data sets [8, 9]. A version of TUF3D optimized for geometries composed of repeating morphological units is used in this work.

A detailed description of TUF3D can be found in KV07 and only the main components are discussed here. TUF3D is structured into radiation, conduction and convection sub-models to determine sensible (Q_h), conduction (Q_g), and net radiative (R_{net}) fluxes (Fig. 3.2). The radiation sub-model uses the radiosity approach [10] and accounts for multiple reflections of direct solar radiation and shading. All radiative reflection and longwave emission is assumed perfectly diffuse, which enables radiative exchanges to be tracked with the use of view (or shape) factors.

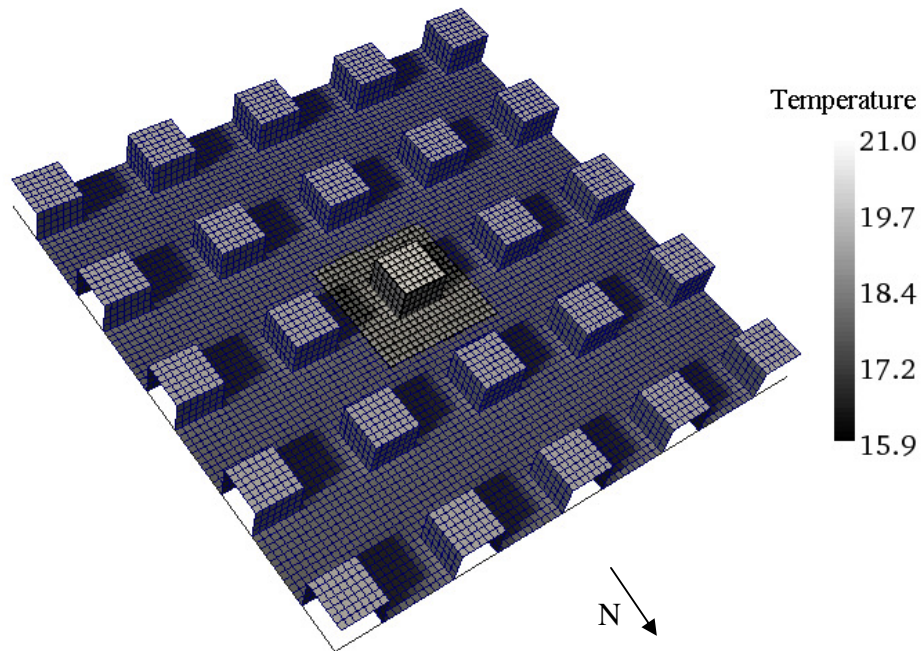


FIG. 3.1 TUF3D model simulation domain with buildings and ground showing surface temperature at 0700 LST. The length of each patch is equal to 3.75 m. The central urban unit is in lighter shades.

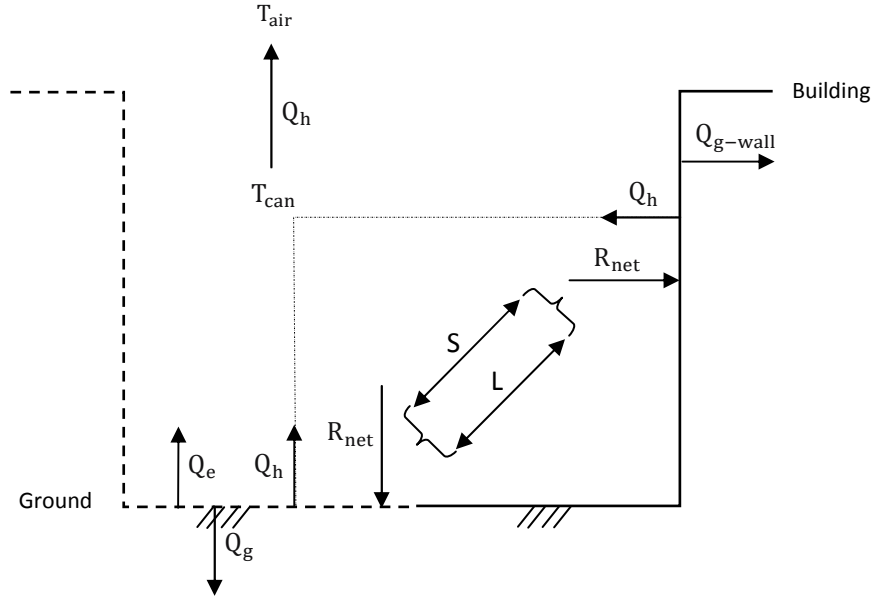


FIG. 3.2 Schematic of the energy balance components between building walls and ground surface in the urban canopy. (T_{air} : above canopy air temperature at twice the building height, T_{can} : canopy air temperature, R_{net} : net radiation, Q_h : sensible heat flux, Q_g : ground heat flux, Q_{g-wall} : building or wall heat flux, Q_e : latent heat flux, S : short wave radiation, L : long wave radiation). Note that in the model all calculations are conducted in three dimensions.

In the conduction sub-model of TUF3D a version of the one dimensional (1-D) heat conduction equation that permits variable layer thickness and thermal conductivity is solved by finite differences for each patch [8].

Convection in TUF3D is modeled by relating patch heat transfer coefficients to the momentum forcing and the building morphology. Sensible heat flux from a patch i of any height follows the typical formulation:

$$H_i = h_i [T_{sfc,i} - T_{can}(z_i)], \quad (3.1)$$

where h_i for *horizontal* patches is calculated using the stability coefficients of Mascart et al. [11] and an effective wind speed. z_i is the height of the patch centre plus a patch forcing height based on internal boundary layer arguments [12], and T refers to temperature. For *vertical* patches h_i in Eq. 3.1 is calculated based on a flat plate forced

convection relationship using wind speed and temperature at the wall patch height, z_i [8]. [In our simulations h_i averages approximately $21 \text{ W m}^{-2}\text{K}^{-1}$ for the roof, $16 \text{ W m}^{-2}\text{K}^{-1}$ for the walls, and for the ground surfaces varies from $9 \text{ W m}^{-2}\text{K}^{-1}$ (concrete, asphalt) over $14 \text{ W m}^{-2}\text{K}^{-1}$ (grass) to $17 \text{ W m}^{-2}\text{K}^{-1}$ (AT).]

In the convection model the 1-D wind speed profile is obtained by applying the logarithmic law above the canopy and an exponential profile within the canopy [8].

Advective horizontal exchanges are neglected in TUF3D due to the well-mixed nature of the canopy layer air in modeled domain which is assumed to be embedded in a large area of similar land cover (here: a large suburban neighborhood).

The canopy air temperature, T_{can} , is calculated by means of an explicit energy budget of the volume of air inside the canopy (between buildings),

$$T_{can}^{m+1} = T_{can}^m + \frac{\Delta t (H_{can}^{m+1} - H_{top}^{m+1})}{c_{air}^{m+1}}, \quad (3.2)$$

where c_{air} [$\text{J m}^{-2}\text{K}^{-1}$] is the average heat capacity of air per unit plan area below the building height, H_{can} is the sum of the convective fluxes from all patches below the building height divided by the canopy-air-plan area ratio, H_{top} is the convective flux density of sensible heat across the canopy top (not including the roof), and m is the time index [8].

3.2.2 Modification to TUF3D

Our main focus is to compare the thermal effect of AT to grass (the surface that it would usually substitute) but we also present results for concrete and asphalt. Unlike AT, concrete and asphalt, grass surfaces evaporate and transpire water thereby

cooling the surface and air. Consequently, TUF3D needs to be modified to account for the latent heat flux in the energy balance equation.

A realistic approach would involve a complex implementation of thermodynamic processes and fluid mechanics of water movement and phase transfer in the soil as well as aerodynamic, biologic, and energy balance principles to estimate both evaporation and transpiration (e.g. [13]). In this study we are primarily concerned with the cooling properties of latent heat flux on the surface and air, but not in the urban water balance. Thus, we use the Bowen ratio ($\beta=Q_h/Q_e$) as an additional term in the energy balance equation to account for latent heat flux, Q_e , relative to the magnitude of sensible heat flux, Q_h . The general equation for energy balance at any patch surface (ground, walls, and roof) reads

$$(1 - \alpha)K \downarrow^{m+1} + \epsilon \left(L \downarrow^{m+1} - \sigma (T_{sfc}^{m+1})^4 \right) - \left(1 + \frac{1}{\beta} \right) h^{m+1} \left(T_{sfc}^{m+1} - T^{m+1}(z) \right) - k_1 (T_{sfc}^{m+1} - T_1^m) / \frac{1}{2} \Delta x_1 = 0, \quad (3.3)$$

where α is albedo, $K \downarrow$ and $L \downarrow$ are incident shortwave and longwave radiation, respectively (downwelling for ground and roof; horizontal for the walls), ϵ is the surface emissivity, σ is the Stefan-Boltzmann constant, k_1 and Δx_1 are thermal conductivity and thickness of first solid layer. We have omitted the i patch subscripts and m refers to the time step. This equation is solved iteratively for T_{sfc}^{m+1} by Newton's method (similar to Arnfield [14]). For non vegetated areas the Bowen Ratio term is excluded.

3.2.3 Geometry, Initial, and Boundary Conditions

In the present study we use a 5 by 5 building array resolved by 79×79 patches in the horizontal resulting in a patch length of 3.75 m (Fig. 3.1). Buildings have square footprints of 26.25 m on a side and a height of $z_H = 15$ m. The distance between buildings is 41.25 m ($= 2.75 z_H$) in both x and y directions. Building plan area fraction (λ_p) is 0.15, the frontal area index is $\lambda_f = 0.086$, and the complete-to-plan area ratio (λ_c) is 1.35. This geometry is typical of a low density North American suburban development without trees.

An “urban unit” defines the smallest plan area that encompasses all of the domain’s morphological variation and repeats throughout the domain [8]. Model outputs are computed over the urban unit in the center of the domain, while the remaining buildings provide appropriate radiative boundary conditions (Fig. 3.1).

The simulations start at 0000 LST and run for 24 hours for a cloud-free day (Julian day 172). While this is representative for summer days in California, our results do not apply for different meteorological conditions, especially cloudiness. However, by simulating the summer day with the largest insolation, we obtain an upper bound of the real effects of AT on urban temperatures and fluxes. Initial surface temperatures at 0000 LST are chosen to approximate thermal equilibrium. The initial air temperature inside the building is 22° C.

The top of the domain is in the atmospheric surface layer, where wind speed, above canopy air temperature, and downwelling radiation are specified at twice the building height as follows. The model is forced with meteorological conditions for

coastal southern California, USA [15], the largest market for artificial turf in the US. The clear-sky downwelling shortwave radiation is calculated by the model for a latitude of 33° North. The wind speed is chosen to be constant at $U = 3 \text{ m s}^{-1}$. The above canopy air temperature, T_{air} , is set to the hourly average June air temperature from the Typical Meteorological Year (NSRDB-TMY3) at a representative coastal urban weather station (Miramar, call sign NKX, $32^\circ 52' \text{N}$, $117^\circ 09' \text{W}$, 146.9 m above mean sea level, 10 km from the Pacific Ocean) in San Diego, California. Since it is impossible to simulate all possible scenarios, we present a sensitivity analysis in section 3.3.5 to determine representativeness and evaluate the potential for extrapolation of our results. This offline approach (i.e., using prescribed atmospheric forcing) ignores the feedback from the boundary-layer which serves to blunt the climatic response to surface modification. Hence, the simulations may be expected to provide an upper bound to the different energetic (and therefore climatic) responses to the different ground cover materials [16]. The greater the influence of advection the less important local surface-atmosphere coupling becomes in terms of the evolution of boundary-layer properties. Thus the offline approach would be expected to be more valid in the advective sea-breeze conditions in southern California.

At the bottom of the domain, the temperature boundary condition at the base of the deepest substrate layer serves to drive conductive exchanges with a constant ‘deep soil’ (ground) or ‘internal’ (roofs and walls) temperature. The deep soil temperature is chosen as 16°C .

3.2.4 Material Properties

a. Surface radiative and thermal properties

Table 3.1 presents thermal and radiative properties of AT, grass, asphalt, and concrete. Emissivities of these four materials are similar but their albedos differ significantly. Since no AT albedos could be found in the literature, the AT albedo was measured at two athletic fields with a Kipp & Zonen CM6 thermopile albedometer. Measurements at La Costa Canyon High School AT baseball field in Carlsbad, CA on July 27, 2008 from 1230-1300 PST as well as University of San Diego rugby field on August 6, 2008 at 1315-1345 PST both revealed an albedo of 0.08. The substrate of AT is polyethylene, and hence appropriate thermal properties were obtained (Table 3.1).

TABLE 3.1 Thermal and radiative properties of different ground materials.

	Grass	Artificial turf (polyethylene)	Asphalt	Concrete
Thermal conductivity ($\text{Wm}^{-1}\text{K}^{-1}$)	$1.10^{[17]}$	$0.42^{[20]}$	$0.75^{[19]}$	$1.51^{[19]}$
Heat capacity ($\text{Jm}^{-3}\text{K}^{-1}$)	$2.8 \times 10^{6[17]}$	$0.634 \times 10^{6[20]}$	$1.94 \times 10^{6[19]}$	$2.11 \times 10^{6[19]}$
Momentum roughness (m)	$0.005^{[18]}$	$0.005^{[18]}$	$0.0005^{[21]}$	$0.0005^{[21]}$
Thermal roughness (m)	$0.0005^{[18]}$	$0.0005^{[18]}$	$0.0001^{[21]}$	$0.0001^{[21]}$
Albedo (α) (-)	$0.26^{[19]}$	0.08 (Measurement)	$0.18^{[22]}$	$0.35^{[22]}$
Emissivity (ϵ) (-)	$0.95^{[19]}$	0.95 (Assumption)	$0.95^{[19]}$	$0.90^{[19]}$

b. Subsurface thermal properties

For this idealized case study we chose typical thermal properties for each material and layer, but they will vary greatly in practice (Fig. 3.3). Following Jansson et al. [23], for asphalt and concrete the top layer has a thickness of 0.07 m followed by 0.7 m of crushed rock and 0.6 m of clay soil with a volumetric soil water content of $\theta = 0.4$. We chose a base layer of AT as 5 mm polyethylene over 0.18 m of clay soil ($\theta = 0.1$) followed by 0.5 m of sandy soil ($\theta = 0.4$). Underneath the irrigated grass is a layer of loam soil ($\theta = 0.4$) of thickness 0.05 m over 0.08 m of clay soil with $\theta = 0.4$ followed by 0.1 m of clay soil with $\theta = 0.3$ and 0.5 m of sandy soil ($\theta = 0.4$). Note that the soil moisture is not dynamic or coupled to evapotranspiration, but merely affects heat conduction and storage in the subsurface. To improve the accuracy of the solution to the heat conduction equation in TUF3D, we subdivided these material layers into thinner computational layers and ensured the ratio of thicknesses between all adjacent layers was three or less. Since the thermal damping depths of the subsurface materials are less than 0.14 m, all materials below 0.14 m will not significantly affect our results.

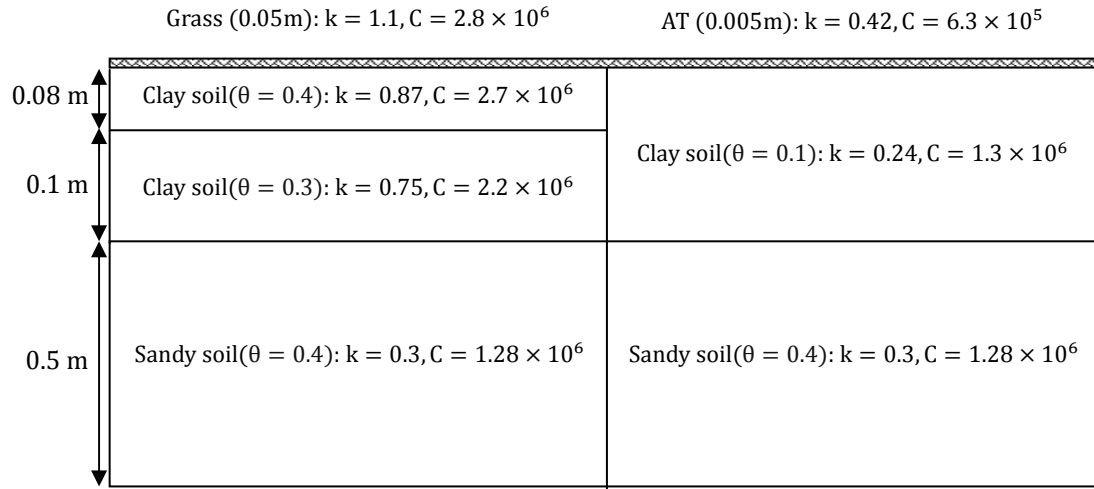


FIG. 3.3a Subsurface layer depths and thermal properties for AT and grass surfaces. k is thermal conductivity (Wm⁻¹K⁻¹), C is heat capacity (Jm⁻³K⁻¹) and θ is volumetric water content.

Asphalt (0.07 m): $k = 0.75$, $C = 1.94 \times 10^6$ / Concrete (0.07 m): $k = 1.51$, $C = 2.11 \times 10^6$

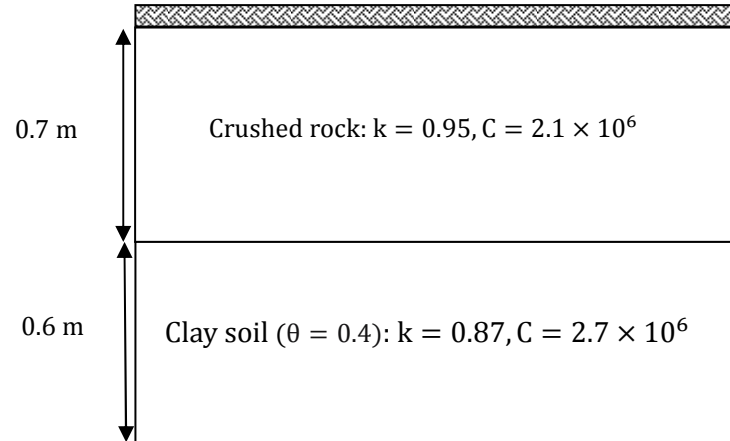


FIG. 3.3b Subsurface layer depths and thermal properties for asphalt and concrete surfaces. k , C and θ are defined as in Fig. 3.3a.

c. Building material radiative and thermal properties

We assume an empty building with no anthropogenic heat production. Thermal and radiative properties of building walls and roof are presented in Table 3.2. The roof parameters are not critical to our study, since the roof does not interact with the ground surface materials. However, the wall parameters are important and their sensitivity will be analyzed in section 3.3.5.

TABLE 3.2 Thermal and radiative properties of building walls and roof.

	Wall			Roof			
	Ply-wood	R-13	Dry wall Gypsum	Asphalt	Ply-wood	R-30	Dry wall Gypsum
Thickness (m)	0.0127	0.088	0.0127	0.01	0.0127	0.2	0.0127
Thermal conductivity ($\text{Wm}^{-1}\text{K}^{-1}$)	0.12	0.038	0.17	0.75	0.12	0.038	0.17
Heat capacity ($\text{Jm}^{-3}\text{K}^{-1}$)	6.62E5	0.02E6	8.72E5	1.94E6	6.62E5	0.02E6	8.72E5
Albedo (α)	0.3	-	-	0.15	-	-	-
Emissivity (ϵ)	0.88	-	-	0.92	-	-	-

3.2.5 Effects of ground surface properties on the urban canopy

The different thermal and radiative properties of asphalt, concrete, grass, and AT (Table 3.1) result in different ground surface temperatures which in turn affect heat transfer to the urban canopy. If the choice of a ground surface material is motivated by building energy efficiency considerations, the thermal interactions between ground surfaces and buildings are of particular interest. Ground surface temperature affects building wall temperature (and heat flux) through longwave emission (L ; Fig. 3.2). L is determined by surface temperature, emissivity, and view factors:

$$L_{ground_to_wall} = \psi_{ground,wall} \epsilon \sigma T_{ground}^4, \quad (3.4)$$

in which $L_{ground_to_wall}$ (W m^{-2}) is the upwelling longwave radiation, per unit area of ground, from ground patches incident on wall patches; $\psi_{ground,wall}$ is the wall view factor of the ground and T_{ground} is the ground surface temperature which depends on surface type.

Similarly, the transfer of heat from ground to wall through shortwave reflection is

$$S_{ground_to_wall} = \psi_{ground,wall} \alpha S_{dn}, \quad (3.5)$$

It depends on the ground surface albedo, α , view factor, and the incident global (direct and diffuse) shortwave flux density on the ground, S_{dn} (W m^{-2}). The net longwave and shortwave radiation between ground and wall are then calculated by substituting respective temperature, emissivity, albedo and view factor in Eqs. (3.4) and (3.5).

$$\begin{aligned}
 RL_{net} &= L_{ground_to_wall} - L_{wall_to_ground} \\
 RS_{net} &= S_{ground_to_wall} - S_{wall_to_ground}
 \end{aligned}
 \tag{3.6}$$

In the simple TUF3D convection model, ground surface temperature indirectly affects building wall temperatures through heating of the canopy air, which in turn modulates the wall-canopy air temperature difference and resulting wall heat flux (Fig. 3.2, Eq. 3.1).

Heat fluxes and temperatures in the urban canopy vary over the course of the day. We will use maximum and aggregate quantities where appropriate to quantify the thermal impacts of the different ground surfaces on temperatures and heat fluxes on urban canopy temperatures and building energy use. *Maximum* surface and air temperatures and ground and wall energy balance fluxes are not directly related to total building energy use. However, they may be related to peak building energy use affecting electric grid stability and electricity rates. The *aggregate* heat fluxes (cumulative heat fluxes over a day in $\text{kWh m}^{-2}\text{day}^{-1}$) and their differences give better information on the total heat exchange and resulting building energy use.

3.2.6 Sensitivity study and limitations

In this first study of the thermal impact of AT, it is not possible to assess the full diversity of urban landscapes. Here we focus on an area and climate where AT is most common and most likely to see increased use. The low built-up fraction (15%) and the absence of roads may approximate suburban gated communities with narrow walkways, but these conditions are unrealistic for most residential areas. However,

model limitations and a desire for generality motivate our simple approach. Since actual material properties and geometrical and meteorological conditions vary, we conducted a sensitivity analysis to determine the sensitivity of building wall, T_{wall} , and canopy air temperatures, T_{can} , to wind speed, above canopy air temperature (T_{air}), ground properties (albedo, thermal conductivity, and heat capacity), geometric-radiative parameters (building plan area fraction, frontal area ratio, latitude) and Bowen Ratio. We repeated the grass and AT simulations varying these parameters by $\pm 20\%$ and tabulated the resulting change in air and wall temperatures.

We acknowledge that the absence of field experimental data to validate our modeling results is a limitation of our study. However, conducting neighborhood scale field experimental studies of heat exchange is a cost and labor intensive task, which could not be afforded. The validation for specific urban environments by KV07 shows that TUF3D generally performs well in modeling urban surface temperatures.

3.3 Results

3.3.1 Diurnal cycle of urban temperatures

We choose grass as the reference surface, as it is still the most frequently used surface type in landscaping and community design. Fig. 3.4 presents the temperatures of the urban facets, canopy air, and building internal air over 24 hours. Results are averages over all patches that compose each surface or facet, e.g. ground, roofs and walls. T_{wall} is the average temperature of all four walls of a building, each of which undergoes a very different diurnal cycle. The highest temperature of the urban surfaces

on this day are 50.6°C for the roof (1200 LST), 31.3°C for ground (grass) (1300 LST), 31.6°C for building wall (1400 LST), and 23.6°C for canopy air (1200 LST). Due to evaporative cooling and reduced insolation the ground temperature is lower than the roof temperature, but still larger than the canopy air temperature. The building wall surfaces remain cooler during midday since their vertical orientation causes them to receive less insolation. At night all of the urban surface temperatures are similar except for the roof where longwave cooling results in lower temperatures. Due to insulating properties of the building materials the internal building temperature has a small amplitude.

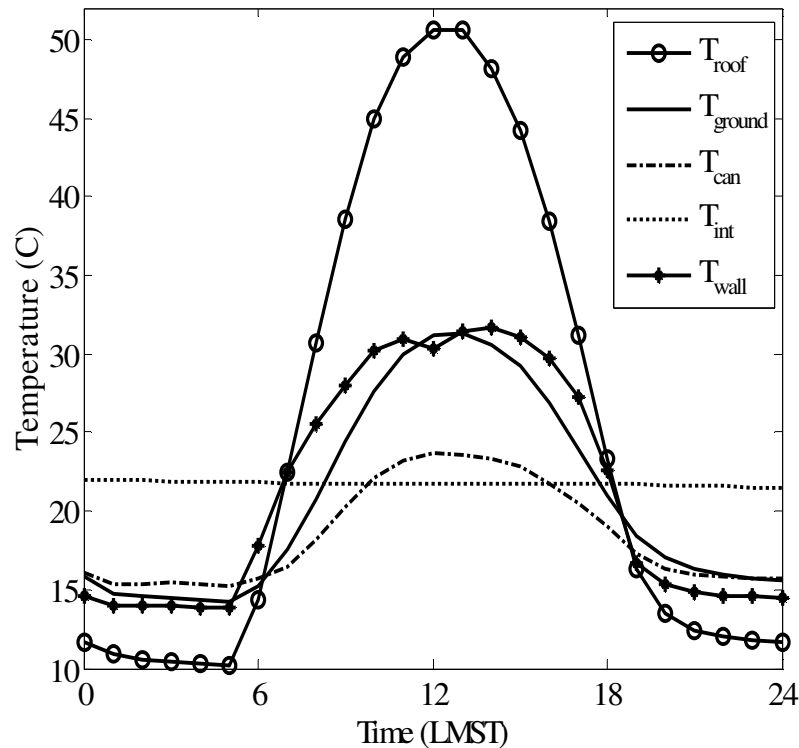


FIG. 3.4 Modelled urban facets, canopy air, and building internal air temperatures for a community covered with a grass surface on a clear summer day in coastal southern California. (T_{roof} , T_{ground} , T_{can} , T_{int} , and T_{wall} are the roof, ground, canopy air, internal building air, and building wall temperatures, respectively.)

We now quantify the effects of other surface materials on the urban energy balance with a focus on artificial turf (AT). Fig. 3.5 compares ground, canopy air, and building wall temperatures for AT, asphalt, grass, and concrete surfaces over 24 hours. While all urban surface temperatures are similar at night, all other materials become significantly warmer than grass during the day. The maximum ground temperature increases compared to grass by 21.2°C for asphalt (at 1300 LST), 22.6°C for AT (at 1200 LST), and 16.2°C for concrete (at 1300 LST). The peak ground temperatures for asphalt and concrete lag due to their larger thermal inertia. In contrast, the canopy air temperatures T_{can} all peak at 1200 LST and the maximum T_{can} for asphalt, AT and concrete are 0.8°C , 1.8°C , and 0.6°C higher than for grass, respectively, assuming no coupling to boundary-layer (forcing) temperature. Given almost constant interior building temperatures, building wall temperatures, T_{wall} , are linearly related to the conductive heat flux into the building. Peak average T_{wall} (at 1400 LST) for asphalt, AT and concrete are 2.0°C , 1.3°C , and 3.1°C higher than that with grass ground cover, respectively. The difference between AT and grass is approximately constant between 1000-1400 LST, but it becomes negligible at about 1700 LST.

3.3.2 Diurnal cycle of urban heat fluxes

Fig. 3.6 shows the energy balance components at the ground surface for grass and AT. Assuming $\beta = 0.3$, the latent heat flux Q_e is the dominant means of heat removal from the grass surface. For example, at noon Q_e is $0.57 R_{net}$, Q_h is $0.17 R_{net}$, and Q_g is $0.26 R_{net}$. Over the day the total latent heat flux is 2.5 kWh m^{-2} implying

an evaporation rate of 3.6 mm day^{-1} (per m^2 of grass) or 3.0 mm day^{-1} (per m^2 of urban area). Note that for the other ground materials (AT, asphalt, and concrete) $Q_e = 0$. The resulting increase in Q_h , sensible heat flux, increases T_{can} .

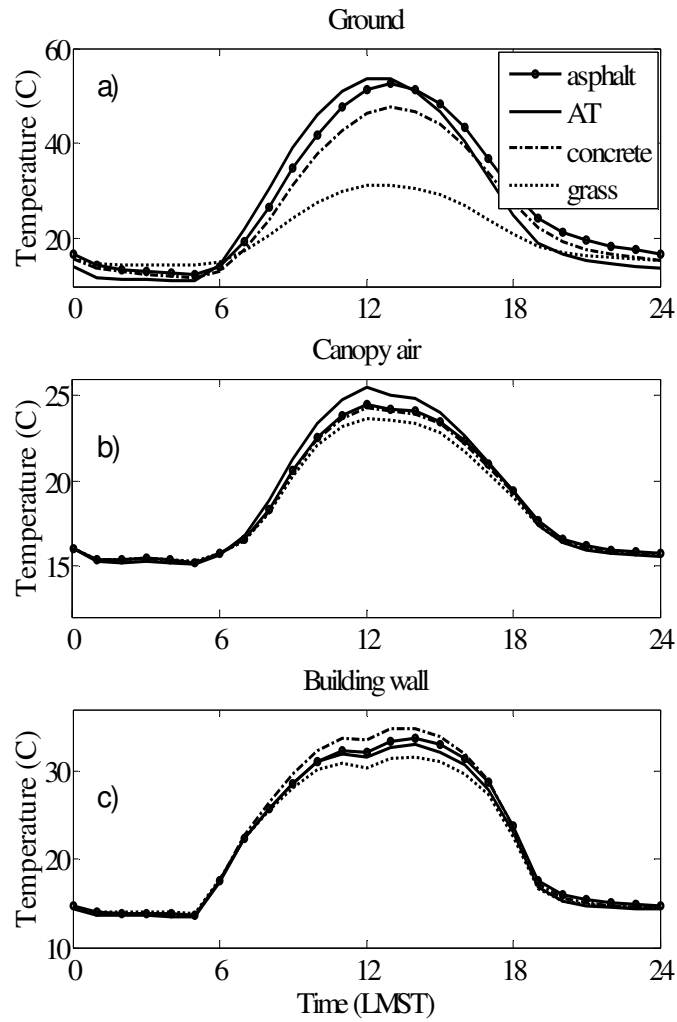


FIG. 3.5 Comparison of a) ground surface, b) canopy air, and c) building wall-average temperatures for AT, grass, asphalt, and concrete surfaces.

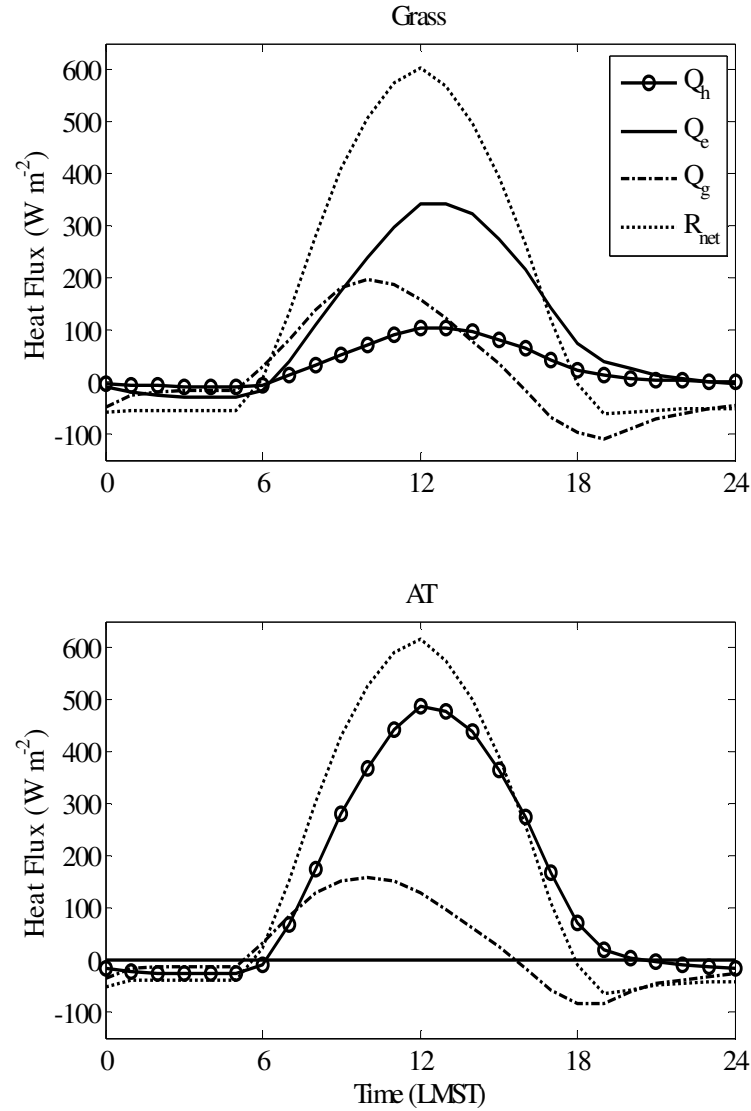


FIG. 3.6 Modelled energy balance components for the grass and AT surfaces. Q_h , Q_e , and Q_g are sensible, latent, and ground heat fluxes, respectively. R_{net} is the net radiation.

Fig. 3.7 shows energy balance components at the outside surface of the R-13 building wall for grass and AT ground covers. The maximum net radiation is about 140 W m^{-2} with a dip around noon when the small solar zenith angle reduces the shortwave radiation intensity per m^2 of wall. Due to wall insulation the conductive flux into the building is much smaller than the convective flux. The wall net radiation

for AT is slightly smaller than that for grass. However, the larger T_{can} leads to reduced temperature spread between canopy air and wall, and hence smaller Q_h .

3.3.3 Radiative exchange between building and ground

The direct impact of ground surface materials on urban energy use is primarily through radiative exchange between building and ground and resulting effects on T_{wall} , building wall temperature, and Q_{g-wall} (Fig. 3.2, Eqs. 3.4-3.6). Since the emissivities of different materials are similar (Table 3.1) $L_{ground_to_wall}$ is strongly correlated to ground temperature to the fourth power (Figs. 3.8a, 3.5a). Consequently, AT and asphalt transfer the most longwave radiative flux to the building, followed by concrete, and grass a distant fourth. Ultimately the radiative effect of a surface material is described by the net exchange of longwave radiation RL_{net} between building wall and ground. Since $L_{ground_to_wall}$ affects the wall temperature (Fig. 3.5c), there is a dynamic feedback on RL_{net} through $L_{wall_to_ground}$. The maximum RL_{net} (per unit area of wall surface) for AT is 39.7 W m^{-2} at 1200 LST, which is much larger than for grass (Table 3.3, Fig. 3.8d).

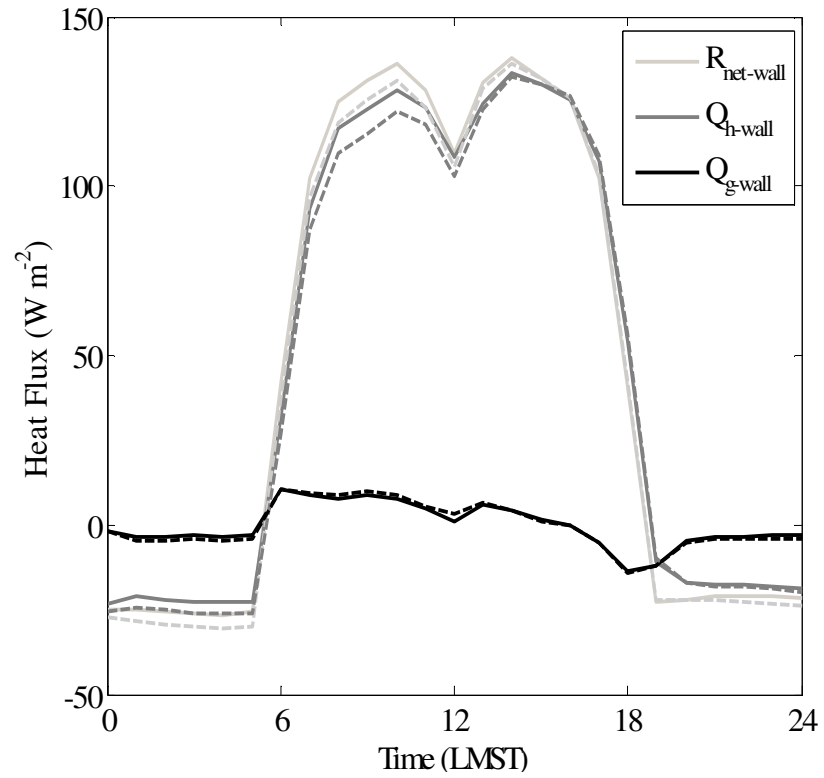


FIG. 3.7 Energy balance components averaged over the four walls for grass (solid line) and AT (dashed line). Q_{h-wall} is the wall-to-canopy sensible heat flux, Q_{g-wall} is the conduction heat flux into the wall, and $R_{net-wall}$ is the net radiation on the building walls after multiple reflections. Area units refer to wall surface area.

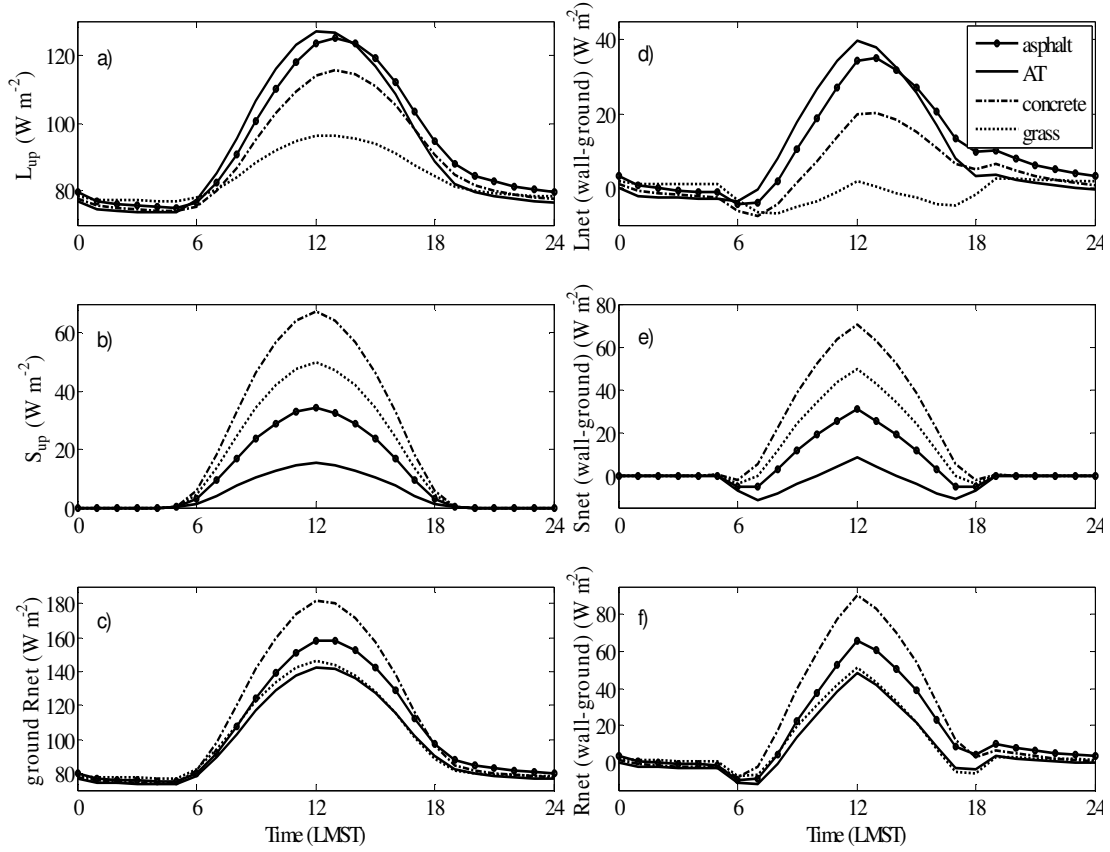


FIG. 3.8 a) Longwave radiation, b) shortwave radiation, and c) total radiation from ground to building wall for different ground materials in W per m^2 of ground surface area. d) Net longwave radiation, e) net shortwave radiation, and f) net radiation flux between ground and building wall in W per m^2 of wall.

The impact of ground material properties on building wall temperature through shortwave radiation (Eq. 3.5, 3.6) is non-trivial, since multiple reflections of shortwave radiation occur in the urban canopy. Compared to other surfaces, concrete shows the largest $S_{\text{ground_to_wall}}$ because of its higher albedo (0.35, Table 3.1), while AT shows the smallest $S_{\text{ground_to_wall}}$ (Fig. 3.8b). The maximum $S_{\text{ground_to_wall}}$ for AT is 34 W m^{-2} less than that for grass. Considering reflection of solar radiation from walls to the ground (wall albedo is 0.3), the maximum RS_{net} for AT is 8.41 W m^{-2} (per unit area of wall surface) which is significantly smaller than RS_{net} for other

materials (Table 3.3, Fig. 3.8e). In fact, net shortwave radiation exchange with AT is a heat sink for building walls for most of the day.

The total upwelling radiative flux (the sum of long and shortwave radiative fluxes from the ground to the building wall) is similar for AT and grass, while asphalt and especially concrete show larger upwelling radiative fluxes (Fig. 3.8c). The net effect of different longwave and shortwave contributions is the overall net radiation between ground and building walls (Fig. 3.8f, note: in units of wall area). Compared to grass, the direct effect of AT is a reduction in net radiative heat flux between ground and building walls. The peak is reduced by 3.2 W m^{-2} and the 24 hour total is reduced by $56 \text{ Wh m}^{-2} \text{ day}^{-1}$. This seems counterintuitive as AT surface temperatures are much larger than those for grass. However, the net radiation is dominated by the reduction in shortwave solar reflected radiation through the low albedo (Fig. 3.8e). Thus considering only radiative effects, installing AT cools adjacent buildings.

TABLE 3.3 Maximum radiative flux densities between ground and wall and their timing in the day. All maxima in shortwave radiation occur at 1200 LST.

	AT	Asphalt	Concrete	Grass
Max longwave (ground to wall)				
(Wm^{-2} of ground)	127	125	115	96.4
Time [LST]	12	13	13	13
Max net longwave				
(Wm^{-2} of wall)	39.7	34.9	20.3	1.8
Time [LST]	12	13	13	12
Max shortwave (ground to wall)				
(Wm^{-2} of ground)	15.2	34.4	67.6	49.9
Max net shortwave (Wm^{-2} of wall)	8.41	31.2	70.5	49.6

3.3.4 Convective heat exchange between building and ground

Ground materials indirectly affect building wall temperature, T_{wall} , through convection or Q_h which is parameterized as a function of the temperature difference between surface and air (Eq. 3.1). Since above-canopy air temperature is an input boundary condition in TUF3D, the indirect effect of urban ground materials on buildings is through increased T_{can} (Fig. 3.2). A larger ground-to-canopy Q_h increases T_{can} , which in turn reduces the building wall-to-canopy heat flux increasing T_{wall} , wall temperature.

As expected considering Eq. 3.1 and T_{can} in Fig. 3.5b, Fig. 3.9a shows that Q_h from the ground to the canopy air for AT is larger than for all other ground covers with a maximum of 487 W m^{-2} (Table 3.4). This compares to a maximum roof heat flux of 568 W m^{-2} .

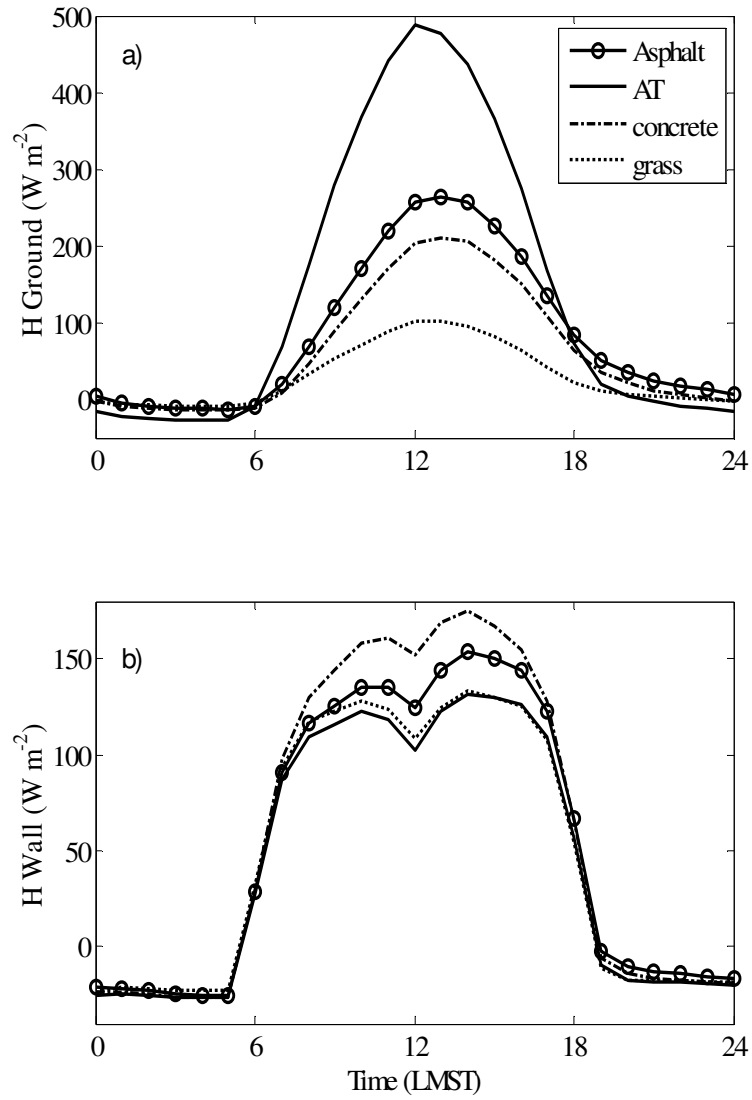


FIG. 3.9 Comparison of sensible heat flux from a) ground and b) building walls to canopy air for AT, grass, asphalt, and concrete. Building wall sensible heat fluxes are averaged over all walls and shown per unit of wall area.

TABLE 3.4 Magnitude and timing of maximum sensible heat fluxes from ground, wall and roof to canopy air.

	Max ground sensible heat flux (Wm ⁻² of ground)	Time [LST]	Max wall sensible heat flux (Wm ⁻² of wall)	Time [LST]	Max roof sensible heat flux (Wm ⁻² of roof)	Time [LST]
AT	487	12	132	14	568	12
Asphalt	264	13	154	14	576	12
Concrete	211	13	175	14	581	12
Grass	103	13	133	14	582	12

The average Q_h from building walls to canopy air (Fig. 3.9b) increases throughout the day until wall temperatures reach their maximum around 1400 LST. Table 3.4 shows that the maximum Q_h convective heat transfer from wall to air with AT as ground cover is 132 W m⁻² which is less than for grass and significantly less than for concrete and asphalt.

Heat also escapes the urban canopy layer and is mixed throughout the atmospheric boundary layer (ABL) leading to non-local effects. Since the surface layer temperature T_{air} is prescribed as a fixed boundary condition (Fig. 3.2), the effect of different urban surfaces on temperatures in the urban surface layer and ABL cannot be obtained from TUF3D alone. To estimate these effects offline we assume that the sensible heat flux from the canopy heats the well-mixed, dry, and deep ABL equally over a depth of 2 km with 1.1 kg m⁻³ air density and 1004.67 J kg⁻¹ K⁻¹ heat capacity. We do not consider the entrainment through the ABL top. In the first offline scenario the ABL air is assumed to linger or ‘recirculate’ over the model domain and thus continues to accumulate the heat emitted by the surface. By accumulating the heat

fluxes over a day we obtain the energy entering to the ABL and the resulting heating (Table 3.5). Compared to grass, AT emits an additional 2.3 kWh m^{-2} of heat to the ABL resulting in a temperature increase of 3.7° C . The offline nature of this scenario makes these numbers high estimates, as rising boundary-layer temperatures resulting from increased sensible heat flux from the canopy air with AT would in reality blunt the process, at least to the extent that the local surface affects the local boundary-layer (i.e., depending on the advective influence).

In the second more realistic offline scenario we consider the typical sea-breeze conditions in coastal areas with a shallower thermal internal boundary layer of 500 m thickness [24]. Assuming a mean boundary layer wind speed of 5 m s^{-1} we estimate the convective heating from the surface for each kilometer that it passes over an urban area. For this scenario, the temperature increases due to canopy sensible heat flux of grass, concrete, asphalt, and AT are $0.042^\circ \text{ C km}^{-1}$, $0.078^\circ \text{ C km}^{-1}$, $0.09^\circ \text{ C km}^{-1}$, and $0.15^\circ \text{ C km}^{-1}$, respectively. The evaporation from grass increases the specific humidity by $2.86 \times 10^{-4} \text{ g kg}^{-1} \text{ km}^{-1}$.

TABLE 3.5 Cumulative sensible heat fluxes over a day from the urban canopy and roof top to the atmospheric boundary layer (ABL) and the resulting air temperature differences ΔT averaged over a stagnant dry ABL of thickness 2 km.

	Sensible heat flux from canopy to above canopy (kWhm^{-2} of urban area)	ΔT ($^\circ \text{C}$)	Sensible heat flux from roof top to above canopy (kWhm^{-2} of urban area)	ΔT ($^\circ \text{C}$)
Grass	1.11	1.8	0.6	0.98
Concrete	1.93	3.1	0.6	0.98
Asphalt	2.32	3.7	0.6	0.98
AT	3.41	5.5	0.59	0.96

3.3.5 Sensitivity study

Table 3.6 shows the sensitivity of the maximum wall and canopy air temperatures T_{can} to wind speed, ground properties, building geometry, Bowen Ratio, above canopy air temperature (T_{air}), and latitude for the grass and AT surfaces. While T_{can} is very sensitive to T_{air} (as expected), it shows almost no sensitivity to thermal properties and latitude. T_{can} is most sensitive to the frontal area ratio λ_f and weakly sensitive to wind speed and Bowen Ratio. The wall temperature T_{wall} is less sensitive to λ_f than T_{can} , but more sensitive to the other parameters, especially (in order of sensitivity) wind speed, ground albedo, latitude, building plan area ratio λ_p , and Bowen Ratio. As expected, wind speed is anticorrelated with T_{wall} , while ground albedo, Bowen Ratio, T_{air} , λ_p and latitude are positively correlated with T_{wall} . Most notably, an increase in the ground albedo causes a strong increase in wall temperature especially for grass, which supports the argument that a large albedo at ground level may increase heat conduction into buildings. Generally the T_{wall} sensitivity for grass and AT are comparable indicating robustness of our results. The direction of the effect or the magnitude of the sensitivity varies between the 20% increases and 20% decreases suggesting some non-linearity in the model.

For the soil types specified in our study the thermal damping depth ranges from 0.10 to 0.14 m, so the soil layers below 0.14 m do not contribute significantly to the surface energy budget. At a depth equal to three times the damping depth, the range in temperature is 5% of that at the surface [25].

TABLE 3.6 Sensitivity of T_{can} and T_{wall} for grass and AT to wind speed, ground properties, λ_p , λ_f , above canopy air temperature, Bowen Ratio and latitude. The units of the sensitivity are °C per 20% change in the property listed in the first column. Base values for ground properties are presented in Table 3.1, and for λ_p , λ_f and latitude are presented in section 3.2.3. The reference values are: wind speed of 3 m s⁻¹, maximum T_{air} of 22.67 °C, and Bowen Ratio of 0.3.

		$(T_{can})_{max}$ sensitivity grass	$(T_{wall})_{max}$ sensitivity grass	$(T_{can})_{max}$ sensitivity AT	$(T_{wall})_{max}$ sensitivity AT
Wind speed (m s ⁻¹)	-20%	-0.09	-0.83	-0.11	-0.93
	+20%	-0.08	-0.71	-0.12	-0.82
Ground albedo	-20%	-0.02	0.54	-0.03	0.11
	+20%	-0.03	0.55	-0.04	0.11
Ground thermal conductivity (Wm ⁻¹ K ⁻¹)	-20%	-0.01	-0.01	0.00	-0.01
	+20%	-0.01	0.00	0.01	0.05
Ground heat capacity (Jm ⁻³ K ⁻¹)	-20%	-0.01	-0.01	-0.01	-0.04
	+20%	-0.01	-0.01	-0.01	0.00
Building plan area ratio (λ_p)	-20%	0.01	0.14	-0.08	0.10
	+20%	0.06	0.20	-0.01	0.18
Frontal area ratio (λ_f)	-20%	-0.2	0.04	-0.5	-0.22
	+20%	-0.05	-0.01	-0.21	-0.03
Latitude	-20%	0.00	0.47	-0.03	0.49
	+20%	-0.01	0.43	-0.08	0.36
Air temperature (°C)	-20%	4.5	4.2	4.5	4.26
	+20%	4.49	4.19	4.49	4.24
Bowen Ratio	-20%	0.08	0.15	-	-
	+20%	0.07	0.13	-	-

3.4 Discussion and Conclusions

3.4.1 Direct Temperature and heat flux effects of AT on nearby buildings

The Temperatures of Urban Facets in 3-D (TUF3D) model was used to compare the impact of different ground surface materials (artificial turf (AT), grass, asphalt, and concrete) on urban canopy layer energy exchange and building energy use. Our comparison covers a clear summer day over a uniform array of buildings at a latitude of 33° with building plan area fraction (λ_p) of 0.15, and frontal area fraction (λ_f) of 0.086.

Comparison of ground surface temperature (Fig. 3.5a) shows that – as expected – evaporative cooling makes grass by far the coolest surface compared to asphalt, AT, and concrete. This results in larger longwave radiation fluxes (Fig. 3.8a) from AT – as well as asphalt and concrete – providing substantially more radiative heat to the building walls than grass. However, the total radiative heat transfer from ground to building wall is the sum of reflected solar shortwave and thermal longwave radiation. Since AT has the lowest albedo of the urban surface materials (or almost any surface in the environment, for that matter), AT leads to a substantial reduction in shortwave radiative heat transfer from the ground to the building (Fig. 3.8b) balancing the increase in longwave radiation. From this point of view the low albedo of AT is a positive characteristic.

The largest sensible heat flux from ground to canopy occurs over AT (Fig. 3.9). The reasons are high surface temperature (Fig. 3.5a), lack of water availability (unlike grass), and higher surface roughness (than asphalt and concrete, Table 3.1).

Hence AT increases the canopy temperature (Fig. 3.5b). The associated decrease in building wall-to-canopy sensible heat fluxes increases building wall temperatures and wall conductive heat fluxes.

3.4.2 Implications of AT on energy use

In this analysis we neglect energy use related to production and disposal of AT, as well as grass maintenance (lawn mowing, fertilizer), which we deem small over the lifecycle. Then, the effect of a ground surface material on building energy use will be a function of heat gain or loss due to conduction into the building (Q_{g-roof} and Q_{g-wall} , Fig. 3.2), leakage or ventilation of indoor air, and shortwave transmission through windows. With the exception of Q_{g-wall} and Q_{g-roof} , these processes are not explicitly simulated in TUF-3D, so the simulated indoor air temperature (Fig. 3.4) describes that of an unventilated building without windows. The maximum Q_{g-wall} at the innermost wall layer for grass is 4.3 W m^{-2} and for AT is 4.8 W m^{-2} (Fig. 3.10). Thus compared to grass, AT increases the conductive heat gain through walls by 10% corresponding to 788 W at peak over the surface area of the building. Note that Q_{g-wall} is strongly dependent on building envelope parameters, in particular the thermal conductivity, heat capacity, and window fraction. For a given wall net radiation the relative resistance to heat transfer into the building wall versus convectively into the canopy will determine the ratio of Q_{g-wall} to canopy sensible heat flux. Thus our results for Q_{g-wall} apply mostly to post 1980 construction that follows California Title 24 building standards [26].

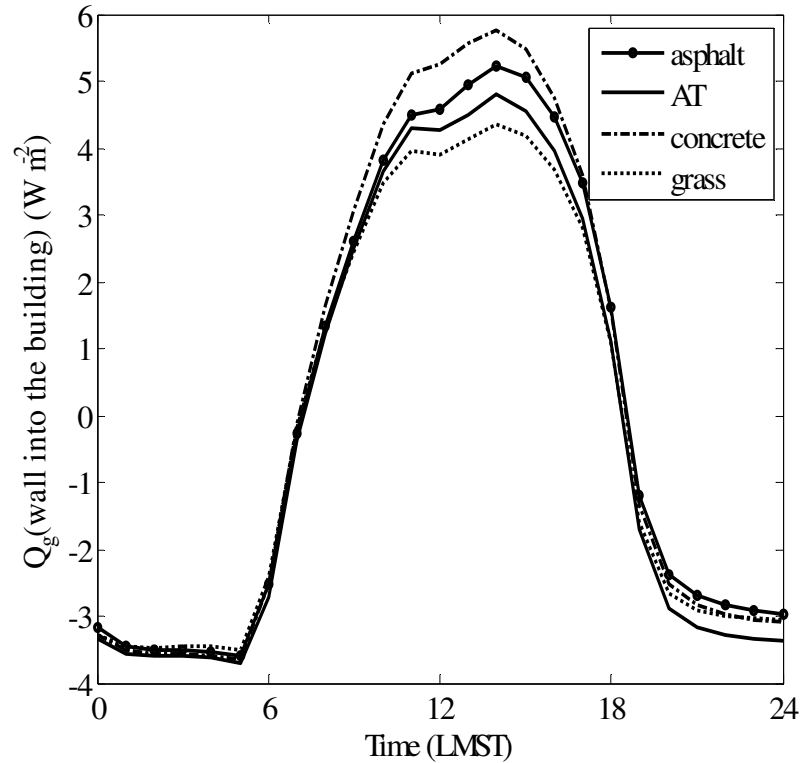


FIG. 3.10 Comparison of Q_{g-wall} at the innermost wall layer for AT, grass, asphalt, and concrete. Q_{g-wall} is averaged over all walls and shown per unit of wall surface area.

Offline modeling was used to quantify total building energy use using the “nonresidential cooling load calculation” method of the American Society of Heating, Refrigerating and Air-Conditioning Engineers (ASHRAE [27]). In this method the cooling load is the aggregate of conductive heat gain through windows, walls, and roofs; solar heat gain through fenestrations; internal heat gain from lights, people, and equipment; and the heat gain or loss from infiltration and ventilation. We calculated cooling load for AT and grass at a typical summer peak load time at 1400 LST assuming (i) zero internal heat gain, (ii) 20% of wall surface area are windows with a solar heat gain coefficient of 0.4 and without blinds, (iii) comfort internal building

temperature of 74° F (~ 23° C), and (iv) no fan energy use. The cooling load caused by radiation through windows (Table 3.7) dominates the total cooling load and is larger for grass than AT due to the larger grass albedo (Fig. 3.8b). The significant wall insulation and relatively cool outdoor air in the selected climate zone cause the conduction and ventilation cooling loads to be small compared to the window radiative cooling load. AT does however cause an increase in the cooling loads for ventilation and conduction due to the higher canopy air temperature.

Moreover, since water has an embodied energy (i.e. energy that was used in making a product) related to supply, conveyance, treatment, and distribution, the air cooling effects of water come at an (energy) price. For outdoor uses in southern California, the California Energy Commission (CEC, 2006) estimated water embodied energy at 11 MWh MG⁻¹. Given our ET estimate of 3.6 mm day⁻¹ per m² of grass, and the landscaping area associated with one building of 3867 m², we estimate a water use of 13.9 m³ day⁻¹ or 3678 G day⁻¹. Consequently the associated energy use would be 40 kWh day⁻¹, which corresponds to a constant power draw of 1.7 kW. This is larger than the online wall heat flux (Fig. 3.10) and about equal to the offline cooling load penalty of AT during the peak hour (Table 3.7) if window radiation is ignored, and can be expected to be larger than said penalty over the day. The reduction in water use contributes to the overall local positive energy balance of AT compared to grass.

TABLE 3.7 Building heat gain through different physical processes and surfaces according to ASHRAE [27] for grass and AT.

Cooling load corresponds to heat gain through	For grass [kW]	For AT [kW]
Roof conduction	1.17	1.27
Wall conduction	2.79	3.22
Glass conduction	-0.70	0.32
Infiltration	0.08	0.55
Non-glass radiation subtotal	3.34	5.36
Glass radiation	38.2	29.4
Total	41.54	34.76

AT has non-local effects on urban energy use through enhanced canopy layer temperatures increasing infiltration and ventilation energy use downwind of AT. This non-local effect would be largest on days with calm winds as heat would accumulate over the day (Table 3.5). In moderate winds the additional heating compared to grass may be as much as 0.11°C per kilometer that the ABL interacts with an urban area. As they are derived from offline modeling, these results may somewhat overestimate the thermal impacts of AT on the boundary-layer. To minimize non-local temperature impacts in urban areas with persistent wind directions, AT could be installed preferentially on downwind sides of the urban area. Bornstein et al. [28] demonstrated that in California additional inland heating as a result of global warming decreases coastal temperatures, likely through an increase in the sea breeze intensity. Increased

inland (i.e. downwind) installation of AT would presumably strengthen this effect, leading to a more complex mesoscale coupling that is beyond the scope of this study.

The increase in non-local energy use caused by AT is estimated using the concept of cooling degree days (CDD [26]). The CDD are computed by subtracting 65°F (~18°C) from the average of daily maximum and minimum temperatures [29]. We assume that the average grass fraction in California's urban areas is 22% [30] and linear scaling of the results in Table 3.5 with AT and grass land cover fraction.

From the NSRDB-TMY3 temperatures at Miramar airport weather station and the results in Table 3.5 for stagnant or recirculating air (the worst case) we determined that replacing all natural grass surfaces with AT would cause an additional 0.6° C CDD. For California, the DOE Energy Efficiency and Renewable Energy [31] website states that 5.0 kWh in energy are used per capita per CDD (in °C). Assuming the typical persons per household in a building (2.87), on a typical summer day AT would be responsible for $\frac{5.0 \text{ kWh}}{\text{person CDD}} \times 2.87 \text{ persons} \times 0.6 \text{ CDD} = 8.61 \text{ kWh day}^{-1}$ in additional energy use which is small compared to the values in Table 3.7. We note that this number would be much larger for warmer locations.

In summary, the net effect of replacement of grass surfaces with AT in coastal southern California is a net water and energy savings. This is a somewhat unexpected result. While our results appear to be reasonably insensitive to model parameters, more comprehensive analyses of the effects of AT in different building fabrics and climate zones will be necessary to robustly estimate the energy impacts of widespread AT installation. Furthermore online modeling of the interactions between buildings

and their environment throughout the year would potentially yield more accurate results. We also note that other landscaping options such as low water use plants are available which would significantly reduce water and its embodied energy use compared to grass. Since the albedo of low water use plants typically is lower than that of grass, we would expect that low water use plants would have similar effects as AT.

Acknowledgements

We acknowledge funding by the Hellman Foundation and NSF CBET-0847054. Samer Naif assisted with albedo measurements of artificial turf. We thank the University of San Diego and La Costa Canyon High School for allowing access to their athletic fields. Thanks to Anthony Dominguez (UCSD) and Ronnen Levinson (Lawrence Berkeley National Lab) for suggesting materials and thermal parameters for California buildings. Three anonymous reviewers helped in substantially improving the manuscript.

The text and data in chapter 3, in full, is a reprint of the material as it appears in “Modeling the thermal effects of artificial turf on the urban environment”, Yaghoobian, Neda; Kleissl, Jan; Krayenhoff, E. Scott, *Journal of Applied Meteorology and Climatology*, 49, 332–345 (2010) © American Meteorological Society (Used with permission). The dissertation author is the primary investigator and author of this article.

References

- [1] T. R. Oke, The energetic basis of the urban heat island. *Quarterly Journal of the Royal Meteorological Society*, 108 (1982) 1–24.
- [2] T. R. Oke, G. Johnson, D. Steyn, and I. Watson, Simulation of surface urban heat islands under ‘ideal’ conditions at night. Part 2: Diagnosis of causation. *Boundary-Layer Meteorol*, 56 (1991) 339–358.
- [3] S. Dhakal, and K. Hanaki, Improvement of urban thermal environment by managing heat discharge sources and surface modification in Tokyo. *Energy and Buildings*, 34 (2002) 13–23.
- [4] R. Giridharan, S. Ganesan, and S. Lau, Daytime urban heat island effect in high-rise and high-density residential developments in Hong Kong. *Energy and Buildings*, 36 (2004) 525–534.
- [5] R. Bornstein, Mean diurnal circulation and thermodynamic evolution of urban boundary layers. *Modelling the Urban Boundary Layer*. Amer. Meteor. Soc., (1987) 53–94.
- [6] E. L. Kruger and D. Pearlmutter, The effect of urban evaporation on building energy demand in an arid environment. *Energy and Buildings*, 40 (2008) 2090–2098.
- [7] G. Galassi and G. Bortolin, New study finds artificial turf may be too hot for summer use. [Available online at www.news.dri.edu/nr2008/Artificial_Turf_Research_091808.pdf], cited 2009.
- [8] E. S. Krayenhoff and J. A. Voogt, A microscale three-dimensional urban energy balance model for studying surface temperatures. *Boundary-Layer Meteorol*, 123 (2007) 433–461.
- [9] E. S. Krayenhoff, A micro-scale 3-D urban energy balance model for studying surface temperatures. Unpublished M.Sc. Thesis, University of Western Ontario, London, Canada, 232 pp, 2005.
- [10] I. Ashdown, *Radiosity: a programmer’s perspective*. John Wiley & Sons, New York, 496 pp, 1994.
- [11] P. Mascart, J. Noilhan, H. Giordani, A modified parameterization of flux–profile relationships in the surface layer using different roughness length values for heat and momentum. *Boundary-Layer Meteorol*, 72 (1995) 331–344.
- [12] I. Harman, J. Barlow, and S. Belcher, Scalar fluxes from urban street canyons. Part II: model. *Boundary-Layer Meteorol*, 113 (2004) 387–409.

- [13] C. S. B. Grimmond and T. R. Oke, Turbulent Heat Fluxes in Urban Areas: Observations and a Local-Scale Urban Meteorological Parameterization Scheme (LUMPS). *J. Appl. Meteorol.*, 41 (2002) 792– 810.
- [14] A. Arnfield, Canyon geometry, the urban fabric and nocturnal cooling: a simulation approach. *Physical Geography*, 11 (1990) 220–239.
- [15] California climate zone 7, cited 2009: Title 24 Requirements. [Available online at http://www.pge.com/includes/docs/pdfs/about/edusafety/training/pec/toolbox/arch/climate/california_climate_zone_07.pdf.]
- [16] E. S. Krayenhoff and J. A. Voogt, Sensitivity testing of an urban surface scheme coupled to a 1-D boundary layer model. Preprints of the Fifth Symposium on the Urban Environment, Vancouver, Canada, American Meteorological Society, 2004.
- [17] G. S. Campbell and J. M. Norman, *An Introduction to Environmental Biophysics*. Springer, 286 pp, 1998.
- [18] W. Brutsaert, *Evaporation Into the Atmosphere*. D. Reidel Publ. Co., 299 pp, 1982.
- [19] T. R. Oke, *Boundary Layer Climates*. Methuen, London, 435 pp, 1987.
- [20] J. G. Speight, *Lange's Handbook of Chemistry* (16th Edition). McGraw-Hill, 2005.
- [21] D. Chen, T. Gustavsson, and J. Borgen, The applicability of similarity theory to a road surface. *Meteorological Applications*, 6 (1999) 81–88.
- [22] M. Iqbal, *An Introduction to Solar Radiation*. Academic Press, 390 pp, 1983.
- [23] C. Jansson, E. Almkvist, and P. Jansson, Heat balance of an asphalt surface: observations and physically-based simulations. *Meteorological Applications*, 13 (2006) 203–21.
- [24] A. Venkatram, Improvement of Short-Range Dispersion Models to Estimate Air Quality Impact of Power Plants in Urban Environments. California Energy Commission, PIER Energy-Related Environmental Research Program. CEC-500-2007-096, 2008.
- [25] G. B. Bonan, *Ecological Climatology*. Cambridge Univ.Press, Cambridge, 678 pp, 2002.
- [26] H. Akbari and S. Konopacki, Calculating energy-saving potentials of heat-island reduction strategies. *Energy Policy*, 33 (2005) 721–56.

- [27] R. H. Howell, H. J. Sauer, W. J. Coad, Principles of Heating Ventilating and Air conditioning. American Society of Heating, Refrigerating and Air-Conditioning Engineers (ASHRAE), 254 pp, 1998.
- [28] Bornstein, R., B. Lebassi, E. Maurer, P. Switzer, and J. E. Gonzalez, 2009: Cooling summer daytime temperatures in two urban coastal California air basins during 1948–2005: observations and implications. 8th Conf. on Coastal Atmospheric and Oceanic Prediction and Processes, Phoenix, AZ, Amer. Meteor. Soc.
- [29] J. E. Oliver, Encyclopedia of world climatology. Springer, 854 pp, 2005.
- [30] A. Walters, Vegetative Assessment in an Urban Environment, California Water Report Update 2005. [Available online at <http://www.waterplan.water.ca.gov/previous/cwpu2005/index.cfm>]
- [31] Energy Efficiency and Renewable Energy, cited 2009: Residential Consumption of Electricity per Capita per Cooling Degree Day. [Available online at <http://apps1.eere.energy.gov/states/residential.cfm/state=CA#eleccool>.]

Chapter 4

An Improved Three-Dimensional Simulation of the Diurnally Varying Street Canyon Flow

The impact of diurnal variation of temperature distributions over building and ground surfaces on the wind flow and heat transport in street canyons is numerically investigated using the PARallelized LES Model (PALM). Simulations are performed for a 3 by 5 array of buildings with canyon aspect ratio of one in both horizontal directions for two clear summer days that differ in atmospheric instability in Phoenix, Arizona, USA. A detailed building energy model with a 3-D raster-type geometry - Temperature of Urban Facets Indoor-Outdoor Building Energy Simulator (TUF-IOBES) - provides urban surface heat fluxes as thermal boundary conditions for PALM. Compared to the neutral ('no heating') case, non-uniform heating of the urban canyon surfaces significantly modifies pressure field and turbulence statistics in street canyons. Strong horizontal pressure gradients were detected in streamwise and spanwise canyons throughout the daytime which motivate larger turbulent velocity fluctuations in the horizontal directions rather than in the vertical direction. Compared to previous analyses which used uniformly distributed thermal forcing on urban surfaces, the present analysis shows that realistic non-uniform thermal forcing resulting from the effects of sunlit-shaded surfaces and materials with different thermal properties can result in complex local air flow patterns. Canyon-averaged TKE in all non-neutral simulations exhibit a diurnal cycle following the insolation on the ground surface in both spanwise and streamwise canyons and it is larger when the canopy-bottom surface is paved with darker materials and the ground surface temperature is higher as a result. This study shows the importance of three-dimensional simulations with detailed thermal boundary condition to explore the heat and mass transport in an urban area.

4.1 Introduction

Urban microclimate which is affected by urban canyon geometry, weather conditions, anthropogenic heat fluxes, and physical, thermal and radiative properties of materials, directly affects the life of city inhabitants. Effects of microscale meteorological processes in urban canyons on energy use, human health and comfort have motivated many investigations over the past several decades (e.g. [1-13]). Due to the complex flow patterns in the urban roughness layer, lack of accurate information of thermal forcing from urban surfaces and also experimental and numerical limitations for holistically studying the thermal forcing effects on the flow field and heat transport, typically only simplified abstractions of real urban canyons can be investigated. Several numerical (e.g. [14-24]), field measurement (e.g. [25-30]), and laboratory experimental (e.g. [31, 32]) studies investigated air flow, heat and mass transport in the urban roughness layer. Several factors were considered: canyon aspect ratios, canyon/building configurations (e.g. uneven building heights), ambient wind speed, and orientation of the heated surfaces with respect to the wind direction. In most numerical and laboratory experimental studies of the flow field and heat transport in street canyons, thermal forces (which in reality are induced by solar radiation, release of stored heat from construction materials and/or anthropogenic heat fluxes) were prescribed uniformly on canyon surfaces and did not vary with time. However thermal forces from urban street canyon surfaces under solar radiation are spatially and temporally variable according to the thermal and radiative properties of the construction materials (e.g. windows versus wall materials, or bright high-albedo

surfaces versus dark low-albedo surfaces) and also seasonal and diurnal variation of shadow distribution on each surface. The latter depends on the location and geometric characteristics of the built-up area (such as building block densities and street orientations). The lack of accurate numerical investigations of these effects on the wind flow and pollutant dispersion within street canyons and yet their importance has been lamented by various investigators (e.g. [19, 24, 33, 34]). Kwak et al. [34] incorporated urban surface and radiative processes into a CFD model to investigate diurnal variation of a two-dimensional street canyon flow. However, thermal forces at each time were uniformly distributed over each canyon surface. Solazzo and Britter [35] conducted CFD of a two-dimensional urban canyon in which a coherent fraction of the canyon facets were heated (insolated), assuming that the shaded fraction of the canyon was at the same temperature as the ambient flow. However their results showed that the mixing inside the canyon produced a spatially uniform air temperature distribution within the canyon. The literature review shows that despite a long history of valuable urban microclimate studies, comprehensive and dynamic studies of heat transfer and flow in the urban canopy layer are still in preliminary stages.

The objective of this study is to apply the heat flux distribution over each surface of a detailed building energy model as thermal boundary conditions into large-eddy simulation (LES) to provide a more comprehensive and realistic simulation of the diurnally varying street canyon wind flow and associated heat transport. The building energy model and the LES and their simulation setup are described in section 2. In section 3, validation against wind-tunnel experimental data is performed. The

results are presented and discussed in section 4. A summary and conclusions are given in section 5.

4.2 Model description and simulation setup

The PArallelized Large-eddy simulation Model (PALM) developed at the Leibniz University of Hannover [36, 37] is employed in this study. It solves the filtered, incompressible Boussinesq equations, the 1st law of thermodynamics, passive scalar equation and the equation for subgrid-scale (SGS) turbulent kinetic energy (TKE). The SGS turbulent fluxes are parameterized using the 1.5-order Deardorff [38] scheme which uses SGS-TKE to calculate eddy viscosity. A detailed description of PALM can be found in Letzel et al. [37].

In this study thermal fluxes from the solid surfaces in PALM are based on Temperature of Urban Facets Indoor–Outdoor Building Energy Simulator (TUF-IOBES [39]) outputs. TUF-IOBES is a building-to-canopy model that simulates indoor and outdoor building surface temperatures and heat fluxes to estimate cooling/heating loads and energy use of buildings in a three-dimensional urban area. The indoor and outdoor energy balance processes are dynamically coupled taking into account real weather conditions, indoor heat sources, building and urban material properties, composition of the building envelope (e.g. windows, insulation), and HVAC equipment. Further details of TUF-IOBES are described in Yaghoobian and Kleissl [39]. Surfaces in the geometry of TUF-IOBES are subdivided into patches of identical size (of the order of meters; Fig. 4.3). With this raster-type geometry, TUF-

IOBES is capable of simulating temperature and heat flux on the surface of each patch in the domain. Applying the discretely simulated surface temperature/heat fluxes of TUF-IOBES as boundary conditions in PALM makes it possible to simulate the effects of the realistic temperature distribution over urban canopy surfaces (walls, roofs and street) on the flow pattern and heat transport in the canopy. Through coupling of these models the following processes and parameters will be examined: (i) different urban materials (e.g. windows versus walls), (ii) moving shadows in the course of a day, (iii) different ground surface albedo (reflective versus dark ground surface materials), (iv) different stability conditions through variable wind speed.

4.2.1 Model Coupling

One-way coupling is implemented in that surface convective heat fluxes (not the surface temperatures) simulated in TUF-IOBES are used as thermal boundary conditions of all solid surfaces in PALM. While two-way coupling between the flow field in PALM and heat transfer in TUF-IOBES would provide the most realistic surface temperature distribution and fluid flow, radiation effects dominate the heat fluxes (over convection effects) (e.g. [40]) and the complexity of integrating these codes cause us to leave two-way coupling to future work. The surface convective heat fluxes in TUF-IOBES are simulated based on the temperature differences between surfaces and canopy air multiplied by a convective heat transfer coefficient based on an empirical model known as the DOE-2 method [41]. Given the inaccuracy of wall functions for complex flows and thin thermal boundary layers in urban flows this

admittedly simple approach was preferred due to consistency with the TUF-IOBES energy balance; if heat fluxes were dynamically computed in PALM using a wall function method and surface temperatures from TUF-IOBES, they would not be representative of the surface temperatures dynamically simulated in TUF-IOBES using the DOE-2 method.

Since the patch sizes in TUF-IOBES are larger than the resolution of the CFD model, the patch heat flux outputs are interpolated using a high order scheme and PALM is modified to obtain heterogeneous gridded heat fluxes. The patch surface heat fluxes are output every 15 minutes in TUF-IOBES and linearly interpolated to the PALM timestep. This allows simulating the effects of gradual shadow movements and associated surface heat fluxes on the flow and heat transport in the urban canopy.

4.2.2 Simulation setup of TUF-IOBES

Physical building setup and thermal properties of the construction materials are similar to the post-1980 buildings in Yaghoobian and Kleissl [42] which satisfy insulation requirements for nonresidential buildings in ASHRAE 90.1-2004 [43] (Table 1 in Yaghoobian and Kleissl [42]). Buildings have square footprints of 21.3 m on each side and heights of 18.3 m. Each wall of the buildings has a window centered on the wall with dimensions of 12.2 m height \times 15.2 m width resulting in a window fraction of 0.47. Windows are triple-pane clear 1 Low-E layer which were chosen to meet ASHRAE Standard 90.1-99. Detailed description of thermal and radiative properties of the construction materials can be found in section 2 of Yaghoobian and

Kleissl [42]. Simulations were performed for a domain of 5×5 identical building with canopy aspect ratio (building height to the distance between buildings) of 1 in both horizontal directions. Two clear summer days, June 9th with moderate average wind speed of 3.67 m s^{-1} and August 17th with weak average wind speed of 1.8 m s^{-1} were chosen from the TMY3 weather data file of Phoenix Sky Harbor International Airport (33.45° north latitude, 111.983° west longitude and 337 m altitude) in Arizona, US. For each of these days, simulations were performed for canopy ground surface albedo of 0.1 and 0.5 while the building wall albedo was kept constant at 0.3. Based on the American Concrete Pavement Association [44] a ground surface albedo of 0.1 (0.5) is representative of weathered asphalt (white Portland cement concrete). The effects of different ground surface albedo and canopy aspect ratios on ground, outside and inside building surface temperatures, building thermal loads and transmitted shortwave radiation through fenestrations are discussed in detail in Yaghoobian and Kleissl [42]. Generally the temperature of the darker ground surface is significantly higher than the temperature of the brighter surface. However, due to the larger shortwave reflection of the brighter canopy floor, outdoor building wall surface temperatures, transmitted shortwave radiation into the buildings and as a result indoor building wall surface temperatures and cooling loads are larger.

4.2.3 Simulation setup in PALM

Evidence of the correlation between the turbulent flow structure within a cubical canopy and the large organized structures of turbulence within the inertial sub-

layer above (e.g. [45-50]) necessitates a preliminary sensitivity test for choosing the most appropriate computational domain size. In the Inagaki et al. [49] simulation of a daytime atmospheric boundary layer over a large domain of regular array of cubes, the inertial sub-layer formed between $1.5H$ and approximately $6H$ (H is the height of the cubes). The turbulent organized structures within this layer are several times H in the spanwise direction, and more than $10H$ in the streamwise direction [49]. In our sensitivity tests the building setup geometry was chosen identical to the simulations presented later: horizontal dimensions of the buildings are $1.13 H$ and canopy aspect ratio (canopy height divided by the distance between buildings) is 1.0 in both x and y directions. To conduct a sensitivity test, a control simulation was performed for a domain of 10 (in streamwise direction) by 3 (in spanwise direction) buildings which provides a domain size of $21.3H$ (length) \times $6.4H$ (width) \times $5H$ (height). Several simulations with different domain sizes were referenced against the control case and the time and ensemble averaged streamwise velocity profiles of some of them are shown in Fig. 4.1a. Based on comparison of u -velocity profiles and profiles of other velocity components, temperature, SGS-TKE, and velocity variances (not shown) a computational domain of $10.6H$ (length) \times $6.4H$ (width) \times $5H$ (height) (5 by 3 buildings) was found to be sufficiently similar to the largest domain size.

To choose an appropriate computational resolution a grid independency analysis was conducted. For this test three simulations were performed in which the cubical canyons in the domain were resolved by 20, 32, and 40 grids (respectively representative of grid sizes of $0.05H$, $0.03H$, and $0.025H$, Fig. 4.1b). Comparison of vertical profiles of time and ensemble averaged streamwise velocity component in Fig.

4.1b (and other parameters as for the domain size sensitivity test, not shown) shows that a moderate resolution with grid spacing of $0.03H$ is sufficient, thus it was chosen for the computational resolution of the main simulations.

The grid spacing is uniform in the horizontal directions. In the z direction, the grid spacing is uniform up to $z = 3H$ and then gradually increases with an expansion ratio of 1.08. In the horizontal directions boundaries are periodic which result in an infinite homogeneous urban surface boundary. A zero-gradient (free-slip) boundary condition is used at the top boundary which has similar effects as a strong inversion [51]. Coriolis forces are not considered.

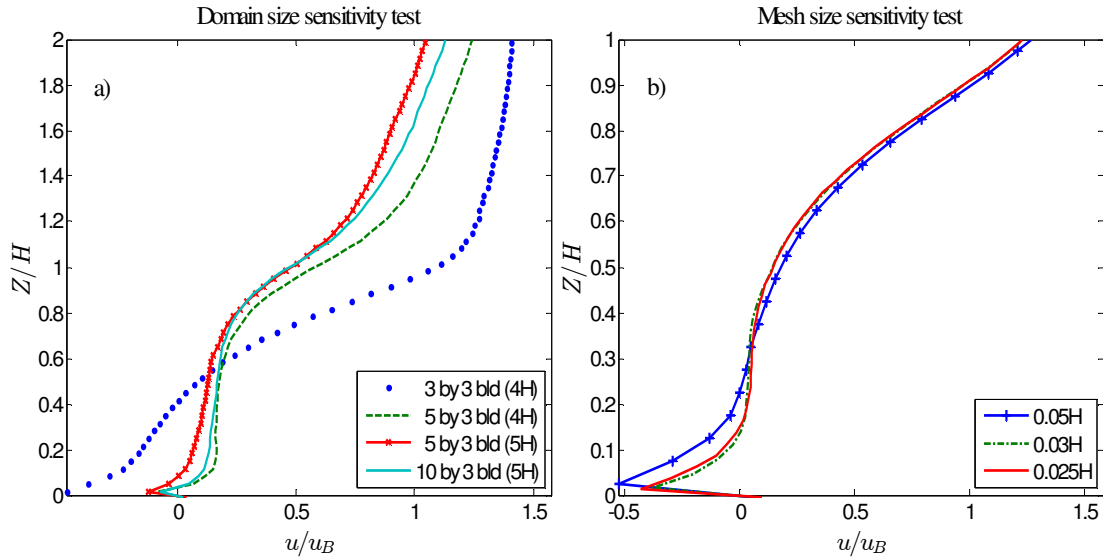


FIG. 4.1 Comparison of vertical profiles of ensemble and time averaged (over the last hour of 6 hour simulations) streamwise velocity normalized by initial bulk velocity at the center of a spanwise canyon in sensitivity tests for a) computational domain and b) mesh size.

A suite of simulations was conducted (Table 1). Since the thermal boundary conditions are from the TUF-IOBES simulations of June 9th and August 17th in Phoenix, AZ, the initial ambient bulk wind velocity in the PALM simulations is set to the average wind speed of these days from TMY3 weather data for Phoenix, AZ (3.67 m s^{-1} and 1.8 m s^{-1} , respectively). Temperature results are very sensitive to the temperature boundary condition at the top of the domain. Several tests showed that if the TMY3 mean air temperature between 0300 and 2000 LST (the time period that was chosen for the PALM simulation; see below) was used as upper boundary condition, the hourly average canopy air temperature was equal to (with a margin of 2-3 °C) the simulated canopy air temperature in the TUF-IOBES simulations throughout the day. Therefore at the top of the domain the temperature is set to 31.7 °C and 33.2 °C for June 9th and August 17th, respectively. Surface heat flux boundary conditions were based on the TUF-IOBES simulations for ground surfaces albedos of 0.1 and 0.5. In addition, August 17th with ground surface albedo of 0.1 was also simulated with zero wind velocity as a free-convection control simulation.

Since nighttime surface temperatures are more homogeneous in the canopy we focus on the daytime. Each of these 5 simulations was performed from 0300 to 2000 LST in which the first 6 hours were considered as the spin up period. Simulation outputs were averaged over consecutive 1800 s intervals. For reference, neutrally stratified simulations (i.e. the surface temperatures at the street, wall and roof are the same as the (homogeneous) air temperature) were performed with initial bulk wind velocities of 1.8 m s^{-1} (August 17th) and 3.67 m s^{-1} (June 9th). Each of these neutral simulations was conducted for 7 hours and the last 1800 s were used for analysis. For

TABLE 4.1 Stratification, ground surface albedo, and wind speed in the August 17th and June 9th PALM simulations.

Day	Stratification	Canopy floor albedo [-]	Wind speed (m s ⁻¹)
Aug 17 th	Unstable	0.1	1.8
Aug 17 th	Unstable	0.5	1.8
Aug 17 th	Unstable	0.1	0.0
Aug 17 th	Unstable (with uniform surface heat fluxes)	0.1	1.8
Aug 17 th	Neutral	-	1.8
Jun 9 th	Unstable	0.1	3.67
Jun 9 th	Unstable	0.5	3.67
Jun 9 th	Neutral	-	3.67

neutral conditions 1800 s corresponds to at least 12 eddy turnover times of the primary circulation in the canyon, $t_c = H/U_c$, where H is the canyon height and U_c is the mean scalar wind speed in the canyon.

4.3 Validation

TUF-IOBES validation is described in Yaghoobian and Kleissl [39]. In Park et al. [22] the velocity and temperature fields of PALM in a bottom-heated street canyon are validated against the wind-tunnel data of Uehara et al. [31]. In this study PALM is validated against the wind-tunnel experiment of Kovar-Panskus et al. [32] for a case with heated windward wall. One of the limitations for numerically replicating the wind-tunnel experiment of Kovar-Panskus et al. [32] is that in PALM the wind and temperature boundary conditions are cyclic which mimic the effects of an infinite number of identical street canyons on the flow characteristics. On the other hand, the

wind tunnel experiment is composed of a single 2D canyon. In PALM a domain with $6H$ length (H is the height of the canopy) in the streamwise direction is chosen with a 2D canyon in the center of the domain. This provides an effective streamwise empty space of $5H$ upstream of the canyon. The canyon aspect ratio (height to width) is 1.0.

Similar to the wind-tunnel experiment, in the LES simulation Re is of $O(10^4)$ [Note that a similar validation study of the Cai [24] LES model did not match the Reynolds number in the experiment; rather Cai [24] assumed that $Re \sim 10^4 - 10^6$ is generally large so that the flow is independent of Re . Our validation for the neutral case showed a significant difference in mean flow field between the LES results for $Re \sim 10^6$ and the wind tunnel experiment (not shown).].

Different surface heat fluxes were prescribed at the wind-ward wall to vary the Froude number, $Fr = U_{ref}^2 / (gH(T_{wall} - T_{ref})/T_{ref})$, where H is the canyon height, g is the acceleration due to gravity, T_{wall} is the wall surface temperature, and U_{ref} and T_{ref} are the ambient, free-stream wind velocity and temperature. To calculate T_{wall} , the sensible heat flux equation ($Q_h = h [T_{wall} - T_{air}]$) was used in which Q_h is the prescribed wall heat flux, h is the convection heat transfer coefficient simulated based on the DOE-2 method (the empirical method that is used in TUF-IOBES), and T_{air} is the simulated air temperature at the first grid point near the wind-ward surface. To calculate h , the volumetric mean wind velocity magnitude and mean air temperature inside the canopy simulated in PALM were used as environmental wind speed and air temperature in the DOE-2 method (the DOE-2 formulation is too lengthy to be fully reproduced here; see [41, 52] for details). The Fr number and mean canopy flow field

were compared against the wind tunnel experiment. While the DOE-2 method is not commonly applied to determine T_{wall} , it is consistent with how convective fluxes are obtained in TUF-IOBES. Therefore the validation extends beyond testing PALM also to the coupling with TUF-IOBES.

Fig. 4.2a and 4.2b show mean velocity vectors of the LES simulation side-by-side with the wind-tunnel experiment of Kovar-Panskus et al. [32] for $Fr = 0.73$. The location of all three vortices at the top, bottom left and bottom right of the canyon in the PALM simulation are comparable with those in the wind-tunnel experiment. Fig. 4.2c and 4.2d represents the LES and wind-tunnel results for $Fr = 1.17$. Again, the features of the flow are very similar in these two figures. For example the velocity vectors at the top of the canopy show the same pattern without updraft despite the heated wall. Also the size of the vectors in the LES and the wind-tunnel results shows that the downward wind speed near the windward wall is much larger than the upward wind near the leeward wall. In addition the location of the secondary vortex in the bottom right of the canopy is at the same height from the canopy floor. Similarly as in the validation results of Cai [24] the primary vortex is shifted to the right (Fig. 7a in Cai [24]) which differs from the location of the ‘sketched’ primary vortex in the experimental results. We believe this to be due to measurement error in the experiment. The shape and magnitude of the mean velocity vectors which are similar in both Figs. 4.2c and 4.2d suggest that based on mass conservation (downward mass flux into the canyon near the windward wall = upward mass flux out of the canyon near the leeward wall) the primary vortex should be shifted to the right as in the LES results of Cai [24] and PALM. As argued by Cai [24] the flow pattern in the

experiment results can only be explained by either an undetected strong updraft near the leeward wall or a mass divergence along the canyon axis. Neither feature was discussed by Kovar-Panskus et al. [32] and this aspect of the experimental results remains questionable. Overall the validation can be considered to be successful.

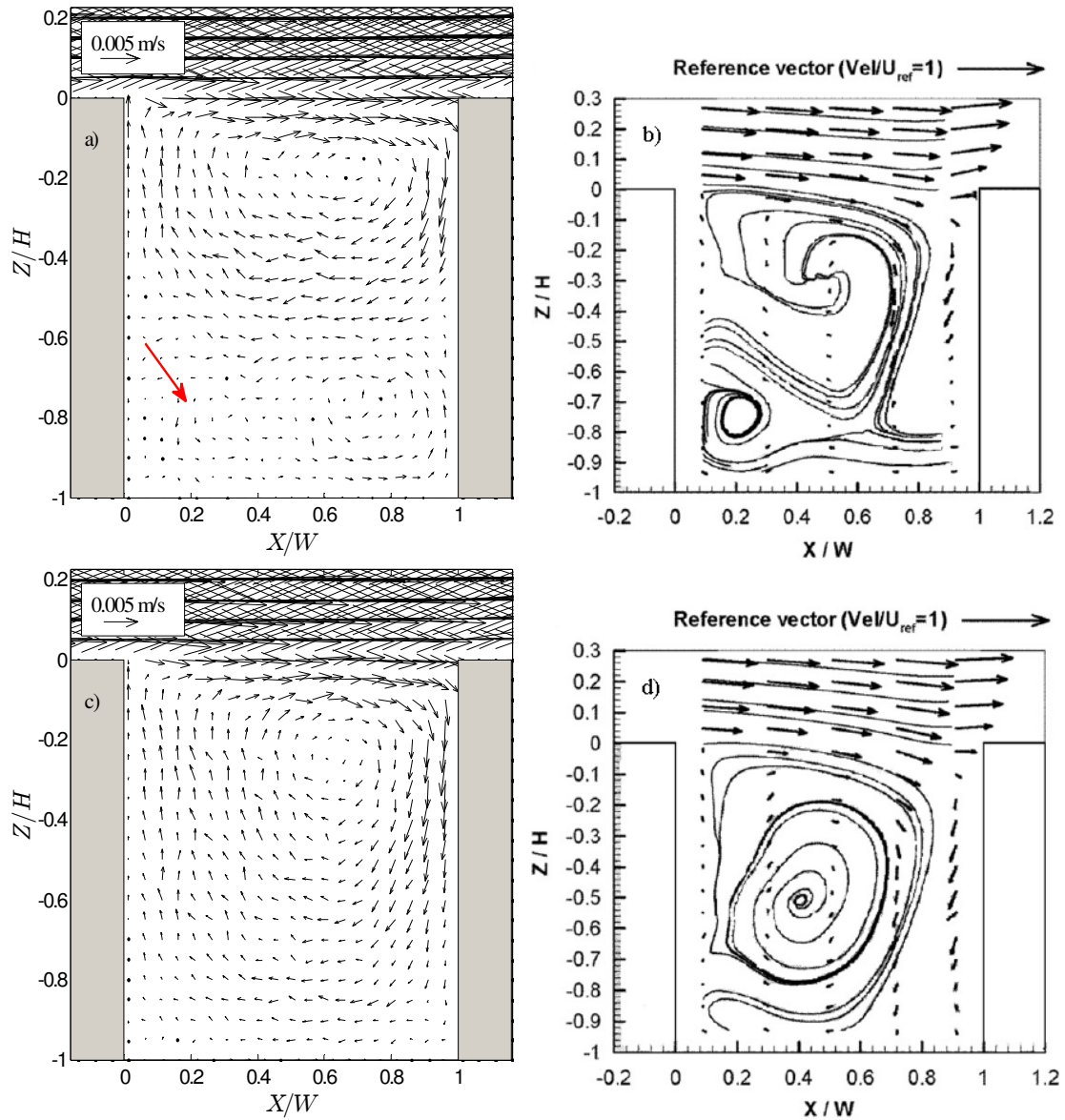


FIG. 4.2 Simulated mean wind field in PALM with $Fr =$ a) 0.73 and c) 1.17, and mean velocity vectors and streamlines of Kovar-Panskus et al. [32] for cases with $Fr =$ b) 0.73 and d) 1.17. The windward (right) wall is heated. The red arrow in (a) shows the location of the bottom left vortex.

4.4 Results and discussion

Since this study is about investigating the effects of diurnal street-bottom and building-surface heating on flow and heat transport in three-dimensional street canyons, it is necessary to consider both spanwise (north-south oriented) and streamwise (east-west oriented) canyons in explaining the results. Unless stated otherwise, all results are time-averaged over 1800s and ensemble-averaged over the canopies in the domain (all spanwise (streamwise) canyons are used for calculating the ensemble-averaged spanwise (streamwise) canyon). Fig. 4.3 shows surface temperature in the TUF-IOBES simulation domain at 1015, 1315, 1615, and 1915 LST of August 17th in Phoenix, AZ when the ground surface albedo is 0.1. Fig. 4.3

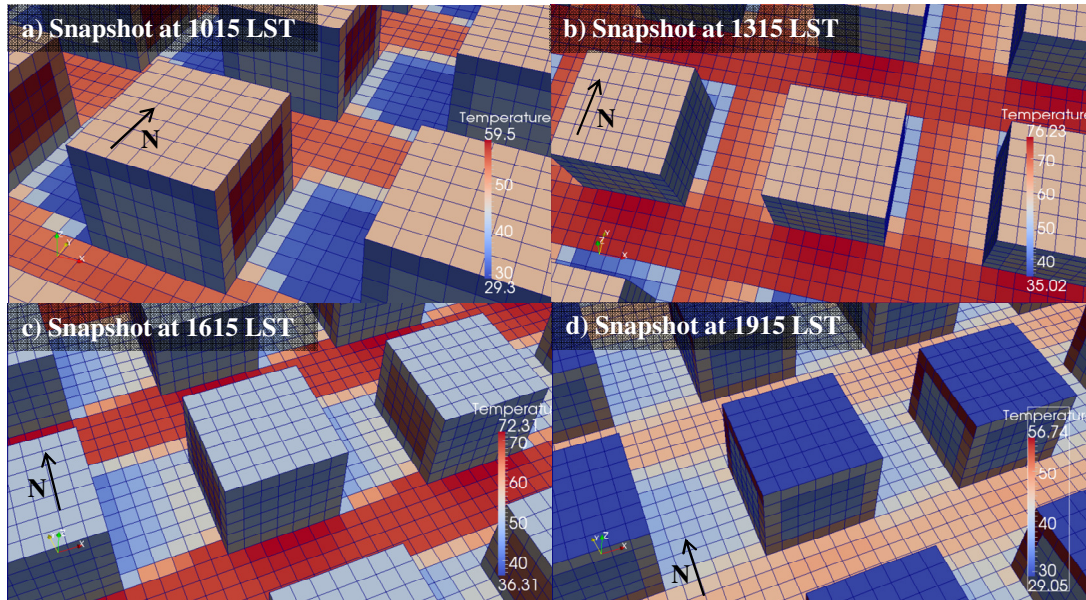


FIG. 4.3 Surface temperature in the TUF-IOBES simulation domain at a) 1015 b) 1315 c) 1615 d) 1915 LST of the August 17th simulation with ground surface albedo of 0.1 in Phoenix, AZ (the base case simulation). The length of each patch is 3.05 m and the center 4×5 patches of each facet are windows. The direction of the flow is from west to east.

illustrates the dynamic thermal forcing that will later be shown to cause variation of flow in urban canopies.

4.4.1 Mean flow and temperature field

Fig. 4.4 shows the spatial distribution of the time and ensemble averaged velocity vectors and temperature in vertical and horizontal cross sections in the middle of the spanwise canyon of the August 17th simulation with ground surface albedo of 0.1 which we chose as the base case. These half hour time-averaged velocity and temperature fields are from four different times of day, late morning (1000 – 1030 LST), early afternoon (1300 – 1330 LST), late afternoon (1600 – 1630 LST) and early evening (1900 – 1930 LST). Due to the large solar altitude and the east-west orientation of the streamwise canyon most of the ground surface in the streamwise canyons (which are located between north and south facing walls) receives direct solar radiation throughout the day; only the north facing walls are shadowed (Fig. 4.3). Therefore velocity and temperature fields for the streamwise canyons are not shown since the relative thermal forcing from the streamwise canyon surfaces does not change significantly throughout the day; the ground is the warmest surface while the north facing wall is the coolest surface.

Fig. 4.4 shows velocity vectors and temperature in a vertical cross section at $Y/H = 0.5$ (left column) and a horizontal cross section at $Z/H = 0.5$ (right column). The ensemble mean velocity vectors in the vertical cross section show a dominant canyon vortex centered at a constant height (around $Z/H = 0.75$) throughout the day. The

persistent location and speed of the canyon vortex suggests that the mechanical force and the horizontal streamwise thermal force induced by the temperature (and as a result pressure) difference between the air right above the roof surfaces and above the spanwise canyon outweigh the thermal forces from the heated surfaces inside the canyon in defining the general flow pattern in the spanwise canyon. For instance, thermal forces from the heated downwind wall in the late afternoon and early evening are not enough to produce an updraft to reverse the clockwise canyon vortex. These findings are consistent with observation of previous atmospheric (e.g. [26, 28, 29]) and wind tunnel (e.g. [53]) experiments. Quantitatively, the thermal forces from the heated building walls (and also roofs) strengthen the mechanically induced vortex throughout the day compared to the neutral simulation with bulk wind velocity of 1.8 m s^{-1} (not shown here). Similar to Nakamura and Oke [25] a gradient Richardson number ($Ri = (g/T_H)((T_H - T_{Ground})/H)(u_H/H)^{-2}$) is defined for the spanwise canyon in which T_H and u_H are mean canyon temperature and horizontal wind speed at the roof level, T_{Ground} is the temperature of air averaged over the closest grid points to the ground surface in the spanwise canyon, g is the gravitational acceleration, and H is the canyon height. Gradient Ri is calculated from the ensemble and time averaged (over 1800 s) outputs in the spanwise canyon and it is equal to 0.37, -1.58, -0.73, and -0.33 respectively at 1015, 1315, 1615, and 1915 LST.

Two counter rotating vortices are visible throughout the day in the horizontal cross section in the middle of the spanwise canyon. Due to uneven thermal forcing caused by the partially shaded surfaces in the canyon and temperature difference

between windows and the building walls these vortices are not symmetric. Heat from the south facing walls, which are warmer throughout the day, is advected to the southern part of the spanwise canyon. This may explain the growth of the southern vortex in the spanwise canyon from morning to the evening compared to the northern vortex. The non-uniform thermal forcing of the wall surfaces is most noticeable in the XY -plane in the evening (between 1900 and 1930 LST; Fig. 4.4h). Due to high pressure air adjacent to the cooler window surface in the center of the west facing wall and low pressure air near the southern building edges the center of the southern vortex moves to the south-east part of the spanwise canyon.

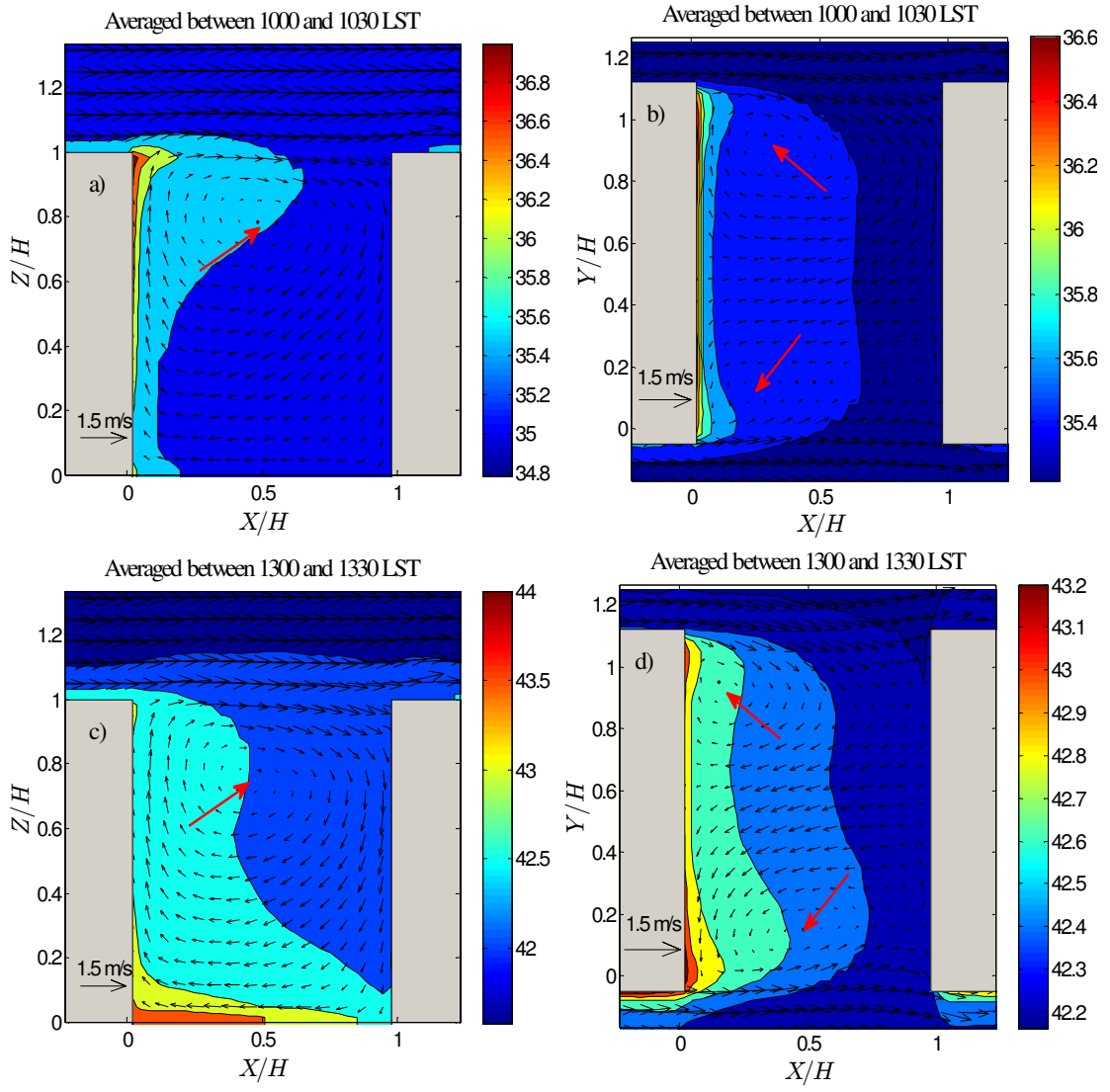


FIG. 4.4 Ensemble and time averaged velocity vectors and temperature field in vertical (left panel) and horizontal (right panel) cross sections in the middle of the spanwise canyon of the base case simulation. The red arrows point to vortex centers.

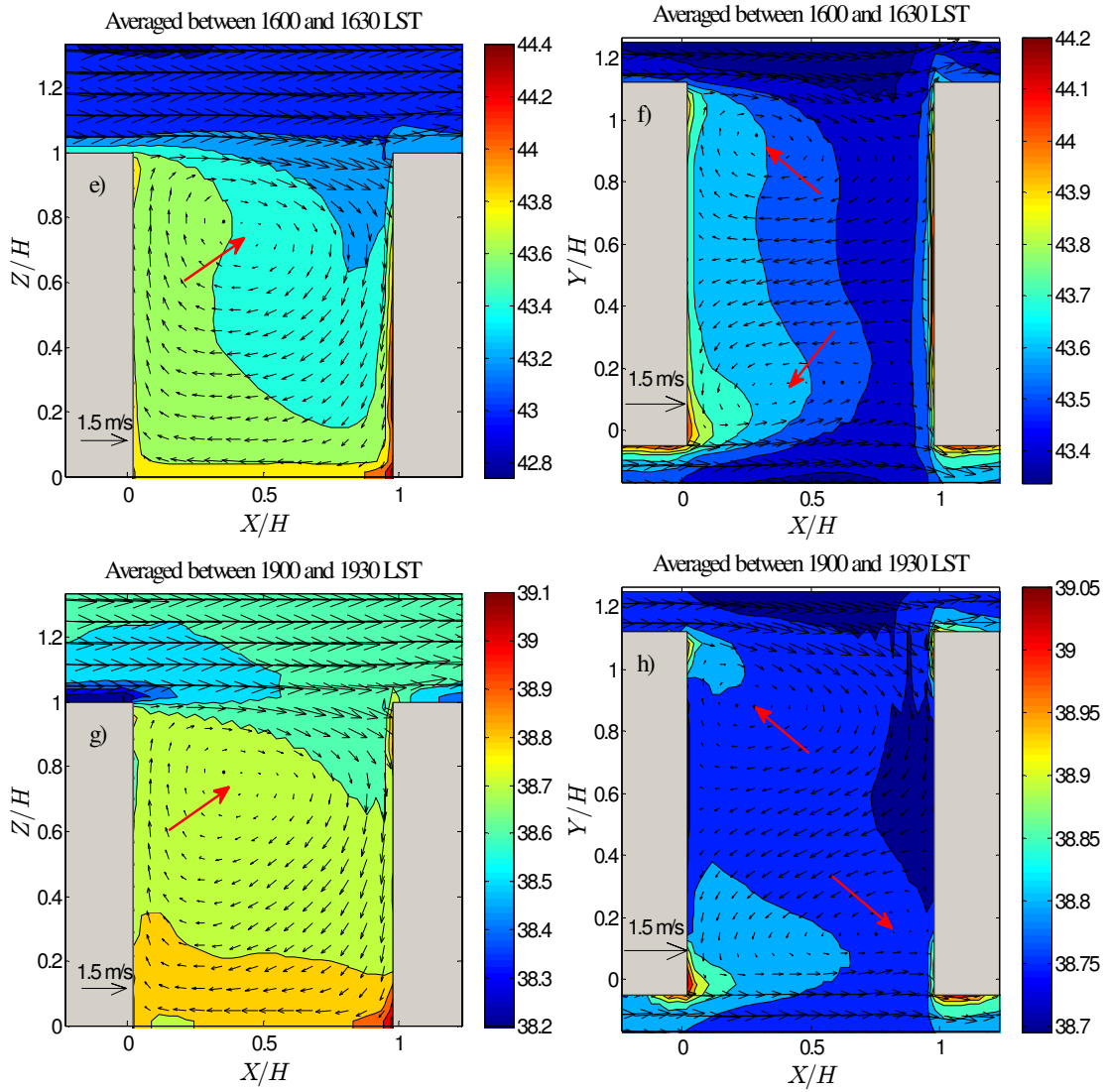


FIG. 4.4 Continued.

4.4.2 Turbulent kinetic energy and turbulent fluxes

Fig. 4.5 shows the vertical profiles of TKE, streamwise and spanwise horizontal velocity variances, $\overline{u'^2}$ and $\overline{v'^2}$, and vertical velocity variance, $\overline{w'^2}$, from the center of the spanwise canyon for different times of day. u' , v' and w' are the velocity fluctuations obtained from a Reynolds decomposition of the filtered velocities (i.e.

$u' = \bar{u} - \langle \bar{u} \rangle$). The SGS contributions are ignored due to their small amounts. The base case (August 17th with ground surface albedo of 0.1) is compared to the neutral (no heating) case with identical wind forcing. Besides ensemble and time averaging which were explained earlier, 9 (3x3) grid points in the center of the canyon (rather than only one grid point) are averaged at each height to obtain the profiles. To show relative contributions to the local TKE, the variances are normalized by 2 times the local TKE.

As evident in Fig 4.5a and consistent with previous studies (e.g. [22, 24]), in *spanwise* canyons in both neutral and non-neutral cases TKE peaks at the roof height due to TKE production in the shear layer between the air and the roof surface, which is generated from a separation of the flow from the edge of the upstream building [50].

Thermal forces modify the TKE in and above the canopies. As expected TKE increases and decreases with rise (morning to noon) and fall (noon to evening) of the thermal forcing (surface heat fluxes) during the course of the day. At 1915 LST, TKE at the rooftop is less than that in the neutral case because stable conditions above the roof surface (which cools radiatively at this time, Fig. 4.3d) counteract the mechanical production of TKE. On the contrary, deeper inside the canopy where conditions are still unstable as the surfaces are still warmer than air due to the radiation trapping effect, TKE is larger than that of the neutral case.

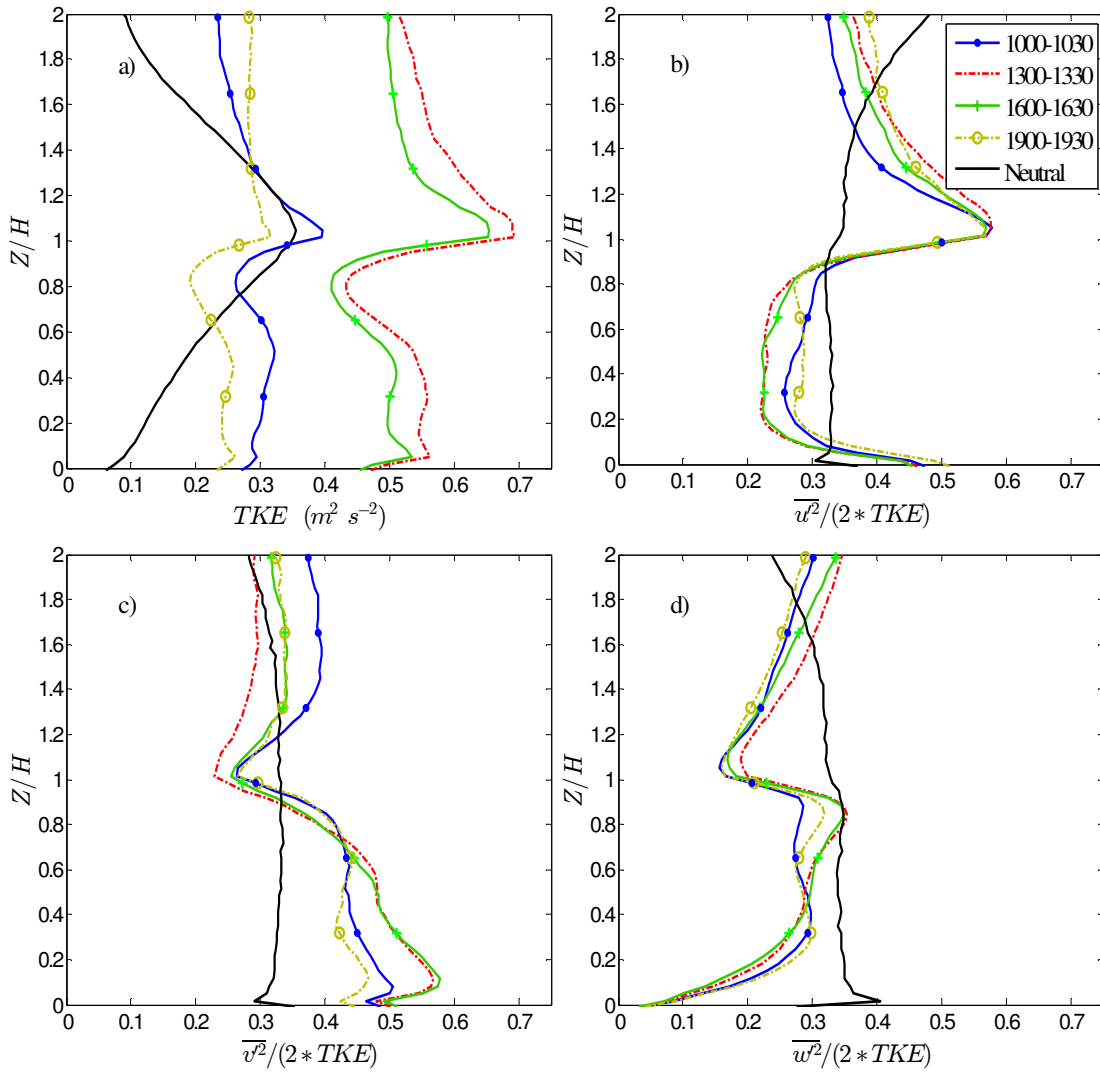


FIG. 4.5 Vertical profiles of a) TKE and relative contributions from b) streamwise horizontal, c) spanwise horizontal, and d) vertical velocity variances from the center of the *spanwise* canyon of the base case and neutral simulations. The variances are normalized by 2 times the local TKE. See the text for the averaging details.

Unlike the neutral case, profiles of TKE at different times of day in the non-neutral case have secondary peaks inside the street canyon. For instance at 1015 LST when the location of the warmest surface (corresponding to the location of more buoyant TKE production) is at the upper two-third of the east facing window (Fig. 4.3a) the TKE secondary peak shifts towards the upper part of the canyon. On the

other hand, early in the afternoon (between 1300 and 1330 LST) when the warmest surface in the canopy is the ground surface, buoyant productions peak close to the canyon floor resulting in a secondary peak. This illustrates that the location of the TKE secondary peak in the middle of the canyon is related to non-uniform thermal forcing in the canyons due to partially shaded surfaces and windows with different thermal properties than walls.

Figures 4.5b-d show the contribution of the horizontal and vertical velocity variances to the TKE in the center of the spanwise canyon. In the neutral case the flow is more isotropic, i.e. all velocity variances equally contribute to the total TKE. On the other hand in the non-neutral simulations, the flow becomes strongly anisotropic.

To investigate the forcing responsible for this strongly anisotropic behavior of the flow we examine the pressure field in vertical cross sections in the center of the canyons. Generally pressure and velocity fields are dynamically linked (Bernoulli's equation), but heat flux from the canyon surfaces also modifies the pressure field by changing the density of the air which creates strong anisotropy in the flow. Fig. 4.6 shows the mean hydrodynamic (perturbation) pressure field ensemble and time averaged between 1600-1630 LST in x - z and y - z -cross sections in the middle of the spanwise canyon in neutral and non-neutral simulations.

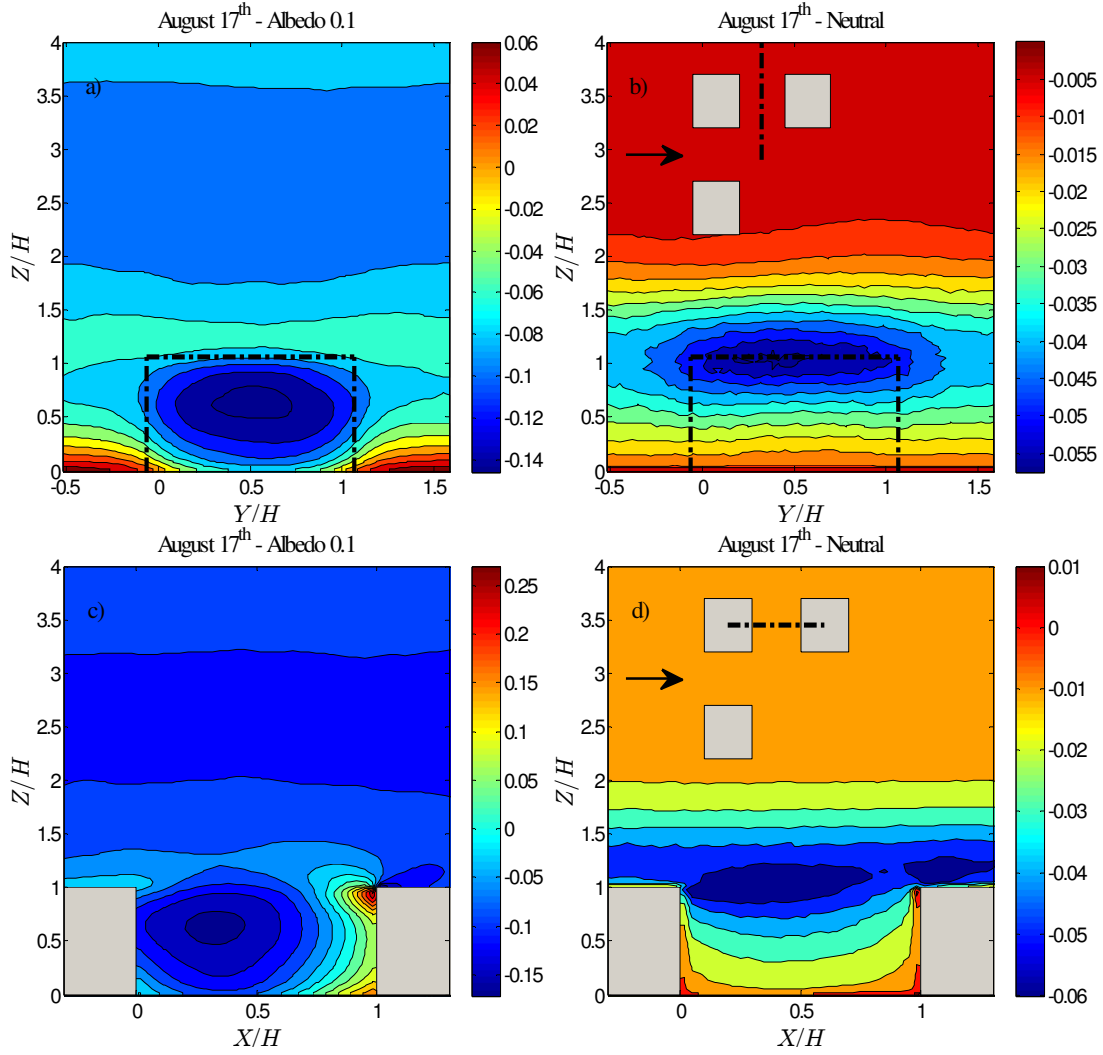


FIG. 4.6 Ensemble and time averaged mean hydrodynamic pressure field at 1600-1630 LST in a, b) y - z and c, d) x - z -cross sections in the center of the spanwise canyon of the base case and neutral simulations. Refer to Fig. 4.3c for the surface temperatures for the base case at 1615 LST. Sketches of the buildings in (b) and (d) are in the x - y plane and they respectively show the locations of the y - z and x - z cross sections in the center of the spanwise canyon.

Figs 4.6a elucidates why the spanwise velocity variance, $\overline{v'^2}$, is the main contributor to the TKE in the spanwise canyon. In the neutral case isosurfaces of mean pressure are aligned parallel to the ground surface (Fig. 4.6b) decreasing from the canyon floor (smallest velocity) uniformly up to the building height. At $Z = H$ the airflow separates at the upwind building edge and generates a boundary layer above

the building roofs extending over the street canyon. Away from the roof surface the velocity converges to the bulk velocity consequently mean pressure increases gradually.

In the non-neutral simulation the heat flux from the surfaces modifies the classical pressure field in the skimming flow pattern of the neutral simulation (Figs 4.6a and c). Generally because of stronger (thermally-driven) circulation and the warm air inside the spanwise canyon (see the temperature field in the horizontal cross sections of the spanwise canyon in Fig. 4.4), the low pressure area expands deeper inside the spanwise street canyon (Fig. 4.6a and c). Advection and vertical mixing cools the air over the street intersections. Consequently the air in these areas (the intersection of the streets) is cooler than the air inside the spanwise canyon. This creates a large horizontal pressure gradient in the spanwise (y-) direction (Fig. 4.6a). That is the main reason for the large contribution of $\overline{v'^2}$ to the TKE in the spanwise canyons (Fig. 4.5c), which is enhanced near the ground where the largest spanwise horizontal pressure gradient exists (Fig. 4.6a).

On the other hand, the air temperature right above the roof surfaces (which are continuously exposed to the sun during the day and cool radiatively at night) is significantly different than the air temperature at the same height over the top of the street canopies. This temperature difference generates horizontal pressure gradients in the non-neutral simulations (Fig. 4.6a and c). Consistent with the magnitude of horizontal temperature differences (around 0.4 °C difference, on average), the streamwise horizontal pressure gradient at the roof level is larger than the spanwise

horizontal pressure gradient at this height. . Consequently, at the roof height in the non-neutral simulations, the streamwise velocity variance, $\overline{u'^2}$, contributes more to TKE (around 60% of the total) than in the canopy. Although the amount of TKE in the spanwise canyon varies at different times of day (Fig 4.5a), the relative contributions of the velocity variances to the total TKE does not change significantly with time (Figs 4.5b-d). The reason is that the flow pattern in these canyons is mainly controlled by horizontal pressure differences (resulting from air temperature differences in the horizontal directions) which are relatively steady throughout the day. Minor differences can be detected for more buoyant flows (at 1315 and 1615 LST) when the v -velocity contribution is enhanced near the surface and the w -velocity contribution is enhanced near the canopy top.

Fig. 4.7 is the same as Fig. 4.5 but for the east-west oriented (streamwise) street canyon. In this canyon the larger TKE at the roof level of the neutral case is related to the shear layer and vortex shedding by the edges of the buildings on the edges of the canyon. Thermal forces significantly increase TKE and anisotropy in the streamwise canyons. TKE increases continuously from 1015 to 1615 LST. At 1915 LST TKE inside the street canyon decreases but – unlike for the spanwise canyon - remains larger than in the neutral case since the release of heat storage and trapping of longwave radiation delays cooling of the canyon surfaces.

The contributions of the velocity variances to the TKE of the streamwise canyon (Figs 4.7b-d) differ from that of the spanwise canyon (Figs 4.5b-d). $\overline{v'^2}$

contributes less than in the neutral case and $\overline{u'^2}$ contributes the most to TKE below roof level (50-60%).

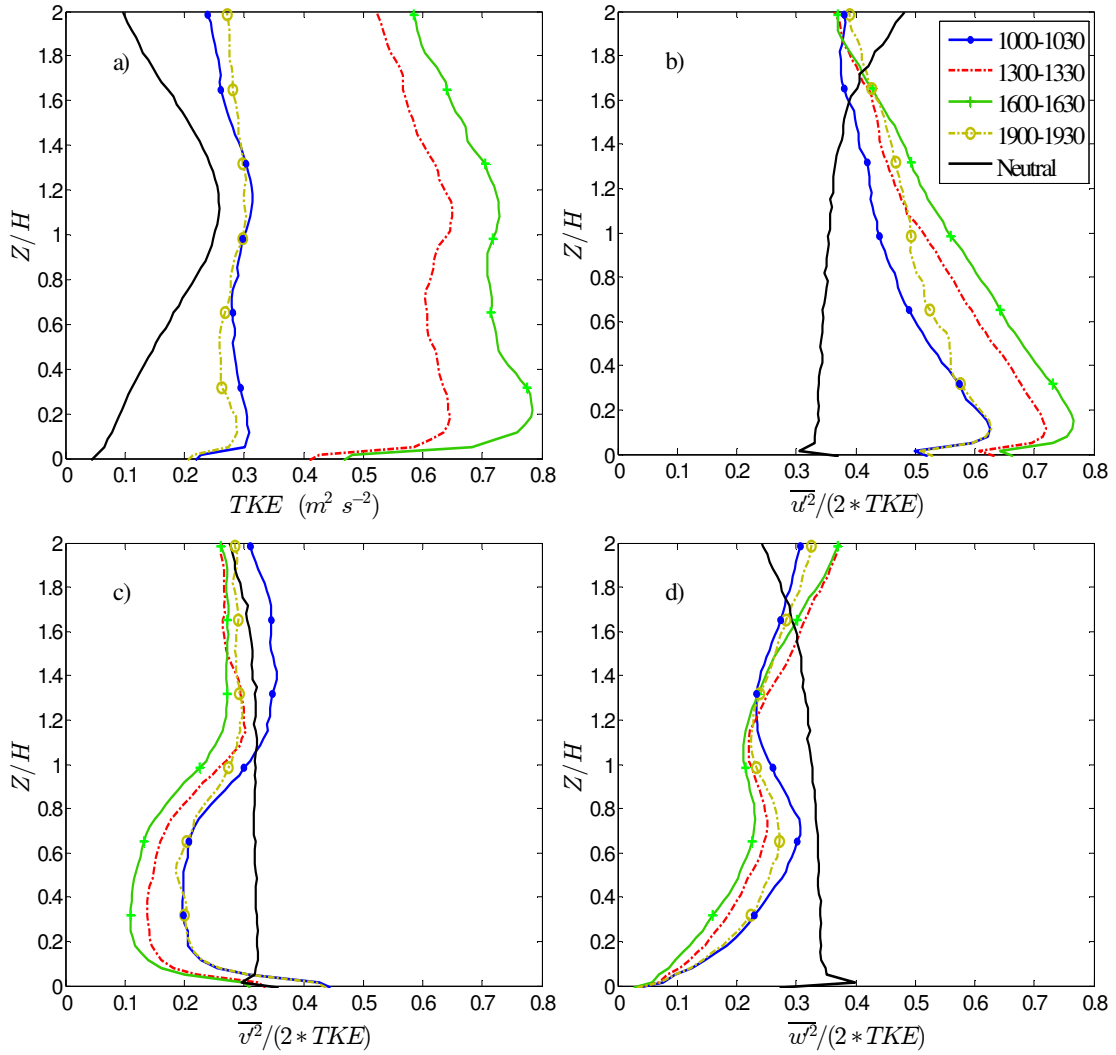


FIG. 4.7 Vertical profiles of a) TKE, and relative contributions from b) streamwise horizontal, c) spanwise horizontal, and d) vertical velocity variances from the center of the *streamwise* canyon of the base case and neutral simulations. The variances are normalized by 2 times the local TKE. See the text for the averaging details.

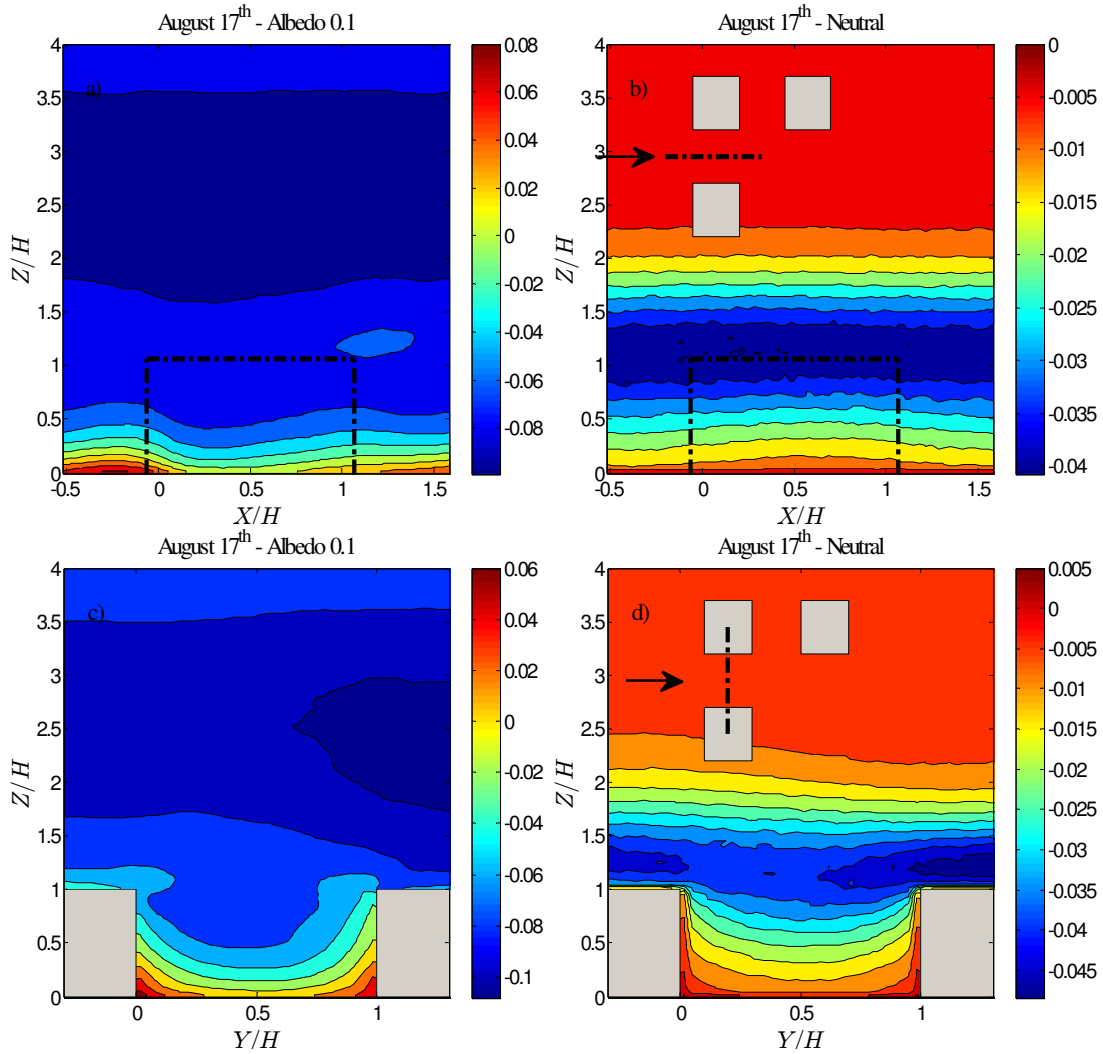


FIG. 4.8 Ensemble and time averaged mean hydrodynamic pressure field at 1600-1630 LST in a, b) x-z and c, d) y-z-cross sections in the center of the streamwise canyon of the base case and neutral simulations. Refer to Fig. 4.3c for the surface temperatures for the base case at 1615 LST. Sketches of the buildings in (b) and (d) are in the x-y plane and they respectively show the locations of the x-z and y-z cross sections in the center of the streamwise canyon.

Fig. 4.8 is similar to Fig. 4.6 but for the streamwise canyon. The larger contribution of the streamwise velocity variance to the TKE in the non-neutral simulation is related to the larger streamwise pressure gradient (see Fig. 4.8a) induced by the temperature difference between the area in between the north and south facing walls and the cooler area over the intersection of the streets. Comparing Fig. 4.8a with

8b shows how strongly thermal forcing modifies the isotropy of the flow compared to the neutral simulation. The contribution of $\overline{u'^2}$ to the TKE varies noticeably with time of the day, much more so than in the spanwise canopies.

Generally in both stream and spanwise canyons the relative contribution of the vertical velocity variance to the TKE is less than for the neutral case. It shows that thermal forcing in an urban area can result in more horizontal fluctuations of the flow than the vertical buoyant movements. While this seems counterintuitive, the pressure analysis supports the findings from the TKE profiles.

Figure 4.9a and b (4.9c and d) show the vertical profile of turbulent momentum (heat) fluxes, $\overline{u'w'}$ ($\overline{w'\theta'}$), for the spanwise and streamwise canyons, respectively. Temporal and spatial averaging of these profiles are similar to those of TKE and velocity variances in Figs. 4.5 and 4.7. In the spanwise canyon, magnitudes of $\overline{u'w'}$ at different times of day in the non-neutral simulation are up to 20 times those in the neutral case and peak at the rooftop level. Shear always causes large negative (downward) $\overline{u'w'}$ at $Z = H$, but the enhancement over neutral can be explained by the enhanced streamwise horizontal velocity right above the roof surface due to the large streamwise horizontal pressure gradient at this location (Fig. 4.6c). The turbulent momentum flux, $\overline{u'w'}$, follows the diurnal cycle of surface thermal forcing increasing gradually from 1015 to 1315 LST and decreasing later at 1615 and 1915 LST. The turbulent momentum flux becomes positive (upward) below about $0.6 H$ because the spanwise canyon vortex which is strengthened in the non-neutral case causes a decrease in velocity magnitude with height.

Since there is no circulation in the streamwise canyons, the sign of the turbulent momentum flux is consistent (negative) at all heights but its magnitude varies with the magnitude of thermal forcing.

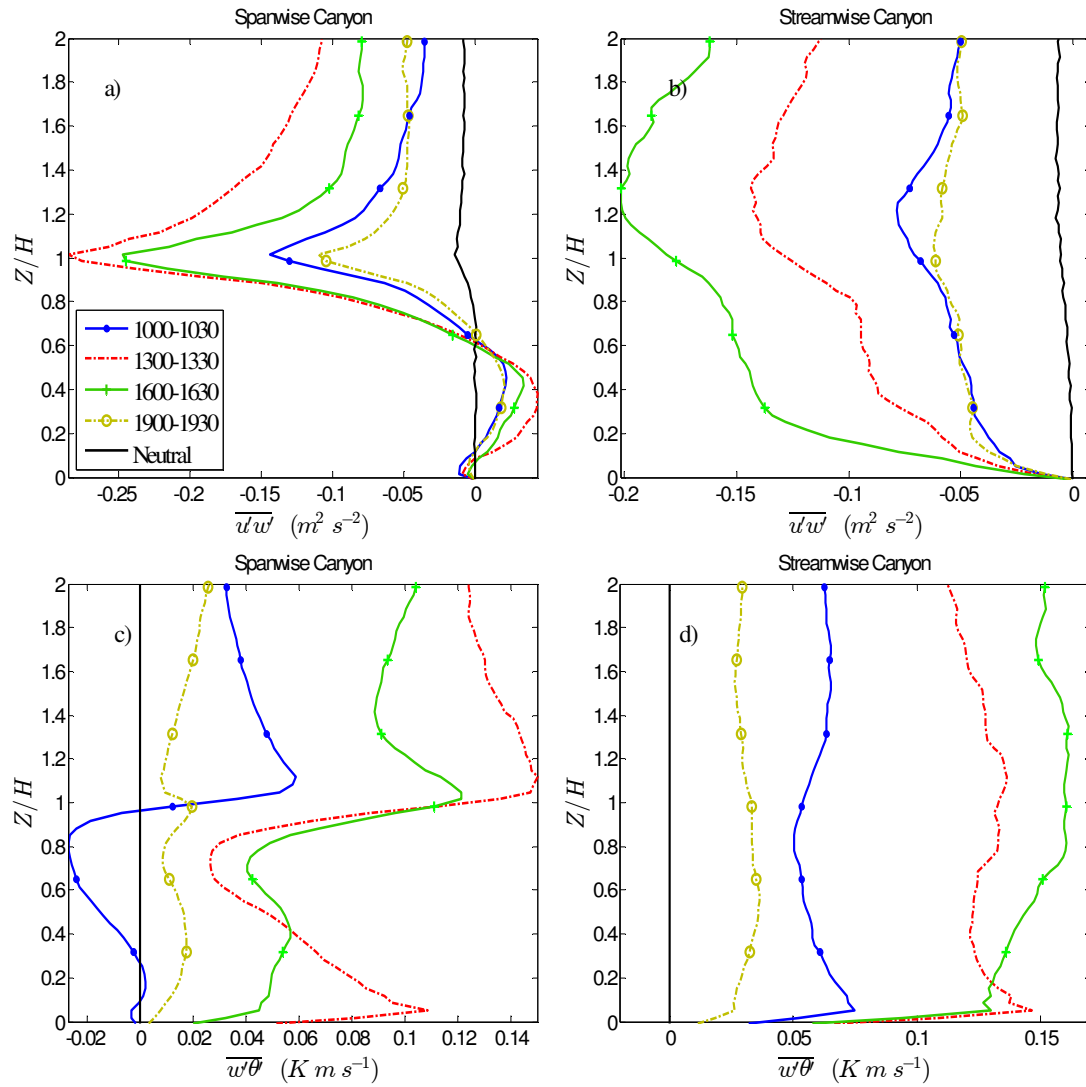


FIG. 4.9 Vertical profiles of turbulent horizontal momentum and heat fluxes from the center of the spanwise (left column) and streamwise (right column) canyons of the base case simulation. See the text for the averaging details.

Due to the larger TKE, large roof surface heat flux and also air temperature gradient between inside and above canopy, the vertical heat flux ($\overline{w'\theta'}$) profiles in the center of the spanwise canopy peaks at roof level. Especially at roof height, the magnitude of the turbulent heat flux follows the diurnal cycle of the ground and roof surface heat flux throughout the day. The large secondary peak near the ground in the 1315 profile of the spanwise canyon is related to the large surface heat flux at this time, while large areas of the ground are shaded at 1015 and 1615 LST. Unlike the spanwise canyons, the turbulent heat flux profiles in the streamwise canyons are more uniform from the ground to the top of the domain.

4.4.3 Non-uniform thermal forcing of the canyon surfaces throughout the day (effects of sunlit-shaded surfaces and different material thermal properties)

To investigate effects of non-uniform thermal forcing of the canyon surfaces due to existence of partially shaded surfaces and windows with different thermal properties on the walls we contrast those results against a case with uniform surface heat fluxes. In this additional simulation the heat flux of each surface is defined as the average heat flux of all the patches on the surface, time-averaged between 1700 and 1730 LST of the base case (hereinafter this simulation is referred to as ‘uniform thermal forcing simulation’). The ensemble and time averaged (over 1800 s) air temperature, hydrodynamic pressure and velocity magnitude outputs of the base case simulation from the time period between 1700 and 1730 LST are compared to those of

the uniform thermal forcing simulation in a vertical and a horizontal cross section in the center of the spanwise canyon (Fig. 4.11). Fig. 4.10 shows a snapshot of surface temperatures at 1715 LST from the TUF-IOBES simulation of August 17th in Phoenix, AZ with ground surface albedo of 0.1 (base case). Due to partial shading of the building walls and the near perpendicular solar incidence, this time period shows the largest within-surface temperature heterogeneity.

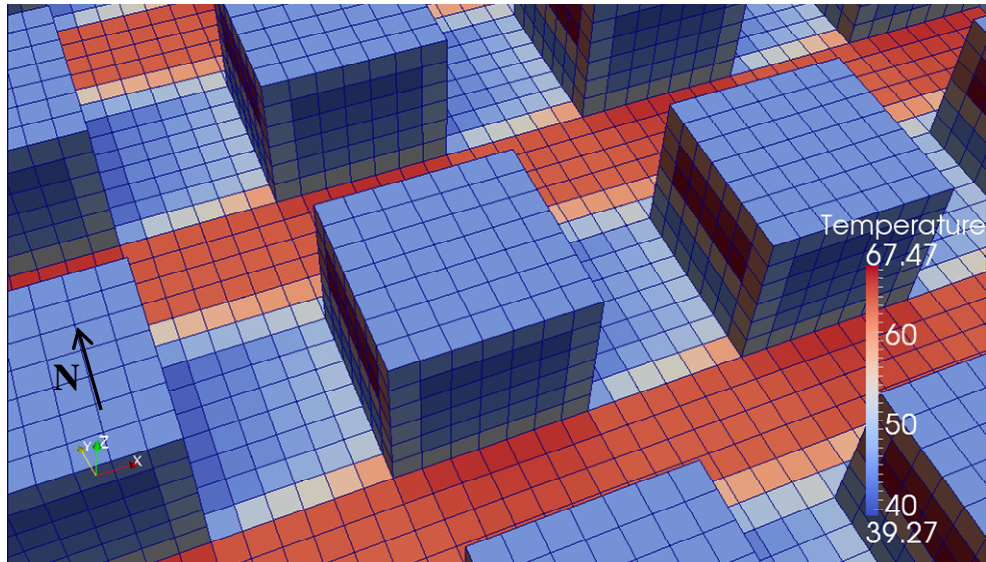
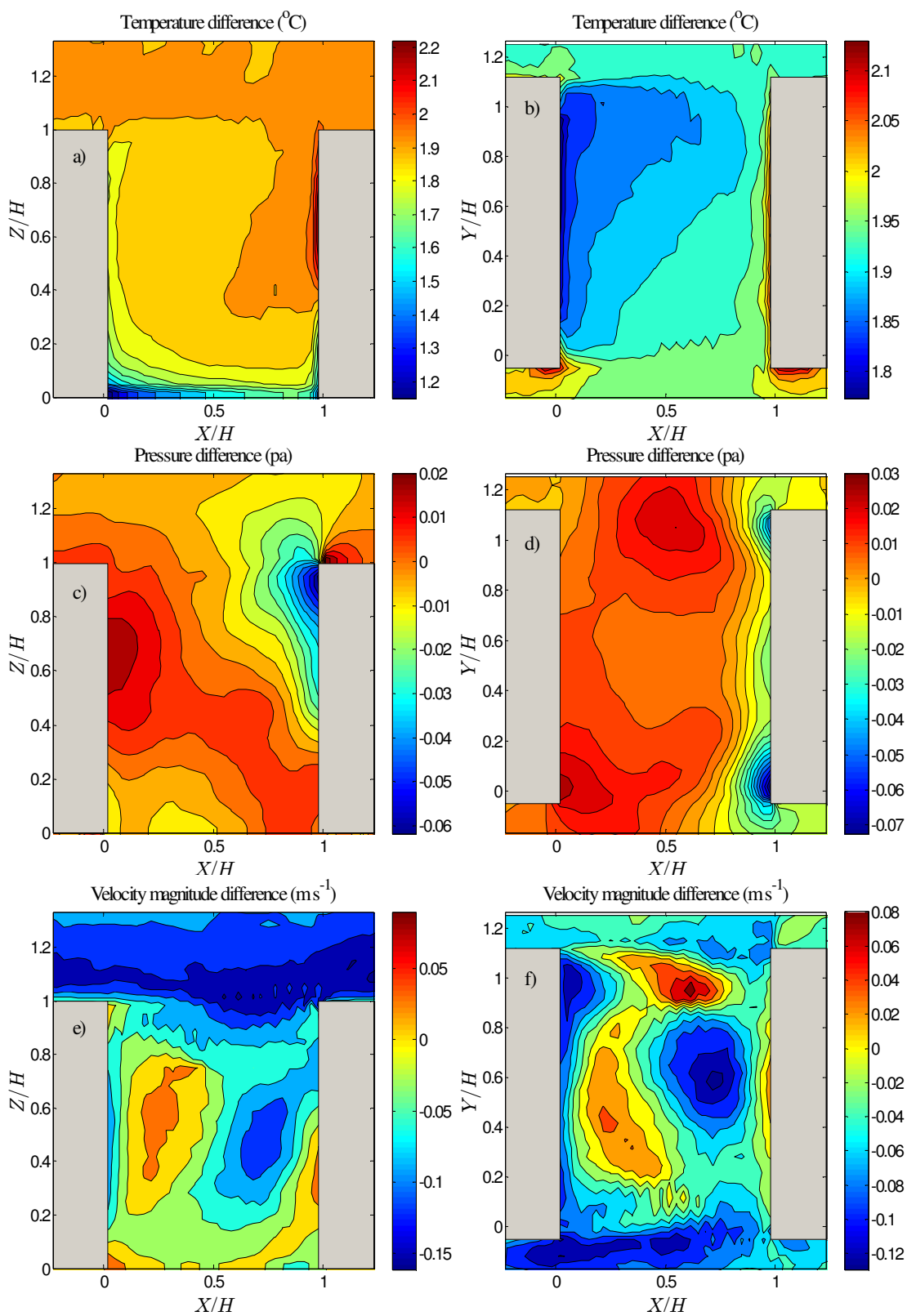


FIG. 4.10 Surface temperature in the TUF-IOBES simulation domain at 1715 LST of the base case simulation. The center 4×5 patches of each facet are windows. The direction of the flow in the PALM simulations is from west to east.

FIG. 4.11 Ensemble and half-hour time-averaged temperature (a, b), pressure (c, d) and velocity magnitude (e, f) difference of the base case simulation from the time period between 1700 and 1730 LST and the uniform thermal forcing simulation (see the text). The left (right) side panel is from a vertical (horizontal) cross section at Y/H (Z/H) = 0.5 of the spanwise canyon.



Figs. 4.11a and 4.11b show the mean temperature field difference between the uniform and non-uniform thermal forcing simulations. As shown in Fig. 4.10, between 1700 and 1730 LST the upper part of the west facing (windward) wall is the warmest surface since it receives direct solar radiation at near normal incidence angles and the air temperature difference between the two non-uniform and uniform thermal forcing simulations is the largest there (2.2 °C). In general locally larger and smaller thermal forcing from the surfaces in the non-uniform simulation respectively generate lower and higher pressure compared to the uniform thermal forcing simulation. For example, the air temperature difference between the uniform and non-uniform thermal forcing simulations resulting from the cooler window at the center of the east facing wall and the warmer window in the middle of the west facing wall (Fig. 4.11b) explains the negative pressure difference adjacent to the upper part of the west facing wall in Figs. 4.11c. Figs. 4.11e and 4.11f show that the velocity magnitude in the downwind half of the canyon (closer to the west facing wall) is smaller in the non-uniform thermal forcing simulation presumably due to the updraft tendency of the flow near the warmer walls which counteracts the canyon vortex. Generally the velocity magnitude locally increases and decreases respectively adjacent to the warmer and cooler spots in the non-uniform thermal forcing simulation compared to the uniform one.

4.4.4 Effects of ground surface albedo and wind speed

To holistically examine effects of ground surface albedo and wind speed on flow characteristics and heat transport in street canyons detailed 3-dimensional

investigation would be required. For conciseness, we focus on the effects of these parameters on the diurnal variation of canyon-averaged TKE while locally examining the mean temperature and velocity fields.

a. Diurnal variation of canyon-averaged TKE (non-local effects)

Generally effects of ground surface albedo and wind speed change as a function of time of a day. Fig. 4.12 shows the daytime (from 1000 to 1900 LST) variation of ensemble and canyon-averaged TKE in the spanwise and streamwise canyons for all simulations.

As expected the average TKE is larger on June 9th when the average bulk wind speed and as a result the shear production is larger. With the wind speed of June 9th being twice that on August 17th, the canopy-averaged TKE of the neutral simulation of June 9th is about 4 times that on August 17th. With thermal forces added, the TKE inside the canyons increases and exhibits a diurnal cycle following the insolation on the ground surface in both canyons (Fig. 4.3). Consistent with that trend, Fig. 4.12 shows that the street-canyon flow contains more TKE when the canopy-bottom surface is paved with darker materials and the ground surface temperature is higher as a result [42]. From Fig. 4.12 it is also evident that the free-convection conditions (“NoWind”) generate more TKE than the pure mechanical forcing (“NoHeat”) on the weak wind day, but less than on the strong wind day. Interestingly the sum is larger than its parts as the simulation with convection and mechanical forcing shows more TKE than the sum of the neutral and free convection simulations.

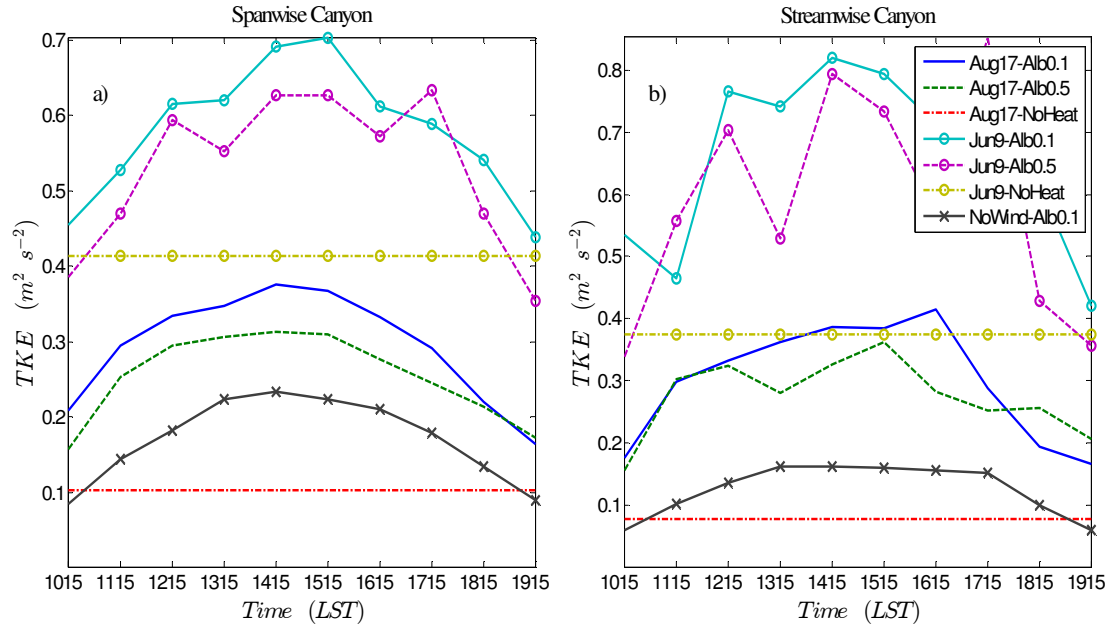


FIG. 4.12 Ensemble, time and canopy-averaged TKE for a) spanwise b) streamwise canyons. Each marker represents a time-averaged value over 1800s. The ‘No wind_alb 0.1’ case was run based on the August 17th thermal forcing.

b. Mean temperature and velocity fields (Local effects)

To show the local effects of ground surface albedo and wind speed, the temperature and velocity magnitude difference between the base case and high albedo simulations and between the base case and no wind are shown in Figs. 4.13 and 4.14, respectively. Velocity and temperatures are ensemble and time averaged between 1300 and 1330 LST (which is the time period that the ground surface in the spanwise canyon receives the most direct solar radiation) and from a vertical cross section at $Y/H = 0.5$ of the spanwise canyon.

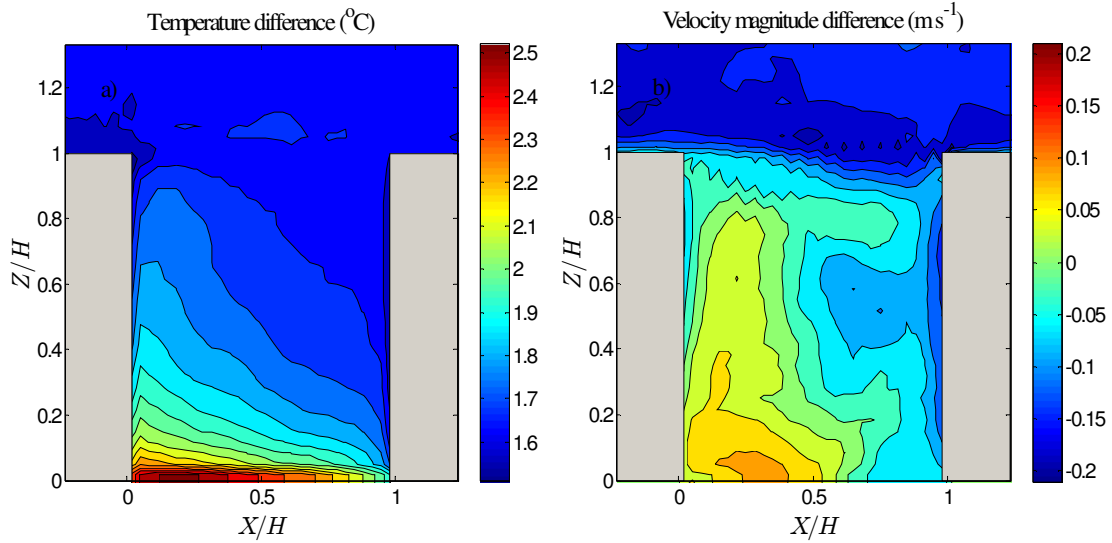


FIG. 4.13 Ensemble and time-averaged a) temperature and b) velocity magnitude difference of the base case simulation minus the August 17th simulation with ground albedo of 0.5 averaged over 1300 to 1330 LST at the center of the spanwise canyon.

Fig. 4.13a shows that the air temperature inside the canyon of the low albedo base case is up to 2.5 $^{\circ}\text{C}$ higher than the high albedo case. Due to reduced shortwave reflection from the ground, with darker ground materials the surrounding building walls are cooler than with brighter ground materials [42] and a smaller air temperature increase is evident there. The velocity magnitude for the low albedo case is larger in the upwind part of the canyon since the thermal forcing is aligned with the direction of the canyon vortex there. The velocity is smaller above the canyon due to the larger TKE and presumably stronger ejections and related shear driven by the stronger upward motion of the upwind half of the canyon vortex.

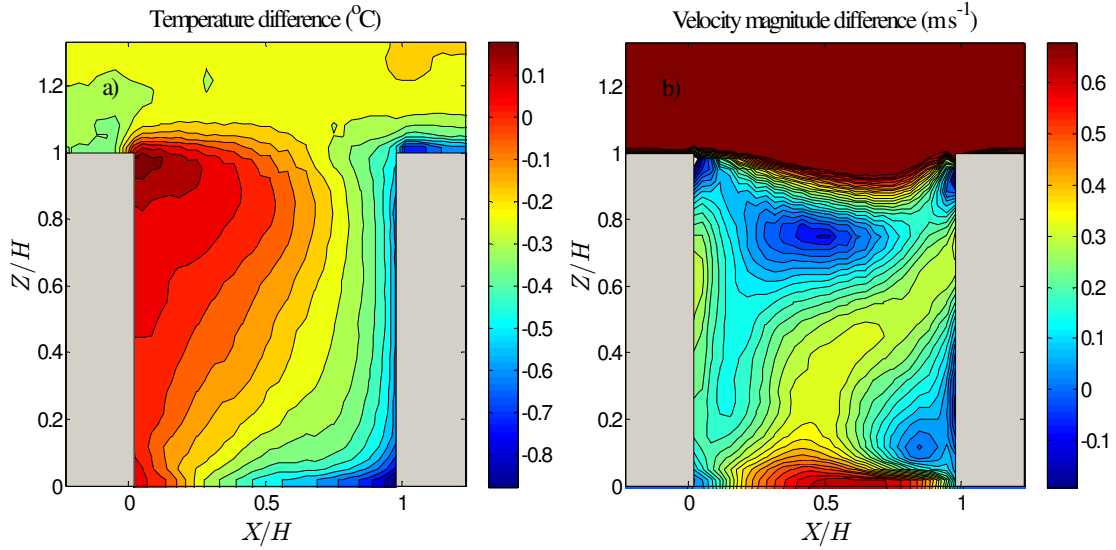


FIG. 4.14 Ensemble and time-averaged a) temperature and b) velocity magnitude difference of the base case simulation minus the corresponding no wind simulation averaged over 1300 to 1330 LST at the center of the spanwise canyon.

As expected, compared to the free-convection simulation the air is mixed more efficiently in the base case and therefore the air temperature inside the canopy is lower than in the free-convection case, except for within a short distance downwind of the roof (Fig. 4.14a). Not surprisingly Fig. 4.14b shows that the velocity magnitude is larger in the mixed convection simulation of the base case than the free-convection simulation and the difference is largest above the roughness layer. Comparison of the velocity vector field (not shown) shows that the negative velocity magnitude difference at $Z/H = 0.8$ indicates the vortex center in the base case simulation (where the velocity magnitude is small) whereas no vortical structure exists in the free-convection simulation.

4.5 Conclusions

In the daytime, urban canyon surfaces are heated by solar radiation. The amount of solar radiation received by the urban canyon surfaces is spatially and temporally variable throughout the canyon. The temperature of the surface depends on whether that surface receives direct solar radiation and on the thermal and radiative properties of its materials. Despite the fact that the thermal forcing from urban surfaces is uneven, most of the previous numerical studies represented urban areas through uniformly heated surfaces. In this study surface heat fluxes simulated in the Temperature of Urban Facets Indoor–Outdoor Building Energy Simulator (TUF-IOBES) were applied as thermal boundary conditions in the parallelized large-eddy simulation model (PALM) to investigate the effects of urban materials with different thermal and radiative properties (e.g. windows versus walls and reflective versus dark road pavements) and the moving shadows in the course of a day on the flow characteristics in three-dimensional urban canopies. TUF-IOBES provides detailed information of simulated surface temperature and heat fluxes on a raster-type geometry and as a result detailed thermal boundary conditions for CFD simulations.

By choosing a large enough domain size, unlike several previous 2D and 3D numerical studies (e.g. [17, 22, 23, 24, 34]), the effect of turbulent organized structures above the roughness layer is more accurately represented in this study.

The modified flow field of the non-uniform thermal forcing simulation compared to the uniform simulation demonstrates very complex and temporally variable flow patterns induced by moving shadows and variable surface thermal

properties. Generally strong horizontal pressure gradients were detected (in the base case simulation) in both streamwise and spanwise canyons throughout the daytime which motivate larger fluctuations of the turbulent flow in the horizontal directions rather than in the vertical direction. Consequently passive scalars (e.g. pollution or water vapor) would disperse more horizontally in between the canyons rather than being efficiently ventilated out of the canopies into the upper atmosphere. These pressure gradients are the results of air temperature difference in the spanwise and streamwise canyons as well as the effects of uneven input heat flux across each surface. This study shows the importance of three-dimensional simulations with detailed thermal boundary condition to explore the heat and mass transport in an urban area. The dynamics of the flow are very sensitive to changes in thermal forcing. As a result, besides simulations of the flow in urban areas with detailed geometry, detailed thermal forcing of the surfaces must also be explored. Realistic boundary conditions are especially important in pollution dispersion simulations and studying human safety and comfort in metropolitan areas.

As an extension of this work, it would be interesting to study the effects of urban configurations with different street canyon aspect ratios. In addition, it would be desirable to study diurnal variation of pollutant dispersion in urban areas in the presence of detailed surface thermal boundary conditions. A two-way coupling between TUF-IOBES and PALM through simulating surface sensible heat fluxes in PALM and using them in simulating surface temperatures in TUF-IOBES would provide more accurate flow and surface results for future studies. However, the added

computational expenses and the accuracy of the wall function model for simulating surface sensible heat fluxes in the CFD model must be justified first.

As stated by Solazzo and Britter [35], Offerle et al. [28] and Dimitrova et al. [20] buoyancy effects from the heated walls were not seen to have as large an impact on the measured flow field as has been shown in many CFD studies. Based on Solazzo and Britter [35] and Dimitrova et al. [20] this could be due to the inaccurate implementation of the thermal wall function (due to validating against thick thermal boundary layers) or to an insufficient grid resolution near the walls in the numerical models. Results of this study add to this conclusion that this also might be related to not considering the whole nature of the heated urban canyon surfaces (e.g. three-dimensionality and details of the thermal forces from urban surfaces).

Acknowledgments

Chapter 4, in part is currently being prepared for submission for publication of the material. Yaghoobian, Neda; Kleissl, Jan; Paw U, Kyaw Tha. The dissertation author was the primary investigator and author of this material.

References

- [1] Berg, R., Quinn, W. (1978) Use of light colored surface to reduce seasonal thaw penetration beneath embankments on permafrost. In: Proceedings of the Second International Symposium on Cold Regions Engineering, University of Alaska, 1978, 86–99.
- [2] Taha, H., Sailor, D.J., Akbari, H. (1992) High-albedo materials for reducing building cooling energy use. Lawrence Berkeley Laboratory, Berkeley, CA.
- [3] Rosenfeld, A.H., Akbari, H., Bretz, S., Fishman, B.L., Kurn, D.M., Sailor, D.J., Taha, H. (1995) Mitigation of urban heat islands: materials, utility programs, updates. *Energy Buildings* 22, 255–265.
- [4] Sailor, D.J. (1995) Simulated urban climate response to modifications in surface albedo and vegetative cover. *J. Appl. Meteorol.* 34, 1694–1704.
- [5] Parker, D.S., Barkaszi, S.F. (1997) Roof solar reflectance and cooling energy use: field research results from Florida. *Energy Buildings* 25, 105–115.
- [6] Akbari, H., Bretz, S., Kurn, D.M., Hanford, J. (1997) Peak power and cooling energy savings of high-albedo roofs. *Energy Buildings* 25, 117–126.
- [7] Akbari, H., Pomerantz, M., Taha, H. (2001) Cool surfaces and shade trees to reduce energy use and improve air quality in urban areas. *Sol. Energy* 70, 295–310.
- [8] Bretz, S., Akbari, H., Rosenfeld, A. (1998) Practical issues for using solar-reflective materials to mitigate urban heat islands. *Atmos. Environ.* 32, 95–101.
- [9] Akbari, H., Rainer, L. (2000) Measured Energy Savings from the Application of Reflective Roofs in 3 AT&T Regeneration Buildings. Lawrence Berkeley National Laboratory, Paper LBNL-47075.
- [10] Doulos, L., Santamouris, M., Livada, I. (2004) Passive cooling of outdoor urban spaces, the role of materials. *Sol. Energy* 77, 231–249.
- [11] Shashua-Bar, L., Pearlmutter, D., Erell, E. (2009) The cooling efficiency of urban landscape strategies in a hot dry climate. *Landscape Urban Plan* 92, 179–186.
- [12] Scherba, A., Sailor, D.J., Rosenstiel, T.N., Wamser, C.C. (2011) Modeling impact of roof reflectivity, integrated photovoltaic panels and green roof systems on sensible heat flux into the urban environment. *Build. Environ.* 46, 2542–2551.

- [13] Bouyer, J., Inard, C., Musy, M. (2011) Microclimatic coupling as a solution to improve building energy simulation in an urban context. *Energy Buildings* 43, 1549–1559.
- [14] Sini JF, Anquetin S, Mestayer PG (1996) Pollutant dispersion and thermal effects in urban street canyons. *Atmos Environ* 30:2659–2677
- [15] Kim JJ, Baik JJ (1999) A numerical study of thermal effects on flow and pollutant dispersion in urban street canyons. *J Appl Meteorol* 38:1249–1261
- [16] Kim JJ, Baik JJ (2001) Urban street-canyon flows with bottom heating. *Atmos Environ* 35:3395–3404
- [17] Kim JJ, Baik JJ (2010) Effects of Street-Bottom and Building-Roof Heating on Flow in Three-Dimensional Street Canyons. *Advances in atmospheric sciences* 28 (3):513–527.
- [18] Xie, X., Huang, Z., Wang, J., & Xie, Z. (2005) The impact of solar radiation and street layout on pollutant dispersion in street canyon. *Building and Environment*, 40(2), 201-212.
- [19] Xie, X., Liu, C. H., & Leung, D. Y. (2007) Impact of building facades and ground heating on wind flow and pollutant transport in street canyons. *Atmospheric Environment*, 41(39), 9030-9049.
- [20] Dimitrova, R., Sini, J. F., Richards, K., Schatzmann, M., Weeks, M., García, E. P., & Borrego, C. (2009) Influence of thermal effects on the wind field within the urban environment. *Boundary-Layer Meteorology*, 131(2), 223-243.
- [21] Cheng WC, Liu CH, Leung DYC (2009) On the correlation of air and pollutant exchange for street canyons in combined wind-buoyancy-driven flow. *Atmos Environ* 43:3682–3690.
- [22] Park, S. B., Baik, J. J., Raasch, S., & Letzel, M. O. (2012) A large-eddy simulation study of thermal effects on turbulent flow and dispersion in and above a street canyon. *Journal of Applied Meteorology and Climatology*, 51(5), 829-841.
- [23] Li, X. X., Britter, R. E., Norford, L. K., Koh, T. Y., & Entekhabi, D. (2012) Flow and pollutant transport in urban street canyons of different aspect ratios with ground heating: large-eddy simulation. *Boundary-Layer Meteorology*, 142(2), 289-304.
- [24] Cai, X. M. (2012) Effects of wall heating on flow characteristics in a street canyon. *Boundary-Layer Meteorology*, 142(3), 443-467.
- [25] Nakamura Y, OkeTR (1988) Wind, temperature and stability conditions in an east-west oriented urban canyon. *Atmos Environ* 22:2691–2700

- [26] Louka P, Vachon G, Sini JF, Mestayer PG, Rosant JM (2002) Thermal effects on the flow in a street canyon—Nantes'99 experimental results and model simulations. *Water Air Soil Pollut Focus* 2:351–364
- [27] Eliasson I, Offerle B, Grimmond CSB, Lindqvist S (2006) Wind fields and turbulence statistics in an urban street canyon. *Atmos Environ* 40:1–16
- [28] Offerle B, Eliasson I, Grimmond CSB, Holmer B (2007) Surface heating in relation to air temperature, wind and turbulence in an urban street canyon. *Boundary-Layer Meteorology* 122:273–292
- [29] Idczak M, Mestayer P, Rosant JM, Sini JF, Violleau MV (2007) Micrometeorological measurements in a street canyon during the joint ATREUS-PICADA experiment. *Boundary-Layer Meteorology* 124:25–41.
- [30] Kitous, S., Bensalem, R., & Adolphe, L. (2012) Airflow patterns within a complex urban topography under hot and dry climate in the Algerian Sahara. *Building and Environment*, 56, 162-175.
- [31] Uehara K, Murakami S, Oikawa S, Wakanatsu S (2000) Wind tunnel experiments on how thermal stratification affects flow in and above urban street canyons. *Atmos Environ* 34:1553–1562
- [32] Kovar-Panskus A, Moulinneuf L, Savory E, Abdelqari A, Sini JF, Rosant JM, Robins A, Toy N (2002) A wind tunnel investigation of the influence of solar-induced wall-heating on the flow regime within a simulated urban street canyon. *Water Air Soil Pollut Focus* 2:555–571
- [33] Vardoulakis S, Fisher BEA, Pericleous K, Gonzalez-Flesca N (2003) Modelling air quality in street canyons: a review. *Atmos Environ* 37:155–182.
- [34] Kwak, K. H., Baik, J. J., Lee, S. H., & Ryu, Y. H. (2011) Computational fluid dynamics modelling of the diurnal variation of flow in a street canyon. *Boundary-Layer Meteorology*, 141(1), 77-92.
- [35] Solazzo, E., & Britter, R. E. (2007) Transfer processes in a simulated urban street canyon. *Boundary-Layer Meteorology*, 124(1), 43-60.
- [36] Raasch, S., and Schröter M. (2001) PALM—A large-eddy simulation model performing on massively parallel computers. *Meteor. Z.*, 10, 363–372.
- [37] Letzel, M. O., Krane M. and Raasch S. (2008) High resolution urban large-eddy simulation studies from street canyon to neighbourhood scale. *Atmos. Environ.*, 42, 8770–8784.

- [38] Deardorff, J. W. (1980) Stratocumulus-capped mixed layers derived from a three-dimensional model. *Boundary-Layer Meteorology*, 18, 495–527.
- [39] Yaghoobian, N., & Kleissl, J. (2012) An Indoor-Outdoor Building Energy Simulator to Study Urban Modification Effects on Building Energy Use–Model Description and Validation. *Energy and Buildings*, 407–417.
- [40] Yaghoobian, N., Kleissl, J., & Krayenhoff, E. S. (2010) Modeling the thermal effects of artificial turf on the urban environment. *Journal of Applied Meteorology and Climatology*, 49(3), 332–345.
- [41] Lawrence Berkeley Laboratory (LBL), DOE2.1E-053 source code, 1994.
- [42] Yaghoobian, N., & Kleissl, J. (2012) Effect of reflective pavements on building energy use. *Urban Climate*.
- [43] American Society of Heating, Refrigerating and Air-Conditioning Engineers Inc. ANSI/ASHRAE/IESNA Standard 90.1-2004, Energy Standard for Buildings Except Low-Rise Residential Buildings I-P Edition.
- [44] American Concrete Pavement Association, Albedo: a measure of pavement surface reflectance. <<http://www.pavement.com/Downloads/RT/RT3.05.pdf>> (accessed 15.12.2011).
- [45] Kanda, M., Moriwaki, R., & Kasamatsu, F. (2004). Large-eddy simulation of turbulent organized structures within and above explicitly resolved cube arrays. *Boundary-Layer Meteorology*, 112(2), 343–368.
- [46] Coceal, O., Dobre A., Thomas T. G., and Belcher S. E. (2007) Structure of turbulent flow over regular arrays of cubical roughness. *J. Fluid Mech.*, 589, 375–409.
- [47] Inagaki, A., and Kanda M. (2010) Organized structure of active turbulence over an array of cubes within the logarithmic layer of atmospheric flow. *Boundary-Layer Meteorology*, 135, 209–228.
- [48] Takimoto H, Sato A, BarlowJF, MoriwakiR, Inagaki A, Onomura S, KandaM (2011) Particle image velocimetry measurements of turbulent flow within outdoor and indoor urban scale models and flushing motions in urban canopy layers. *Boundary-Layer Meteorology* 140:295–314
- [49] Inagaki, A., Castillo, M. C. L., Yamashita, Y., Kanda, M., & Takimoto, H. (2012) Large-eddy simulation of coherent flow structures within a cubical canopy. *Boundary-Layer Meteorology*, 142(2), 207–222.

- [50] Perret, L., & Savory, E. (2013) Large-Scale Structures over a Single Street Canyon Immersed in an Urban-Type Boundary Layer. *Boundary-Layer Meteorology*, 1-21.
- [51] Shaw, R. H., & Schumann, U. (1992) Large-eddy simulation of turbulent flow above and within a forest. *Boundary-Layer Meteorology*, 61(1-2), 47-64.
- [52] Pedersen, C.O., Liesen, R.J., Strand, R.K., Fisher, D.E., Dong, L., Ellis, P.G. (2001) A toolkit for Building Load Calculations; Exterior Heat Balance (CD-ROM), American Society of Heating Refrigerating and Air Conditioning Engineers (ASHRAE). Building Systems Laboratory.
- [53] Richards K, SchatzmannM, Leidl B (2006) Wind tunnel experiments modelling the thermal effects within the vicinity of a single block building with leeward wall heating. *J Wind Eng Ind Aerodyn* 94(8):621–636.

Chapter 5

Summary and conclusions

One of the first three-dimensional fully-coupled indoor–outdoor building energy simulators has been developed in this research to study the holistic impacts of urban heat island mitigation measures. As described in Chapter 1, a large number of processes such as weather conditions, indoor heat sources (from people and equipments), building and urban material radiative and thermal properties, composition of building envelopes (e.g. windows, insulation), and HVAC equipment can be considered in this two-way coupled model. TUF-IOBES is also capable of simulating effects of the waste heat from air-conditioning systems on urban canopy air temperature. Annual simulations of building energy use on about two days of a single processor are possible with this model. TUF-IOBES was validated against analytical heat transfer results and against previously validated and well-known building energy models. It can improve our understanding of how urban geometry and material modifications, the interaction between buildings and their surroundings, and dynamic combination of all of these effects in three dimensions modify urban energy use.

Using TUF-IOBES capabilities, in Chapter 2, the complex interaction between urban morphology, materials, and (seasonal) climate were considered to study the effects of reflective pavements on urban microclimates and building energy use in an office building in Phoenix, Arizona. Sensitivity of the results to canopy aspect ratio, building age (as reflected in the insulation), window surface area, and windows with different radiative properties were investigated. The results show that the annual thermal loads decrease with increasing canopy height-to-width ratio and increase with increasing window-to-wall ratio. On the other hand, annual cooling increases with increasing ground surface albedo but annual heating shows no sensitivity to ground

surface albedo. Compared to triple-pane clear windows, double-pane reflective windows decrease the annual cooling load and increase the annual heating load. This study highlights that although reflective pavements have been proposed as a mitigation measure for urban heat island since they reduce urban air temperatures, the increased solar reflectivity which transports solar radiation into (through fenestrations) and onto adjacent buildings increases building energy use.

Chapter 3 substantiated the ground surface albedo feedback on building wall temperatures. Counterintuitively building walls near a dark material (artificial turf) remained at a relatively cool temperature similar to buildings adjacent to irrigated grass surfaces. Both studies highlight the fact that the interaction of urban materials (i.e. reflective pavements) with surrounding buildings must be considered in the energy analysis of urban areas. Only local simulations for specific neighborhoods and urban climates can elucidate the exact effect of urban mitigation measures; with often surprising outcomes.

Specifically, the increase in energy use for buildings near reflective pavements for typical scenarios indicates that reflective pavements should be applied with caution. Previous research (i.e. [1]) showed that application of cool pavement to roads (which were not surrounded by air-conditioned buildings) reduced global radiative forcing counteracting global warming and reduced air temperatures and energy use in urban areas downwind. However others (i.e. [2, 3]) found that streets with lighter-colored walls generated a slightly higher total pedestrian heat gain, which was attributed to increased pedestrian exposure to shortwave radiation reflected from the

walls. We recommend that policymakers carefully weigh the benefits and disadvantages of reflective pavements to ensure their optimal application.

Despite the complexity of solar irradiance fields and existence of materials with different radiative and thermal properties in urban canopies, TUF-IOBES is able to estimate the non-uniform temperature and heat flux fields on urban surfaces throughout a day on three-dimensional raster-type urban geometries. In Chapter 4 we took advantage of this capability to derive detailed diurnally varying thermal boundary conditions for Large-Eddy Simulation (LES) to study flow and heat transport in urban canopies. The sensitivity of the results to ground surface albedo and wind speed were also tested. This study demonstrates very complex and temporally variable flow patterns induced by moving shadows and variable surface thermal properties (i.e. windows compared to the walls) in urban canyons throughout a day. This study demonstrates the importance of three-dimensional simulations with realistic thermal boundary condition to accurately quantify heat and mass transport in urban areas. Realistic boundary conditions are especially important in pollution dispersion simulations and studying human comfort in metropolitan areas.

Followings are some suggestions as extensions of this research which would provide additional insight into the physics and effects of urban microclimate:

- Model improvements to allow
 - more flexible model geometry to accommodate any possible building and canyon shape

- more sophisticated models for simulating vegetated surfaces (other than the Bowen ratio method explained in Chapter 3) and the water balance in urban areas
- Two-way coupling between TUF-IOBES and PALM (Although the computational expenses and the accuracy of the wall-function model for simulating surface sensible heat fluxes in the CFD model must be justified first.)
- Studying diurnal variation of street canyon wind flow and associated heat transport with detailed thermal boundary conditions for different (especially small) street canyon aspect ratios
- Studying diurnal variation of pollutant dispersion in urban areas in the presence of detailed surface thermal boundary conditions

References

- [1] H. Akbari, Menon, S., Rosenfeld, A., Global cooling: increasing world-wide urban albedos to offset CO₂. *Clim. Change* 94 (2009) 275–286.
- [2] D. Pearlmutter, Berliner, P., Shaviv, E., Physical modeling of pedestrian energy exchange within the urban canopy, *Build. Environ.* 41 (2006) 783–795.
- [3] E. Erell, Effect of high-albedo materials on pedestrian thermal comfort in urban canyons International Conference on Urban Climate, Dublin, Ireland, 2012.